Università
degli Studi
di Padova

University of Padua, Department of Physics and Astronomy "G. Galilei"
Master Thesis in Physics

Quantum states of interacting bosons coupled to spin-1 qudits

Gioele Vicentini
ID 2124513

Supervisor
Prof. Marco Di Liberto
University of Padova

Co-supervisor
Dr. Lorenzo Maffi
University of Padova

Academic Year 2025/2026

Contents

Abstract

Quantum engineered systems offer remarkable opportunities to identify quantum phases, including topological states of matter. A prominent example is the Peierls instability, already known to occur in quantum materials via coupling to phonons. Recent investigations have shown that a similar mechanism can be identified in quantum simulators by coupling strongly-interacting bosons to qubits via a $\mathbb{Z}_2$ theory. Current developments in quantum simulation and computing have recently started focusing on architectures beyond the qubits paradigm. In this spirit, here we focus on the scenario in which bosons are coupled to spin-1 qudits, providing distinct couplings and possibilities as compared to the spin-$1/2$ qubit case. The analysis will involve the identification of novel coupling terms available via spin-1 qudits and of the corresponding quantum phases originating in such many-body system.

1 Introduction

The study of quantum many-body systems represents an open challenge in modern physics. While the fundamental laws governing microscopic particles are well established through quantum mechanics, the collective behavior emerging from interacting quantum systems often becomes analytically and computationally intractable. Indeed, the dimension of the Hilbert space describing a many-body quantum system grows exponentially with the number of particles, making exact numerical simulations computationally expensive even for small systems. This behavior motivates the development of alternative techniques capable of reproducing and investigating the physics of many-body quantum systems.

Quantum simulation [1, 2] is a promising application of quantum technologies able to capture the complexity of these many-body systems. Quantum simulation broadly divides into digital and analog approaches. Given a Hamiltonian of interest, digital quantum simulation relies on the representation of its quantum state as a collection of two-level systems, called qubits. The dynamics induced by the Hamiltonian is approximated by applying a collection of quantum gates, basic logical operators, to the qubit system. In contrast, analog quantum simulation exploits the natural evolution of a controllable quantum system engineered to reproduce the Hamiltonian of interest. Analog simulators have been implemented on many physical platforms such as atomic or solid state systems due to the large degree of control obtained experimentally in the last decades. These systems include ultracold atoms in optical lattices [3, 2], trapped ions [1], Rydberg atom arrays [4], and superconducting circuits [5]. Their ability to access regimes that are challenging for both classical and digital quantum methods has established them as a powerful tool for quantum science.

An interesting collection of complex many-body phases is represented by

systems featuring beyond-Landau transitions. Landau's theory of symmetry-breaking predicts that phases of matter separated by a transition are characterized by a suitable local order parameter. Beyond Landau's paradigm, the different phases are not characterized by a local order parameter, but instead feature an emergent global order of topological origin.

A paradigmatic example of such topological states is the Su-Schrieffer-Heeger (SSH) model [6]. Introduced in 1979, it was initially developed to study the electronic properties of polyacetylene chains and the emergence of a quantized bulk polarization P [7]. The model consists of a one-dimensional tight-binding fermionic chain with alternating hopping amplitudes at half-filling, which satisfies time-reversal and chiral symmetries. It was later discovered that the SSH model features two different possible ground states, one of which features a quantized nonvanishing bulk polarization, both characterized by distinct nonlocal invariants. This quantization and the topological nature of the two possible ground states are encoded in the presence of different quantized Berry phases [8] for the two gapped ground states. At half-filling, the many-body fermionic ground state depends on all the single particle states of the lower bulk band, thus making the Berry phase a global property of the system: the topological properties of the system are robust against local or continuous perturbations. Furthermore, the nonvanishing bulk polarization P is a mark of the presence of a gapped bulk phase protected by time-reversal and chiral symmetry, which also allow for the existence of massless excitations exponentially localized at the edges of a finite chain. These properties are hallmarks of the so called symmetry-protected topological insulators [7].

Although originally studied in solid-state systems, recent advances in the field of analog quantum simulation [9, 10, 1] motivated the realization of such topological phase in accessible and tunable settings with both Rydberg atoms [11] and ultracold atoms [12].

1.1 A $1D$ symmetry-protected topological insulator

As we will discuss in chapter 2, the Hamiltonian of the original SSH model leads to an effective theory consisting of a one-dimensional tight-binding chain with two atoms per unit cell and alternating hopping amplitudes. We label the two atoms of a unit cell as A, B and, for a chain of N unit cells, particles in the system are allowed to hop in between nearest-neighboring sites. If particles hop between sites A, B of the same unit cell the hopping amplitude is $v > 0$, while between different unit cells the hopping amplitude is $w > 0$. The Hamiltonian

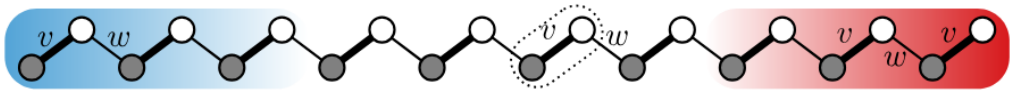

Figure 1.1: A representation of the SSH chain: intercell hopping amplitudes are marked with normal lines, while intracell hopping amplitudes with bold lines. The encircled section is a unit cell and the shaded background identifies the left and right edge regions. Image taken from [7].

for such system is:

$$\hat{H} = \sum_n \left(v\hat{a}_n^\dagger \hat{b}_n + w\hat{a}_{n+1}^\dagger \hat{b}_n + \text{h.c.} \right). \tag{1.1}$$

where the first term accounts for intracell hopping while the second accounts for intercell hopping and $h.c.$ identifies the hermitian conjugate. The single-particle operators $\hat{a}_n, \hat{b}_n$ destroy a particle on the respective site A, B of the n-th unit cell. Note that the lattice is bipartite between sites A, B as no particles on the m-th site A can hop to another site of type A: $\langle m, A| H |n, A\rangle = \langle m, B| H |n, B\rangle = 0 \, \forall m, n$. A representation of the SSH model can be found in Figure 1.1.

Despite its apparent simplicity, the SSH model has become paradigmatic in the study of topological matter due to its rich physical properties and analytical tractability.

A convenient way to analyze the SSH model is through its momentum-space representation. The Hamiltonian in Eq. (1.1) is invariant under translations of the two-sites unit cell. Bloch's theorem grants the existence of a momentum dependent Hamiltonian that can be expressed as a 2×2 matrix $\hat{H}(k) = \sum_{\alpha\beta \in A,B} \langle k, \alpha| \hat{H} |k, \beta\rangle \cdot |k, \beta\rangle \langle k, \alpha|$. Momentum space wavefunctions are defined as $|k, A\rangle = \sum_{m=1}^{N} e^{imk} |m, A\rangle / \sqrt{N}$, where we assume the lattice spacing to be $a = 1$. For the SSH model of Eq. (1.1), the Bloch Hamiltonian reads:

$$\hat{H}(k) = \begin{pmatrix} 0 & v + we^{-ik} \\ v + we^{ik} & 0 \end{pmatrix}. \tag{1.2}$$

The energy bands of bulk eigenstates $|u(k)\rangle$ of $\hat{H}(k)$ are:

$$E(k) = \pm\sqrt{v^2 + w^2 + 2vw\cos(k)}. \tag{1.3}$$

As shown in Figure 1.2, we see that the two possible energy bands are separated by a minimal energy gap $\Delta E = |v - w|$ at $k = \pm\pi$. If $v = w$, at $k = \pm\pi$ the band gap closes.

The Bloch Hamiltonian can be written as $\hat{H}(k) = \mathbf{d}(k) \cdot \boldsymbol{\sigma}$, with $\mathbf{d}(k) \in \mathbb{R}^3$ and

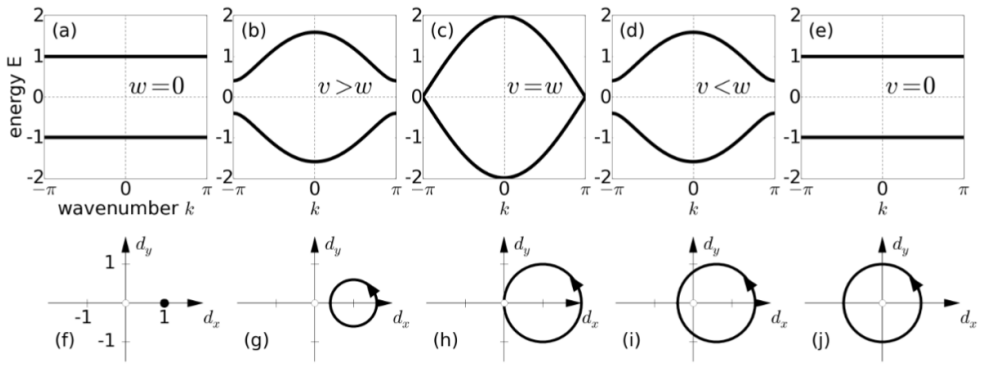

Figure 1.2: Top panels: dispersion relations of the SSH model. Bottom panels: $\mathbf{d}(k)$ vector path as k sweeps across the first Brillouin zone. From left to right we report five combinations of the hopping amplitudes v, w: $(a): v = 1, w = 0$, $(b): v = 1, w = 0.6$, $(c): v = 1, w = 1$, $(d): v = 0.6, w = 1$, $(e): v = 0, w = 1$. Image taken from [7].

$\boldsymbol{\sigma} = (\sigma_x, \sigma_y, \sigma_z)$ are the Pauli matrices. From Eq. (1.2), we find:

$$\mathbf{d}(k) = (v + w\cos(k), w\sin(k), 0)^T . \tag{1.4}$$

As k sweeps the first Brillouin zone, namely the interval $[-\pi, \pi]$, $\mathbf{d}(k)$ maps a circle in the xy plane centered in $(v, 0)$ of radius w.

Chiral symmetry is defined by the presence of an operator anticommuting with the bulk Hamiltonian. Since the SSH model is characterized by $d_z(k) = 0$, the bulk Hamiltonian satisfies $\left\{\hat{H}(k), \hat{\sigma}_z\right\} = 0$ and the Hamiltonian of Eq. (1.1) indeed features chiral symmetry represented by the operator $\hat{\sigma}_z$.

The presence of chiral symmetry has a relevant consequence on the properties of the ground state of Eq. (1.1): since $\mathbf{d}(k)$ is restricted to the xy plane, its path as k changes defines a closed circle that either contains or not the origin $\mathbf{d}(k) = 0$. This special point corresponds to a closed gap $v = w$, since $d_z(k) = 0$ is granted by chiral symmetry and for $v = w$, $k = \pm\pi$ the vector in equation (1.4) is zero.

Furthermore, as long as the system is gapped the path swept by the vector $\mathbf{d}(k)$ cannot pass through the origin. Then, a closed path containing the origin cannot be continuously deformed into one which does not, without closing the gap. In terms of adiabatic transformations, this means that the two ground states for $v > w$ and $v < w$ are topologically disconnected: as long as chiral symmetry is present, we cannot connect one ground state into the other by chiral-preserving smooth deformations of the Hamiltonian without closing the gap $v = w$.

To distinguish the two topological phases, we introduce the winding number ν which counts how many times the vector $\mathbf{d}(k)$ circles around the singularity

$\mathbf{d}(k) = 0$: From Figure 1.2, it's clear that for $v > w$ the circle in the xy plane does not contain the degenerate point $v = w$, thus $\nu = 0$. If instead $w > v$, the origin is encircled once and the bulk winding number is $\nu = 1$. This integer quantity remains invariant under continuous deformations that preserve the energy gap and chiral symmetry. We define the phase with $\nu = 0$ to be trivial, while the one with $\nu = 1$ is topological.

1.1.a Edge states and bulk-boundary correspondence

One of the manifestations of the nontrivial topology is the appearance of edge states in finite chains. Under open boundary conditions, exponentially localized zero-energy modes emerge at the ends of the chain, reported in Figure 1.3. Their appearance is protected by chiral symmetry and is robust against a broad class of perturbations.

To show how localized, zero-energy edge modes emerge in the topological ground state of the SSH model, we return to the real space definition of Eq. (1.1). We focus on an open chain consisting of N two-site unit cells, which starts with a site of type A and ends with a site of type B. The hopping amplitudes at both edges have strengths v.

We look for a single particle wavefunction in the real space basis composed of $|m, A\rangle, |n, B\rangle$ states. Our ansatz reads:

$$|E\rangle = \sum_{m=1}^{N} (a_m |m, A\rangle + b_m |m, B\rangle) \tag{1.5}$$

where, for a finite chain of N two-site unit cells, $m \in 1, \ldots, N$.

Edge states must be zero-energy eigenstates:

$$\hat{H} |E\rangle = 0 \tag{1.6}$$

Furthermore, the Hamiltonian of Eq. (1.1) is bipartite: particles are allowed to hop only from sites A towards sites B and vice versa, as only nearest-neighbor hoppings are present. Due to the bipartite nature of the SSH model, by projecting Eq. (1.6) onto sites $|n, A\rangle, |m, B\rangle$ we find:

$$\begin{aligned} \langle n, B| \hat{H} |E\rangle &= v a_n + w a_{n+1} \\ \langle n, A| \hat{H} |E\rangle &= w b_{n-1} + v b_n. \end{aligned} \tag{1.7}$$

Since $\hat{H}\left|E\right\rangle = 0$ we find a set of $2N$ constraints:

$$\begin{aligned} a_{n+1} &= -\frac{v}{w}a_n \\ b_{n+1} &= -\frac{w}{v}b_n \end{aligned} \tag{1.8}$$

for sites different from the edges a_1 and b_N. Our open chain starts and ends with an intercell hopping strength v, thus the particles localized on sites $\left|1,A\right\rangle, \left|N,B\right\rangle$ are allowed to hop only towards the bulk. Consequently, the single particle wavefunction must satisfy:

$$\begin{aligned} va_N &= 0 \\ vb_1 &= 0 \end{aligned} \tag{1.9}$$

For a semi-finite chain $N \to +\infty$ we find the solution $a_m = \left(\frac{-v}{w}\right)^{m-1} a_1$ and $b_m = 0$, which is indeed localized at the $m = 1$ edge of the chain. For a finite length chain ($N < +\infty$), no zero energy solution is actually allowed. Indeed, it should satisfy $a_m = \left(\frac{-v}{w}\right)^{m-1} a_1$ and $b_m = 0$, but the constraints on the borders require $a_N, b_1 = 0$. For a finite length chain the edge states have always a small hybridization and therefore a finite energy.

Focusing on $a_N \neq 0$, by taking first the logarithm on both sides and then the large N limit we find:

$$\log\left|\frac{a_N}{a_1}\right| = (N-1)\log\left|\frac{v}{w}\right| \equiv -\frac{N-1}{\epsilon} \tag{1.10}$$

where we introduced the penetration length $\epsilon^{-1} = \log|w| - \log|v|$. For large N a good approximation of zero-energy states are states exponentially localized on the edges of the lattice:

$$\begin{aligned} |a_N| &= \exp\left(-\frac{N-1}{\epsilon}\right)|a_1| \\ |b_1| &= \exp\left(-\frac{N-1}{\epsilon}\right)|b_N| \end{aligned} \tag{1.11}$$

where the values of a_1 and b_N are fixed by the normalization of the wavefunction.

We see from Eq. (1.11) that in order to have a nontrivial result for a_N, the penetration length must be positive. Indeed, in order for the logarithm of Eq. (1.10) to make sense we need $v < w$. This implies that the SSH model has two regimes: a trivial one with $v > w$ in which there are no edge states, followed by a topological one with $w > v$ which features exponentially-localized states at

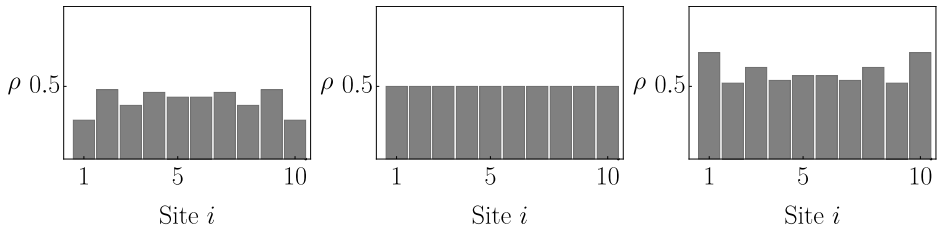

Figure 1.3: Fermionic density on the ground state for the SSH model on an open chain of 5 unit cells, at half-filling and with $v/w = 0.75$. The number of fermions along the chains are 4 (left), 5 (middle) and 6 (right) corresponding to a -1 filling anomaly, half-filling and $+1$ filling anomaly respectively. Localized zero-energy edge modes appear in the noninteracting fermionic ground state as we remove or add a particle.

the edges.

The constraints of Eq. (1.6) and the large N limit which leads to Eq. (1.10) actually lead to two orthogonal approximate edge states, one living on each end of the lattice and each restricted to one of the two sublattices A, B:

$$|L\rangle = \sum_{m=1}^{N} \left(-\frac{v}{w}\right)^{m-1} a_1 |m, A\rangle \tag{1.12}$$

$$|R\rangle = \sum_{m=1}^{N} \left(-\frac{v}{w}\right)^{N-m+1} b_N |m, B\rangle \tag{1.13}$$

Since these states hybridize for a finite-length chain, the real eigenstates are symmetric and antisymmetric combinations of $|L\rangle, |R\rangle$:

$$|0_\pm\rangle = \frac{|L\rangle \pm |R\rangle}{\sqrt{2}} \tag{1.14}$$

of small opposite energies $E_\pm = \pm \left|a_1 b_N v e^{-(N-1)/\epsilon}\right|$. As the size of the chain grows, the overlap between the states of Eq. (1.12) vanishes exponentially:

$$|\langle R| H |L\rangle| = \left|b_N a_1 v e^{-(N-1)/\epsilon}\right|. \tag{1.15}$$

We see that the hybridization depends on the penetration length ϵ but falls exponentially with the size of the chain N. Figure 1.3 shows the fermionic density near half-filling. Adding or removing an electron from the system corresponds to adding/removing a charge $e/2$ from each edge, which is an example of charge fractionalization.

1.2 Motivation and Structure of the Thesis

The SSH model has become an essential theoretical and experimental platform for studying topological physics. Its simplicity allows for analytical treatment, while its experimental realizations span numerous physical systems, including ultracold atoms [13, 14].

The interplay between quantum simulation and topological matter has gained relevant interest in modern physics. Topological phases of noninteracting systems are completely characterized by the topological properties of their Bloch Hamiltonian $\hat{H}(k)$ as the one of Eq. (1.2) [15]. The single particle description, which is needed for the validity of the Bloch Hamiltonian formalism, fails once we introduce interactions among degrees of freedom. The field of SPT interacting phases has developed quickly in recent years, leading to the complete characterization of interacting topological phases in one-dimension for fermions [16] and in any dimension for bosons [17, 18].

Starting from these theoretical and experimental premises, González-Cuadra et al. propose a one-dimensional model based on a lattice of bosonic particles interacting with spin-$1/2$ degrees of freedom sitting on the bonds of the chain. This system features the emergence of an interacting, one dimensional topological insulator and, at the same time, the spontaneous breaking of translational invariance in its ground state. Furthermore, the breaking of translational invariance on the ground state is induced by a mechanism similar to the Peierls transition [19], a phenomenon of paramount importance in one-dimensional fermionic systems. For the emergence of the topological phase this model needs a nonvanishing coupling between bosons and spin-$1/2$ degrees of freedom, thus defining a topological interacting phase. Furthermore, they show that this symmetry-broken phase is robust against local perturbations of the spin-$1/2$ sites living on the bonds.

Building upon this framework and motivated by recent interest in experimental realizations of SPT phases, this thesis explores a spin-1 extension of the model introduced by González-Cuadra [20] and is organized as follows.

In chapter 2, we introduce the physics of the original SSH model as introduced in 1979 and highlight its ability to undergo a Peierls transition in the mean-field regime. Then we report on the model proposed by González-Cuadra et al. and show how to map the fermions and phonons of the original SSH Hamiltonian to strongly interacting bosons and spin-$1/2$ degrees of freedom. Furthermore, we develop the analytical tools and numerical results needed to characterize the phases of the ground state. We then focus on the symmetry-broken ground state that features interesting topological traits, as the emergence of an effective SSH

bulk Hamiltonian like Eq. (1.2) and the presence of localized edge states.

The content of chapter 3 focuses on spin-1 pure states, showing how they encode more information than spin-$1/2$ and how their description naturally leads to the definition of the quadrupolar tensor of fluctuations $\hat{Q}_{\alpha\beta}$. After analyzing time-reversal invariant states, a feature of half-even spin states, we present a complete characterization of spin-1 pure states as pairs of orthogonal three-dimensional vectors $\mathbf{u}, \mathbf{v}$.

In chapter 4 we introduce an extension of the original model proposed by González-Cuadra et al. which features spin-1 degrees of freedom and quadrupolar, time-reversal invariant states. The extended model, grounded on the results and mechanisms of [20], is able to show the same symmetry-broken ground state patterns of its spin-$1/2$ counterpart, but with relevant differences. Not only its ground state displays a uniform, translationally-invariant region where spin-1 states feature ferroquadrupolar order, but its parameter space contains regions of intertwined ferroquadrupolar-dipolar order. As an example, the mean-field ansatz predicts that the latter regions are characterized by spin-1 quadrupolar $|0\rangle$ states on even sites of the lattice, alternating with $|\pm 1\rangle$ states on odd sites, where $|0\rangle, |\pm 1\rangle$ are eigenstates of $\hat{S}_z$. Finally, we report numerical results obtained through exact diagonalization methods showing that the mean-field picture is not enough to characterize the ground state in the symmetry-broken configurations, although it remains an effective description.

In chapter 5 we draw the conclusions and outline the possible directions and open questions for future studies.

2 Topology from instability in spin-1/2 chains

In this chapter, we introduce the concept of Peierls instability in one dimensional systems, a well-known phenomenon in the study of fermionic chains [21, 22, 19]. We then give a brief introduction to the notion of topological states [16] and their connection to the aforementioned instability. Building from these concepts, we present an alternative many-body bosonic formulation of the Peierls mechanism motivated by the technology of modern quantum simulators [1]. The model we envision involves bosons in optical lattices. In particular, we review previous works from González-Cuadra et al. [23, 20], which study a chain of interacting bosons coupled to spin-$1/2$ degrees of freedom. For strong interactions this model exhibits the spontaneous breaking of translational symmetry in its ground state, which is found in a dimerized configuration. Under periodic boundary conditions (PBC) the ground state is exactly two-fold degenerate and its eigenspace is spanned by two dimerized states connected by translation of one site. These degenerate dimerized states are characterized by different non-vanishing topological invariants [8]. Under open boundary conditions (OBC) at finite size the two degenerate configurations split and one realizes a symmetry protected topological phase [24] characterized by the presence of zero-energy edge modes localized at the edges. These features resemble the ones found in the ground state of the fermionic Su-Schrieffer-Heeger model [6, 7], a paradigmatic model in the field of topological quantum matter. After presenting the model, we review the mean-field ansatz developed in [23] and then compare its behavior with the ground state obtained through exact diagonalization (ED).

2.1 The Su-Schrieffer-Heeger model

In the study of condensed matter systems in one dimension, the Peierls instability appears in chains of fermions interacting with lattice vibrations. Peierls' theorem [19] states that a chain of equally spaced atoms with one electron per site, i.e. at half filling, becomes unstable towards a dimerized configuration. Such a dimerization produces alternating strong and weak bonds for the electrons, which can be effectively described by a tight-binding Hamiltonian with staggered hopping amplitudes [25]. In much of modern literature, this effective description is referred to as the Su-Schrieffer-Heeger (SSH) model, originally introduced to describe the polarization of polyacetylene. In its original formulation [6] the SSH Hamiltonian explicitly includes the coupling between electrons and lattice vibrations in the following way:

$$\begin{aligned}\hat{H} = &-\sum_{i,\sigma}\left[t + g(\hat{q}_i - \hat{q}_{i+1})\right]\left(\hat{c}^\dagger_{i,\sigma}\hat{c}_{i+1,\sigma} + \hat{c}^\dagger_{i+1,\sigma}\hat{c}_{i,\sigma}\right) \\ &+\sum_i\left[\frac{\hat{p}_i{}^2}{2M} + \frac{\hat{K}}{2}\left(\hat{q}_i - \hat{q}_{i+1}\right)^2\right].\end{aligned} \tag{2.1}$$

The above tight-binding Hamiltonian describes fermions $\hat{c}_{i,\sigma}$ with spins $\sigma = \{\uparrow,\downarrow\}$ hopping on the lattice sites labeled by i, and interacting with lattice vibrations described as acoustic phonons. The fermions hopping strength depends on the relative lattice site displacements $\hat{q}_i - \hat{q}_{i+1}$, where $\hat{q}_i$ is the lattice coordinate of the i-th site. This model implements lattice vibration modes as collections of coupled harmonic oscillators on the bonds of the lattice.

2.1.a Optical phonons

Although the original SSH model of Eq. (2.1) provides a microscopic description of the coupling between electrons and atomic displacements, it involves acoustic phonons, i.e. collective vibrational lattice modes whose long-wavelength frequency vanishes as $\omega_{\mathrm{ph}}(k) \sim |k|$ for $k \to 0$. For quantum simulation purposes, in Ref. [26], Cuadra et al. discuss instead the variation presented in [27] of the Hamiltonian in Eq. (2.1) in which the dynamical degrees of freedom live independently on the bonds. More precisely, each link $l(i)$, between the i-th and $(i+1)$-th sites, hosts a local optical phonon mode of finite frequency ω, resulting in a collection of uncoupled harmonic oscillators. The fermionic hopping amplitude along each bond is then modulated by the corresponding local displacement of the local optical phonon. In this framework, the Hamiltonian

reads:

$$\hat{H} = -\sum_{i,\sigma} \left(t + g\hat{q}_{l(i)}\right) \left(\hat{c}^{\dagger}_{i,\sigma}\hat{c}_{i+1,\sigma} + \hat{c}^{\dagger}_{i+1,\sigma}\hat{c}_{i,\sigma}\right) + \sum_{i} \left[\frac{\hat{p}^2_{l(i)}}{2M} + \frac{K}{2}\hat{q}^2_{l(i)}\right] \tag{2.2}$$

While in the original model of Eq. (2.1) the electron-phonon coupling depends on the relative displacement of neighboring atoms, in the optical model of Eq. (2.2) the single canonical variable $\hat{q}_{l(i)}$ encodes the strength of the $l(i)$-th bond. The two models in Eq. (2.1) and Eq. (2.2) cannot be mapped into each other by the canonical transformation $\hat{q}_{l(i)} - \hat{q}_{l(i+1)} \to \hat{q}_{l(i)}$, which introduces additional terms $\hat{p}_{l(i)}\hat{p}_{l(i+1)}$ that are missing in (2.2). Despite this, recent numerical results show that the two models behave in the same way up to numerical errors at half filling [28]. While the acoustic-phonon description (2.1) is appropriate for solid-state systems such as polyacetylene, the optical-phonon formulation (2.2) is better suited for atomic quantum simulation platforms, where local bosonic modes can be naturally implemented.

We restrict our study to spinless fermions and express the phonon degrees of freedom in their Fock representation. The resulting model reads:

$$\hat{H} = -\sum_{i} \left[t + g\left(\hat{a}^{\dagger}_{l(i)} + \hat{a}_{l(i)}\right)\right] \left(\hat{c}^{\dagger}_{i}\hat{c}_{i+1} + \hat{c}^{\dagger}_{i+1}\hat{c}_{i}\right) + \sum_{i} \omega \hat{a}^{\dagger}_{l(i)}\hat{a}_{l(i)} \tag{2.3}$$

where $\omega = \sqrt{K/M}$ and phonons are described by bosonic creation and annihilation operators $\left[\hat{a}_l, \hat{a}^{\dagger}_{l'}\right] = \delta_{ll'}$.

2.1.b The Peierls transition

In this subsection, we analyze how the Peierls dimerization emerges in the optical-phonon formulation. In this setting, the lattice distortion is replaced by the expectation value of the local bond coordinate, which directly modulates the fermionic hopping amplitudes in Eq. (2.3). At half-filling, with L fermionic sites and $L/2$ spinless fermions, we focus on the adiabatic limit of slow phonons, obtained for large mass $M \to +\infty$ and hence vanishing energy $\omega \to 0$. In this regime, the phonon coordinates can be treated as quasi-classical variational parameters. For a fixed configuration of link displacements, $\langle \hat{q}_l \rangle = \langle \hat{a}^{\dagger}_l + \hat{a}_l \rangle$, the fermions experience an effective Hamiltonian with bond-dependent hopping amplitudes $t + g\langle \hat{q}_l \rangle$.

Then the energy of the effective fermionic Hamiltonian is minimized by the set of values of $\langle \hat{a}^{\dagger}_l + \hat{a}_l \rangle$ depending on the fermionic fillings. At half filling, the uniform chain has Fermi points at $k = \pm\pi/2$. A bond modulation with period

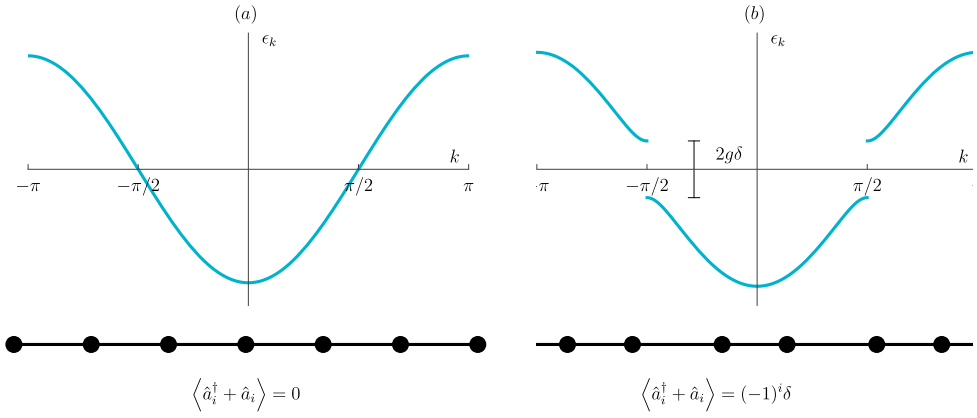

Figure 2.1: Uniform (a) and dimerized (b) configurations of the one-dimensional Su-Schrieffer-Heeger model. For the uniform configuration, the ground state is a single-band conducting metallic state. The dimerized configuration allows the opening of a band gap at the Fermi points $k = \pm\pi/2$ of size $2g\delta$. At half-filling, the Fermi energy ϵ_f has zero value and the opening of a gap in its region $k = \pm\pi/2$ lowers the fermionic energy.

two, $\langle \hat{a}_l^\dagger + \hat{a}_l \rangle = (-1)^l \delta$, carries momentum $Q = \pi = 2k_F$ and therefore mixes the degenerate low-energy modes at the two opposite Fermi points in Fig.2.1. The resulting fermionic spectrum becomes gapped at the Fermi energy, so that the occupied single-particle states are shifted downward in energy. Since the optical phonons sector is made of independent harmonic oscillators, it provides only an elastic quadratic energy cost $\Delta E_{\rm ph} \sim +\delta^2$.

In the mean-field regime $\omega \to 0$, the quasi-classical displacement which minimizes the total energy assumes alternating values $\langle \hat{a}_l^\dagger + \hat{a}_l \rangle = (-1)^l \delta$ with real δ.

The alternating fermionic hoppings $-t \pm g\delta$ mark the spontaneous symmetry breaking of translational invariance of the one-dimensional chain, as in Figure 2.1

Furthermore, the effective fermionic Hamiltonian reads:

$$\hat{H}_f = -\sum_i \Big[(t + g\delta) \hat{c}_{2i}^\dagger \hat{c}_{2i+1} + (t - g\delta) \hat{c}_{2i+1}^\dagger \hat{c}_{2i+2} + \text{H.C.} \Big] \tag{2.4}$$

which is exactly the two-level fermionic Hamiltonian introduced in section 1.1 with staggered hoppings $J = t + g\delta$ and $J' = t - g\delta$. In specific regimes, as discussed in the previous chapter the ground state of the model in Eq. (2.4) manifests topological features such as different finite topological invariants for periodic boundaries and localized zero energy edge states for open boundaries.

The effective Hamiltonian of Eq. (2.4) describes an insulator with nonzero band gap of size $2g\delta$. The transition from a uniform, conducting ground state for $\delta = 0$ to the insulating state is a characteristic of the Peierls transition, which makes the SSH model of Eq. (2.2) a Peierls insulator at half-filling and in the mean-field regime.

2.2 Synthetic Dynamical Lattice

The aim of this section is to design a Hamiltonian which mimics the physics of the SSH model in Eq. (2.3) and that can be implemented on a quantum simulation platform. Rather than simulating the microscopic electron-phonon system directly, we recast its relevant degrees of freedom in terms of experimentally accessible bosonic and spin variables. Modern quantum simulators can in principle be built from both fermionic and bosonic local degrees of freedom: consequently this makes it possible to implement directly the Hamiltonian of (2.3). However, the goal of the present construction is not only to reproduce the non-interacting SSH limit, but also to formulate a synthetic many-body model in which Peierls physics, topology and strong correlations can be explored in a controllable bosonic setting. For this reason, we chose to study a fully bosonic effective Hamiltonian to be coherent with previous works [23] and because of the established interest present in the literature in strongly interacting bosonic phases of matter [14, 10, 29, 1]. As will be clear in the following, this formulation connects to the spinless-fermion SSH model in the hardcore-boson limit, while also allowing to move away from this limit and explore genuinely bosonic regimes at finite onsite interactions.

We start with the paradigmatic one-dimensional Bose-Hubbard model [30]:

$$\hat{H} = -t \sum_i \hat{B}_i + \frac{U}{2} \sum_i \hat{n}_i \left(\hat{n}_i - 1\right) - \mu \sum_i \hat{n}_i \tag{2.5}$$

where $\hat{n}_i = \hat{b}_i^\dagger \hat{b}_i$ and $\left[\hat{b}_i, \hat{b}_j^\dagger\right] = \delta_{ij}$, while $\hat{B}_{l(i)}$ is the bosonic hopping operator between bosonic sites $i, i+1$:

$$\hat{B}_{l(i)} = \hat{b}_i^\dagger \hat{b}_{i+1} + \hat{b}_{i+1}^\dagger \hat{b}_i. \tag{2.6}$$

The hopping operator represents bosonic particles hopping from site i to site $i+1$ or, vice-versa, from $i+1$ to i. Consequently, while the number of bosonic particles on site i is not conserved by the operator $\hat{B}_{l(i)}$, the total number of bosons $\hat{n} = \hat{n}_i + \hat{n}_{i+1}$ commutes with $\hat{B}_{l(i)}$. From the bosonic canonical commutation

relations it's easy to show that $\left[\hat{n}_i, \hat{B}_{l(i)}\right] = -\left[\hat{n}_{i+1}, \hat{B}_{l(i)}\right]$.

The Bose-Hubbard Hamiltonian of Eq. (2.5) is a widely studied model in cold-atom experiments [31, 29]: it describes interacting bosonic particles hopping along a chain of localized sites, with hopping amplitude t. Particles are not able to freely move along the chain, as the interaction term $U > 0$ decreases the probability of finding two bosons on the same site.

Crucially, in the limit of large and positive self-interactions $U \to +\infty$, the on-site bosonic Hilbert space is dynamically restricted to the states $|0\rangle, |1\rangle$, yielding to the so-called hardcore bosons regime. For one-dimensional systems, hardcore bosons are mapped to spinless fermions under the Jordan-Wigner transformation [32] $\hat{b}_j^\dagger = \exp\left(i\pi \sum_{k=1}^{j-1} \hat{c}_k^\dagger \hat{c}_k\right) \hat{c}_k^\dagger$. Upon this transformation, we recover the fermionic operators of Eq. (2.2) satisfying the anticommutation relations $\{\hat{c}_i, \hat{c}_j^\dagger\} = \delta_{ij}$. Indeed, for open boundary conditions and nearest-neighbour hoppings, the string factors $\exp\left(i\pi \sum_{k=1}^{j-1} \hat{c}_k^\dagger \hat{c}_k\right)$ in the Jordan-Wigner transformation cancel in the Hamiltonian, so that the hardcore bosonic hopping model is equivalent to a free spinless-fermion Hamiltonian.

The second step towards a finite-dimensional quantum-simulation model concerns the phonons degrees of freedom of Eq. (2.2). Each local phonon mode corresponds to a harmonic oscillator with an infinite-dimensional Hilbert space. To obtain a finite dimensional description we truncate the phonon occupation number up to $n_{\text{ph}} < n_{\text{max}}$. This allows us to represent phonons as spin $S = n_{\text{max}}/2$ degrees of freedom through the Holstein-Primakoff transformation [33]:

$$\begin{aligned} S^+ &= \sqrt{2S - \hat{n}}\, \hat{a} \\ S^- &= \hat{a}^\dagger \sqrt{2S - \hat{n}} \\ S_z &= S - \hat{n} \end{aligned} \tag{2.7}$$

The Holstein-Primakoff representation is exact for a spin-S degree of freedom only within the physical bosonic subspace $0 \leq n_{\text{ph}} \leq 2S$. Therefore, using it to represent phonons requires the truncation of the local oscillator Hilbert space to the states with $n_{\text{ph}} \leq n_{\text{max}} = 2S$. This truncation must be checked carefully, because the optical SSH Hamiltonian does not conserve the number of phonons and the ground state generally contains a superposition of different phonon occupations. The spin representation is reliable only when the weight of states with n_{ph} close to or above n_{max} is negligible, for instance in regimes where phonons are energetically costly $\omega \gg t$.

On the contrary, Peierls physics appears in the limit of slow lattice deformations, $\omega \ll t$, where the phonons are better described as quasi-classical displacement fields rather than as few-particle quantum excitations. In the

oscillator-number basis, such classical distorted configurations would generally require large phonon occupation numbers n_{ph}, and therefore a truncation to the lowest phonon states is not a controlled approximation to the full optical SSH Hamiltonian (2.2) in the adiabatic regime. However, as we will see in the following sections, the truncated model should not be regarded as a quantitatively controlled low-energy truncation of the phononic Hilbert space. Rather, it provides a minimal finite-dimensional version of a dynamical lattice, where the continuous phonon displacement on each bond is replaced by a two-level $\mathbb{Z}_2$ degree of freedom and hence it can be represented on quantum simulators. This simplified model still retains the central Peierls mechanism: a slow bond field can spontaneously develop a staggered background, dimerize the matter hopping, and open a gap in the half-filled matter sector. The price to pay is that the resulting Peierls instability is no longer identical to that of the standard SSH model; in particular, the harmonic elastic energy of the phonons is replaced by the energy of the $\mathbb{Z}_2$ field, leading to a genuine parameter-dependent Peierls transition.

To transform the phonons on the links using Eq. (2.7) we truncate the onsite bosonic Hilbert space to 2 states, which corresponds to having a spin-$1/2$ degree of freedom on each link. An exact representation of $\hat{a}^\dagger, \hat{a}$ in this reduced space can be obtained by expanding $h(\hat{n}) = \sqrt{2S - \hat{n}}$ in its Newton series [34] up to order $\hat{n}^{2S} = \hat{n}$:

$$\begin{aligned} \sqrt{2S - \hat{n}}|_{S=1/2} &= 1 - \hat{n} \\ &= \frac{1}{2} + \hat{S}_z \end{aligned} \tag{2.8}$$

The second line comes from the substitution $\hat{S}_z = S - \hat{n} = 1/2 - \hat{n}$.

By plugging Eq. (2.8) back into Eq. (2.7) we obtain the exact representation of the spin-$1/2$ operators $\hat{S}^+, \hat{S}^-$ in the bosonic subspace spanned by the Fock states $|0\rangle, |1\rangle$. On this subspace we have $\hat{a}^2 = \left(\hat{a}^\dagger\right)^2 = 0$ and thus $\hat{S}^- = \hat{a}^\dagger$ and $\hat{S}^+ = \hat{a}$.

Transforming the bosonic operators of Eq. (2.3) into spin-$1/2$ operators we get:

$$\begin{aligned} \hat{a}^\dagger + \hat{a} &= \hat{S}^- + \hat{S}^+ \\ &= 2\hat{S}_x \\ &= \begin{pmatrix} 0 & 1 \\ 1 & 0 \end{pmatrix} \end{aligned} \tag{2.9}$$

which is the Pauli matrix $\hat{\sigma}_x$: the exact projection of the operator $\hat{a}^\dagger + \hat{a}$ on the

bosonic vector space composed of the states $|0\rangle, |1\rangle$. The result in Eq. (2.9) is valid only for spin-1/2 sites.

As a final step we rotate our spin operators such that $\hat{\sigma}_x \to \hat{\sigma}_z$ and $\hat{\sigma}_z \to -\hat{\sigma}_x$. The transformed Hamiltonian of Eq. (2.3) at half filling and after removing constant terms reads:

$$\hat{H} = -\sum_i \left[t + g\hat{\sigma}^z_{l(i)}\right]\left(\hat{b}^\dagger_i \hat{b}_{i+1} + \hat{b}^\dagger_{i+1}\hat{b}_i\right) + \frac{U}{2}\sum_i \hat{n}_i\left(\hat{n}_i - 1\right) + \sum_i \frac{\omega}{2}\hat{\sigma}^x_{l(i)} \quad (2.10)$$

The obtained Hamiltonian bears some similarities with the starting one of Eq. (2.3): bosonic particles hop along nearest-neighboring sites of a one-dimensional chain, with hopping strength which depends on the values of a $\mathbb{Z}^2$ field living on the bonds. The bosonic particles are also self-interacting with repulsive strength $U > 0$, which for $U \to +\infty$ leads to hardcore bosons. The dynamics of the $\mathbb{Z}^2$ fields is regulated by their energy ω.

2.3 Interacting bosons on a dynamical $\mathbb{Z}^2$ lattice

González-Cuadra et al. [26] propose an experimental setup using a mixture of ultracold atoms trapped in an optical lattice to recreate the Hamiltonian of Eq. (2.10). As shown in their work, this experimental platform not only grants the couplings needed to recreate the Bose-Hubbard and spin-1/2 operators, but also features other possible coupling. The final model, extended by the relevant experimentally available couplings, is the following:

$$\hat{H} = -\sum_i \left[\left(t + \alpha\hat{\sigma}^z_{l(i)}\right)\left(\hat{b}^\dagger_i \hat{b}_{i+1} + \hat{b}^\dagger_{i+1}\hat{b}_i\right) + \frac{U}{2}\hat{n}_i\left(\hat{n}_i - 1\right) + \beta\hat{\sigma}^x_{l(i)} + \frac{\Delta}{2}\hat{\sigma}^z_{l(i)}\right] \quad (2.11)$$

where we relabeled the energy of the phonons $\omega/2$ with the external parameter β, g with α and we added the onsite spin-1/2 dipolar operator $\Delta\hat{\sigma}^z_i/2$. This extended model, as shown in the following, recovers the symmetry-breaking phases of the Peierls transition.

The Hamiltonian of Eq. (2.11) describes a chain of alternating bosonic and spin sites. Bosonic particles hop in between these sites, with the hopping strength $t + \alpha\hat{\sigma}^z_i$ which depends on the value of the spin located on the relative link, as shown in Figure 2.2.

In this section, we first propose a mean-field treatment of the ground state of Eq. (2.11) for a frozen dynamic of the $\mathbb{Z}^2$ fields, then we report the results of a numerical study on the ground state via exact diagonalization methods. In the following part of this section we discuss on the presence of a topological

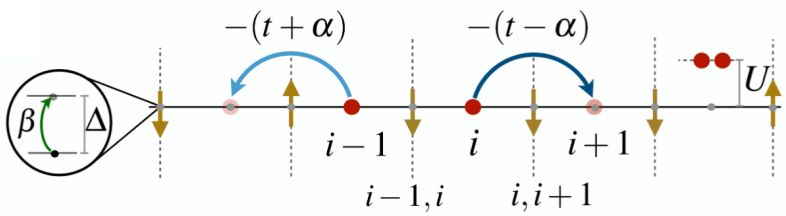

Figure 2.2: Representation of the bosons and spin-1/2 chain. Bosons hop in between neighboring sites (red dots) with hopping strength $-t \pm \alpha$ in the adiabatic regime $\beta = 0$, depending on the local spin degrees of freedom (arrows). In general, spins are influenced by both an orienting field of strength Δ and a disordering field proportional to β. Bosonic particles self-interact with strength U.

state hosting zero energy edge modes and its connection to the topological one-dimensional model introduced in section 1.1.

2.3.a Ground state mean field study

The Hamiltonian in Eq. (2.11) is nontrivial in its spin degrees of freedom as $\hat{\sigma}_x$ does not commute with $\hat{\sigma}_z$. In order to perform a mean-field analysis of the ground state, we neglect the $\hat{\sigma}_x$ contribution by setting $\beta = 0$. We also work with hardcore bosons to study the physics of the fermionic SSH model, $U \to +\infty$. Since the parameter β is connected to the phonons' energy and mass $\omega = \sqrt{K/M}$, as of Eq. (2.2), neglecting $\hat{\sigma}_x$ is equivalent to having phonons of large mass $M \gg K$. An in-depth study of the effects of β and U on the mean-field ansatz can be found in [20].

From Eq. (2.11), after removing constant terms and applying the Jordan-Wigner transformation the Hamiltonian becomes:

$$\hat{H} = -\sum_i \left[t + \alpha\hat{\sigma}^z_{l(i)}\right]\left(\hat{c}^\dagger_i\hat{c}_{i+1} + \hat{c}^\dagger_{i+1}\hat{c}_i\right) + \frac{\Delta}{2}\sum_i \hat{\sigma}^z_{l(i)} + \beta\sum_i \hat{\sigma}^x_{l(i)} \tag{2.12}$$

Setting $\beta = 0$ brought us to the adiabatic regime for the spin degrees of freedom: for all bonds $l(i)$ the local spin operator $\hat{\sigma}^z_{l(i)}$ commutes with the Hamiltonian $\left[\hat{H}, \hat{\sigma}^z_{l(i)}\right] = 0$. The ground state of the Hamiltonian is characterized by a fixed $\hat{\sigma}_z$ eigenstate $|\uparrow\rangle$ or $|\downarrow\rangle$ on each bond. This is the limit in which the spin dynamics is fully frozen with respect to the fermionic dynamics and thus fermions obey an exact effective Hamiltonian.

Furthermore, we study only the section of the parameter space spanned by α, Δ, β with semipositive $\alpha \geq 0$ with the fermionic hopping strength t fixed as our units of energy. Indeed, once we know the ground state for a given positive

α and arbitrary Δ, its counterpart for the parameters $-\alpha, -\Delta$ is obtained by flipping the direction of the spins of the initial ground state. This operation corresponds to a rotation of π in the Bloch sphere around the x axis. In the spin basis, this corresponds to applying the spin operator $\exp(-i\pi\hat{\sigma}_x/2)$. By flipping $\hat{\sigma}_z$, we invert its eigenstates $|\uparrow\rangle \to |\downarrow\rangle$ and $|\downarrow\rangle \to |\uparrow\rangle$. In conclusion, we can study the ground state in the region of the space of parameters (α, Δ, β) where $\alpha \geq 0$; by flipping the ground state spin configuration we get the ground state in the remaining region $(-\alpha, -\Delta, \beta)$ for fixed β.

Before introducing the analytical tools we need, we report on the behavior of the model for $\beta = 0$, and $\alpha, \Delta > 0$ in the limit cases $\Delta/\alpha \gg 1$ and $\Delta/\alpha \ll 1$:

- $\Delta/\alpha \gg 1$: spins and fermions interact weakly and the energy of the classical spin is dominated by the Zeeman local Δ-term. The model behaves like a tight-binding Hamiltonian with uniform nearest-neighbor hoppings on the fermionic side, like a ferromagnet on the spin side. The spins uniformly align to the spin-down state $|\downarrow\rangle$.
- $\Delta/\alpha \ll 1$: the fermionic band energy, which is proportional to the fermionic hopping amplitude strength, determines the spin behavior. Indeed, the spins align to the state $|\uparrow\rangle$ which leads to a strong uniform fermionic hopping amplitude $|t + \alpha| \gg \Delta$ and a lower fermionic energy contribution. This energy gain from fermionic side compensates the positive contribution $\sum_l \Delta\hat{\sigma}_l^z/2$ from the spin Hamiltonian, which is smaller.

As we will show, in the intermediate regime $\Delta \sim \alpha \sim t$ a Néel ordered region of the spins emerges along the chain: spins alternate in between $|\uparrow\rangle$ and $|\downarrow\rangle$ leading to staggered bosonic hoppings of $-t + \alpha$ and $-t - \alpha$. The quadrant of parameter space with $\Delta < 0$, $\alpha > 0$ features only ground states with uniform spin-up configurations $|\uparrow\rangle$, as both the energetic spin contribution and fermionic contributions reach their lowest levels $-|\Delta|/2$ and $-(t + \alpha)$ for each bond.

To understand where and why a Néel ordered region opens up in the range $\Delta \approx \alpha$, we follow the reasoning of [20] and introduce a variational ansatz for $\beta = 0$. Furthermore, we restrict our analysis to the hardcore bosons limit, $U \to +\infty$ so that our bosonic operators are exactly mapped to fermionic ones via the Jordan-Wigner transformation: $a_i^\dagger a_{i+1} \to c_i^\dagger c_{i+1}$.

As we stated above, for $\beta = 0$, the ground state is a product state of a fermionic wavefunction and a site-separable spin configuration. For small but finite β, the transverse field introduces slow quantum fluctuations of the spin background. In the adiabatic regime $\beta \ll t$, these fluctuations occur on a timescale much longer than the fermionic hopping time and the fermions can be assumed to respond almost instantaneously to a given spin configuration. This separation of time scales motivates us, at the variational level, to neglect spin-fermion

entanglement and approximate the total state as a product between a fermionic wavefunction and a generic site-separable spin state.

Spin correlations in between different sites are not present and thus a mean-field ansatz for the spin state is eligible. Furthermore, the spin Hamiltonian of Eq. (2.12) does not contain on-site terms proportional to $\sigma^y_{l(i)}$, so we choose real coefficients for the on-site spin wavefunction:

$$|\psi_s\rangle_{l(i)} = a_{l(i)} |\uparrow\rangle_{l(i)} + b_{l(i)} |\downarrow\rangle_{l(i)} \tag{2.13}$$

The ground state ansatz, with the aforementioned restrictions, has the following form:

$$|\mathrm{GS}(|\psi_f\rangle, \{a_{l(i)}, b_{l(i)}\})\rangle = |\psi_f\rangle \bigotimes_{i=0}^{N-1} \left[a_{l(i)} |\uparrow\rangle_{l(i)} + b_{l(i)} |\downarrow\rangle_{l(i)}\right] \tag{2.14}$$

where the fermionic wavefunction $|\psi_f\rangle$ lives in the fermionic Hilbert space.

Given the ansatz (2.14), we can write an effective fermionic Hamiltonian by substituting the spin operators $\hat{\sigma}^z$, $\hat{\sigma}^x$ in the Hamiltonian (2.12) with their variational expectation values on the ansatz $\langle\hat{\sigma}^z\rangle_{\mathrm{GS}}$ and $\langle\hat{\sigma}^x\rangle_{\mathrm{GS}}$. So for the spin living on the bounds, we have:

$$\left\langle \hat{\sigma}^z_{l(i)} \right\rangle_{\mathrm{GS}} = \left[a^2_{l(i)} - b^2_{l(i)}\right] \equiv s_{l(i)} \tag{2.15}$$

where $s_{l(i)}$ is a notational shorthand, and:

$$\left\langle \hat{\sigma}^x_{l(i)} \right\rangle_{\mathrm{GS}} = \left[a_{l(i)} b_{l(i)} + b_{l(i)} a_{l(i)}\right] = 2 a_{l(i)} b_{l(i)}. \tag{2.16}$$

By substituting back into the Hamiltonian of (2.12) for each configuration of link-spin variables $\{s_{l(i)}\}$, we get the fermionic effective Hamiltonian:

$$\hat{H}_f\left(\{s_{l(i)}\}\right) = -\sum_i (t + \alpha s_{l(i)}) \left(\hat{c}^\dagger_i \hat{c}_{i+1} + \hat{c}^\dagger_{i+1} \hat{c}_i\right) \tag{2.17}$$

In order to extract information from the ansatz, we simplify our problem: since we are looking for a dimerization, we restrict the variational parameters $\{s_{l(i)}\}$ to the strings composed of the repeating block of pairs (s_A, s_B). This last hypothesis excludes from our variational ansatz all the possible repeating patterns with periodicity higher than two, as well as configurations where a single spin is changed. To strengthen this assumption, numerical studies [20] show that the ground state at half filling is found in a uniform or dimerized configuration. We reobtained those numerical results and we report them at the

end of this chapter.

With this restriction, the unit cell contains two fermionic sites and two link-spin variables. We label the two fermionic sites in the jth unit cell with A and B, with corresponding operators $\hat{c}_{jA}$ and $\hat{c}_{jB}$, while the two link-spin variables are denoted by (s_A) and (s_B). Then we Fourier transform the fermionic operators $\hat{c}_{jA} = \frac{1}{\sqrt{L}} \sum_k e^{-ikj} \hat{c}_{kA}$, with $k \in [-\pi, \pi]$. L is the number of unit cells in our repeating periodic system and, at half filling, is also the number of hardcore bosons. To be consistent, we must also take $\hat{c}_{jB} = \frac{1}{\sqrt{L}} \sum_k e^{-ik(j+1/2)} \hat{c}_{kB}$.

Since the variational ansatz is periodic with a two-site unit cell, the effective fermionic Hamiltonian (2.17) is also translationally invariant under translations by one enlarged unit cell. In order to find the energy contribution from the fermionic ground state $|\psi_f\rangle$, it's therefore convenient to diagonalize (2.17) in momentum space. Bloch's theorem [19] grants the existence of a bulk Hamiltonian $\hat{H}(k)$ in momentum space that satisfies:

$$\hat{H}_f = \sum_k \hat{\psi}_k^\dagger \hat{H}(k) \hat{\psi}_k, \tag{2.18}$$

where $\hat{\psi}_k = (\hat{c}_{kA}, \hat{c}_{kB})^T$. For the fermionic system of Eq. (2.12), its noninteracting fermions occupy single particle Bloch states $|k\rangle \otimes |u_{A,B}\rangle$. Bloch states are defined as $|k\rangle = \sum_j e^{-ikj} |j\rangle / \sqrt{L}$, where $|j\rangle$ identifies the wavefunction of a fermion localized in the $j-$th unit cell and $|u_{A,B}\rangle$ defines which site of the unit cell it localizes on.

By substituting back into Eq. (2.17), we rewrite our fermionic effective energy as:

$$\begin{aligned}
\hat{H}_f(s_A, s_B) &= -\sum_j \frac{1}{L} \sum_{kl} e^{i(k-l)j} \Big[(t + \alpha s_A)\, c_{kA}^\dagger c_{lB} e^{-il/2} + \\
&\qquad (t + \alpha s_B)\, c_{kB}^\dagger c_{lA} e^{il/2} + \text{H.C.} \Big] \\
&= -2 \sum_k \Big[(t + \alpha s_A)\, c_{kA}^\dagger c_{kB} e^{-ik/2} + (t + \alpha s_B)\, c_{kB}^\dagger c_{kA} e^{ik/2} + \text{H.C.} \Big] \\
&= -\sum_k (c_{kA}, c_{kB})^\dagger \left[\mathbf{v}(k) \cdot \boldsymbol{\sigma} \right] (c_{kA}, c_{kB})
\end{aligned} \tag{2.19}$$

where $\boldsymbol{\sigma} = (\sigma_x, \sigma_y, \sigma_z)$ is the Pauli vector and c.c. denotes the complex conjugate of the elements in parentheses.

The term summed over k gives us exactly the bulk hamiltonian $\hat{H}(k)$. The effective fermionic bulk Hamiltonian of Eq. (2.19) $\hat{H}(k) = \mathbf{v}(k) \cdot \boldsymbol{\sigma}$ is defined by

the vector:

$$\mathbf{v}(k) = \begin{pmatrix} (2t + \alpha s_A + \alpha s_B)\cos(k/2) \\ \alpha\,(s_A - s_B)\sin(k/2) \\ 0 \end{pmatrix} \tag{2.20}$$

Note that for a general vector $\mathbf{w} \in \mathbb{R}^3$ we have $(\mathbf{w}\cdot\boldsymbol{\sigma})^2 = |\mathbf{w}|^2\,\mathbb{I}$, thus our Bloch Hamiltonian $\hat{H}(k)$ has two energetic bands with opposite signs. The two fermionic energy bands are $E(k) = \pm\,|\mathbf{v}(k)|$:

$$E(k) = \pm 2t_{AB}\sqrt{1 - \left(1 - \frac{\alpha^2(s_A - s_B)^2}{4t_{AB}^2}\right)\sin^2(k/2)} \tag{2.21}$$

where we introduced $t_{AB} = t + \alpha\,(s_A + s_B)\,/2$. As shown in Figure 2.3, depending on the values of s_A, s_B the two bands are either gapless or gapped with energy gap equal to $\alpha\,|s_A - s_B|$.

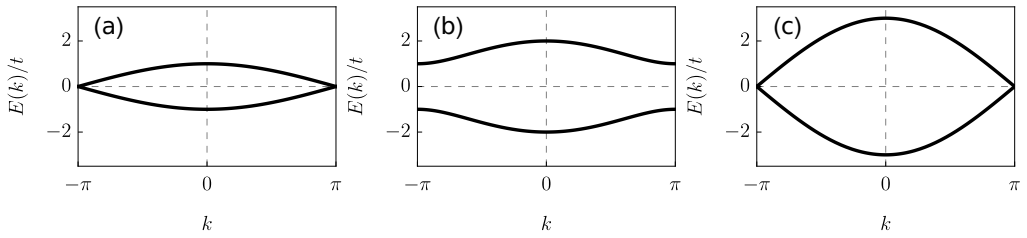

Figure 2.3: Energy bands of the bulk Hamiltonian $\hat{H}(k)$ across the first Brillouin zone for $\alpha = 0.5t$ and various values of the pair s_A, s_B. From left to right: (a) homogeneous spin phase with $s_A, s_B = -1$ and hopping strength equal to $-t+\alpha$. (b) staggered phase with $s_A = -s_B = 1$, alternating hopping strengths $-t \pm \alpha$ and nonzero gap of size $2\alpha = t$. (c) homogeneous spin phase with $s_A, s_B = 1$ and hopping strength equal to $-t - \alpha$. Gapped phases are insulating, gapless phases are conducting.

At half-filling, the ground state of a system of noninteracting fermions corresponds to a fully occupied lower energy band, since we have as many fermions as unit cells. Summing over the lower energy band we find the fermionic con-

tribution to the variational ansatz:

$$\begin{aligned} E_f &= -\sum_k |\mathbf{v}(k)| \\ &= -\sum_k 2t_{AB}\sqrt{1-\left(1-\frac{\alpha^2(s_A-s_B)^2}{4t_{AB}^2}\right)\sin^2(k/2)} \\ &= -\frac{L}{\pi}t_{AB}\int_{-\pi}^{\pi} dk\,\sqrt{1-\left(1-\delta_{AB}^2\right)\sin^2(k/2)} \\ &= -4L\frac{t_{AB}}{\pi}E\left(1-\delta_{AB}^2\right) \end{aligned} \tag{2.22}$$

Here we introduced the complete elliptic integral of the second kind:

$$E(x) = \int_0^{\pi/2} dk\,\sqrt{1-x\sin^2 k} \tag{2.23}$$

and, lastly, a parameter for the dimerization:

$$\delta_{AB} = \frac{\alpha(s_A-s_B)}{2t_{AB}} \tag{2.24}$$

This parameter is 0 when the spins are aligned $s_A = s_B$ and equals α/t when they are opposite $s_A = -s_B$ Notice that no gap in the bands is assumed at the moment.

The energy bands of Eq. (2.21) are similar to the ones of the topological insulator introduced in section 1.1 and reported in Figure 1.2, thus its topological invariants are the same.

Summing the result of Eq. (2.22) together with the spin contributions we find the energy of our ansatz, normalized to the number of unit cells L:

$$\epsilon(s_A,s_B) = -\frac{2}{\pi}t_{AB}E(1-\delta_{AB}^2) + \frac{\Delta}{4}(s_A+s_B) + \beta\left(a_Ab_A + a_Bb_B\right) \tag{2.25}$$

From this equation we can find the values of s_A, s_B which minimize the energy.

Since we included the dependence on the local spin wavefunction into the parameters $a_{l(i)}, b_{l(i)}$, the ansatz of Eq. (2.25) is completely agnostic on the nature of the local spin wavefunction, as long as the mean field approach holds. The advantage of using this notation is simple: if the nature of the local spin wavefunction changes we just add the relative additional parameters on which $s_{l(i)}$ depends. This assumption holds as long as the ground state is found in a product state of single spin sites. For example, the case presented in this chapter uses the constraints posed by Eq. (2.13) and the pair s_A, s_B depends only on four

real parameters $(a, b)_{A,B}$.

The case for spin-1/2 is straightforward: since we set $\beta \ll t$, the only possible allowed states of the local spin wavefunction are the eigenstates $|\uparrow\rangle, |\downarrow\rangle$ of the operator $\hat{\sigma}_z$. Then the only values allowed are $s_A = s_B = \pm 1$ and $s_A = -s_B = \pm 1$, and the energy of Eq. (2.25) has the same value for $(s_A, s_B) = (1, -1)$ and $(s_A, s_B) = (-1, 1)$. The energy term proportional to β vanishes since for $s_{l(i)} = +1$ we have $b_{l(i)} = 0$ while for $s_{l(i)} = -1$ we have $a_{l(i)} = 0$.

A direct calculation of these three energies and a confrontation of their values shows that we have three regions in the parameter space Δ, α, as in Figure 2.4. Two uniform regions, corresponding to $s_A = s_B = \pm 1$ and spin states $|\uparrow\uparrow \ldots\rangle$ or $|\downarrow\downarrow \ldots\rangle$, are separated by one region of alternating spins with $s_A = -s_B$, the Néel ordered region $|\uparrow\downarrow \ldots\rangle$.

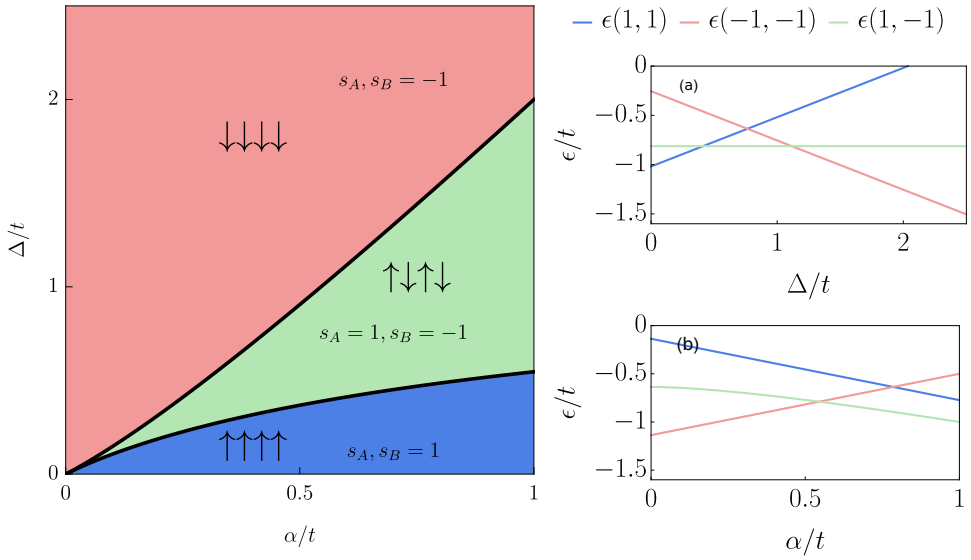

Figure 2.4: Mean-field results obtained from the Born-Oppenheimer ansatz. Left: the parameter space features three different regions hosting different ground states. The top (red) and bottom (blue) regions host translationally invariant ground states where spins feature ferromagnetic order and either $|\uparrow\rangle$ (for $s_A, s_B = 1$) or $|\downarrow\rangle$ (for $s_A, s_B = -1$) separable states. The central (green) regions shows spontaneous breaking of translational invariance, with alternating $|\uparrow\rangle, |\downarrow\rangle$ separable spins. Right: energy levels for different configurations across (a) a vertical cut for $\alpha = 0.6t$ and (b) a horizontal cut for $\Delta = 1.0t$ of the parameter space.

We report the energies of the uniform regions:

$$\epsilon(1,1) = -\frac{2}{\pi}(t+\alpha) + \frac{\Delta}{2} \tag{2.26}$$

$$\epsilon(-1,-1) = -\frac{2}{\pi}(t-\alpha) - \frac{\Delta}{2} \tag{2.27}$$

and of the Néel ordered region:

$$\epsilon(1,-1) = -\frac{2}{\pi} tE\left(1 - \frac{\alpha^2}{t^2}\right) \tag{2.28}$$

Confronting their values we find the critical lines $\Delta_\pm(\alpha)$ separating them:

$$\Delta_\pm(\alpha) = \frac{4t}{\pi}\left[\frac{\alpha}{t} \pm E\left(1 - \frac{\alpha^2}{t^2}\right) \mp 1\right] \tag{2.29}$$

where Δ_+ is the boundary between the Néel region and the uniform $|\downarrow\rangle$ one, while Δ_- separates the uniformly ordered $|\uparrow\rangle$ phase from the Néel phase. At the mean-field level the ansatz predicts that in the regions $\alpha \geq 0, \Delta < 0$ and $\alpha \leq 0, \Delta > 0$ the ground state is found in the two uniform configurations $|\uparrow\uparrow \ldots\rangle$ and $|\downarrow\downarrow \ldots\rangle$ respectively.

In chapter 3 we introduce the theory behind spin-1 sites and in chapter 4 we present a variation of the Hamiltonian in Eq. (2.11). As long as the spin wavefunction is site-factorizable the different Hamiltonian will display a similar behavior to the one found here. Then we choose a single site spin-1 wavefunction depending on real parameters $|\psi_s\rangle_j = a_j |+1\rangle + b_j |0\rangle + c_j |-1\rangle$ and still obtain the variational ansatz of Eq. (2.25) with s_j now depending on (a_j, b_j, c_j).

In appendix Appendix A, we report on a generalization of the following variational minimization to systems with spin sites of generic spin length. We conclude that the same results found for spin-$1/2$ systems hold for spin-1 and more generic spin-N systems built from (2.11) as long as $\beta = 0$.

2.3.b Numerical results for the spin-$1/2$ case

In order to study numerically the behavior of the full model in Eq. (2.11), we implement the Hamiltonian using `QuSpin` [35] and study a lattice of $L = 6$ sites with exact diagonalization. The periodic chain of 6 bosonic sites has 3 bosons on it, with self-energy $U = 20t$. This value shows to be enough to preserve the hardcore bosons regime on the ground state, thus we also restrict the local bosonic Hilbert space to host at maximum one boson.

Due to the periodicity of the chain, in the Néel region where the ground state is

bipartite its wavefunction is a quantum superposition of both symmetry broken states, characterized by their spin wavefunctions $|\uparrow\downarrow\uparrow\downarrow\uparrow\downarrow\rangle$ and $|\downarrow\uparrow\downarrow\uparrow\downarrow\uparrow\rangle$. In order to study each symmetry broken configuration, we introduce a small artificial perturbation which selects one of the two Néel states:

$$H_\epsilon = \epsilon \sum_i (-1)^i \hat{\sigma}^z_{l(i)} \tag{2.30}$$

with $\epsilon \ll t$.

Simulations were made in the region of the space of parameters with $\alpha \in [0, t]$ and $\Delta \in [0, 2.5t]$, for values of $\beta \in \{0, 0.05t\}$. The first numerical analysis is for $\beta = 0$ and $\epsilon = 0.001t$, which allows us to study the two uniform configurations and one symmetry broken state. Then we turn on $\beta = 0.05t$ and turn off ϵ to study the quantum correlations on the ground state.

Before discussing the full phase diagram, we first show representative ground-state configurations obtained from exact diagonalization. These configurations reproduce the uniform and dimerized spin backgrounds anticipated by the mean-field analysis of the previous section and are reported in Figure 2.5. Spins are either in a uniform $|\uparrow\rangle$ or $|\downarrow\rangle$ configuration, with uniform $-t \pm \alpha$ hoppings, or in a Néel configuration of alternating $|\uparrow\rangle, |\downarrow\rangle$ states with staggered bosonic hoppings. The two degenerate symmetry broken states are connected by translation of a single site of the whole periodic chain.

Since the Peierls transition leads to a staggering of both bosonic hoppings $\hat{B}_{l(i)}$ and of spin orientations $\hat{\sigma}^z_{l(i)}$, we compute two order parameters for the symmetry broken regions: the staggered hopping amplitude $\hat{\sigma}_B$

$$\hat{\sigma}_B = \frac{1}{L} \sum_i (-1)^i \hat{B}_{l(i)} \tag{2.31}$$

and the staggered magnetization $\hat{\sigma}_N$

$$\hat{\sigma}_N = \frac{1}{L} \sum_i (-1)^i \hat{\sigma}^z_{l(i)}. \tag{2.32}$$

Measuring the values of these two observables on the ground state we find the regions of Figure 2.6. The critical lines of Eq. (2.29) accurately reproduce the numerical boundaries between the different phases for $\beta = 0$, where the mean field ansatz is indeed justified.

In order to verify numerically the hypothesis of the mean field ansatz, we measure the entanglement entropy between the bosonic and spin-1/2 sectors $S_E = -\mathrm{Tr}\left[\rho_s \log \rho_s\right]$ where $\rho_s = \mathrm{Tr}_b\left[\rho\right]$ is the reduced density matrix of the spins

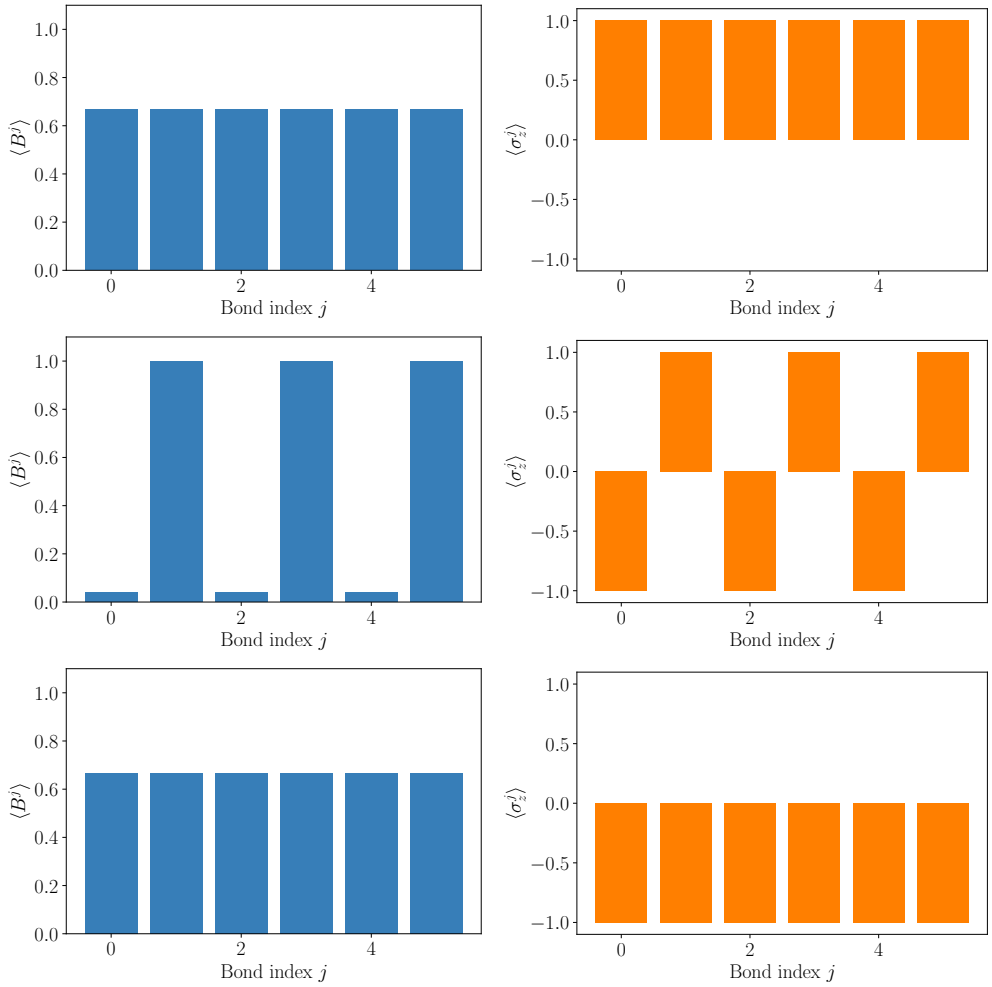

Figure 2.5: Expectation values for each spin $\hat{\sigma}_j^z$ on the jth bond (right panels) and bosonic hopping amplitudes $\hat{B}_j$ along the chain (left panels) for three points of the configuration space. Here $\beta = 0t$, $\alpha = 0.8t$ and $\epsilon = 0.001t$. Top: for $\Delta = 0.6t$, the spins are all in a uniform configuration and bosons hop uniformly along the chain with strength $-t - \alpha$. Middle: for $\Delta = 1.2t$ we are in the Néel region where spins form an alternating pattern. The bosonic hoppings dimerize accordingly with values $-t \pm \alpha$. Bottom: for $\Delta = 1.8t$ the spins are in a ferromagnetic configuration and the bosonic hopping is uniform and equals $-t + \alpha$.

and Tr_b denotes a partial trace of the ground state density matrix ρ over the full bosonic Hilbert space. We also compute the purity $\mathrm{Tr}\rho_{ss}^2$ of the reduced density matrix of a single spin-1/2 site, $\rho_{ss} = \mathrm{Tr}'[\rho_s]$. The partial trace Tr' is taken over all spin-1/2 degrees of freedom except for one. If the ground state obeys the hypotheses of the variational ansatz, which requires separability in its bosonic and single spin-1/2 sectors, the purity of ρ_{ss} is expected to be exactly equal to 1.

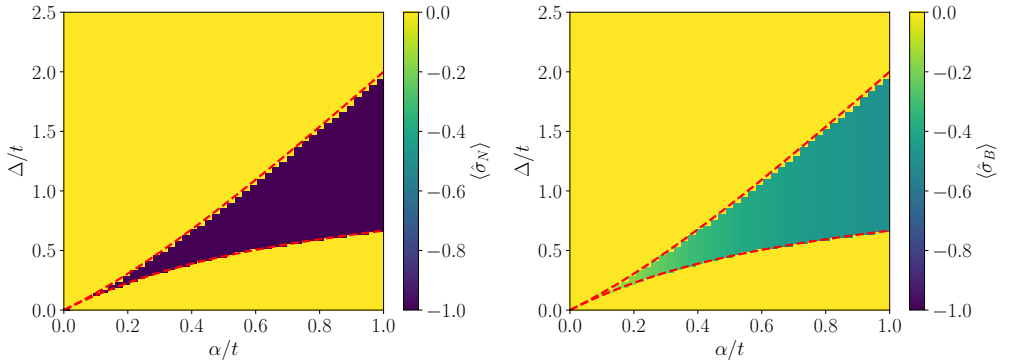

Figure 2.6: Phase space for the region $\alpha \in [0, t]$, $\Delta \in [0, 2.5t]$, $\beta = 0$. Simulations were run with $\epsilon = 0.001t$ which selects the periodic, symmetry broken spin state $|{\downarrow}{\uparrow}{\downarrow}{\uparrow}{\downarrow}{\uparrow}\rangle$ in the dimerized region. Expected values on the ground state for the staggered spin magnetization $\hat{\sigma}_N$ (left) and staggered hopping amplitude $\hat{\sigma}_B$ (right). The yellow regions identify uniform configurations where translational invariance of the periodic chain is preserved. The central region instead are symmetry broken regions where spins are Néel ordered and bosons show bond-density waves. The red dashed lines are the critical values of $\Delta_\pm$ found with the variational mean-field ansatz in Eq.(2.29).

As expected for the $\beta = 0$ case, the ground state is forced by the local $\hat{\sigma}_z$ symmetry to be a product state and Figure 2.7 confirms the validity of the ansatz.

After selecting a vertical cut $\alpha = 0.9t$ along the phase space in Figure 2.6, we look at the energy difference in between the lowest excited states and the ground state. From the energy gaps of Figure 2.8 it's clear that the Néel region is characterized by a two-fold degenerate ground state. The transition from the two uniform regions to the degenerate symmetry broken one is an exact level crossing for $\beta = 0$ because, as highlighted in subsection 2.3.a, the three configurations live in different symmetry sectors.

Furthermore, by evaluating $\langle\hat{\sigma}^z_j\rangle$, $\langle\hat{\sigma}^x_j\rangle$ and $\langle\hat{B}_j\rangle$ on two adjacent bonds $j = 0, j = 1$ in Figure 2.9 we find further marks of the dimerized configuration.

Having established the behavior of the system in the adiabatic limit, we break the local $\hat{\sigma}^z_{l(i)}$ symmetry by setting $\beta = 0.05t$. The two symmetry broken Néel regions are now connected by quantum fluctuations over the two dimerized ground states. The absence of the local symmetry hinders the breaking of translational symmetry, as can be seen in Figure 2.10. We consider first having a small $\epsilon \neq 0$, such that we select one of the two hybridized ground states in the dimerized region.

The entanglement entropy S_E and the purity of the reduced density matrix $\mathrm{Tr}\rho^2$ are in Figure 2.11 and are peaked at the transitions in between phases. As confirmed from the boson-spin entanglement entropy and the single-spin purity

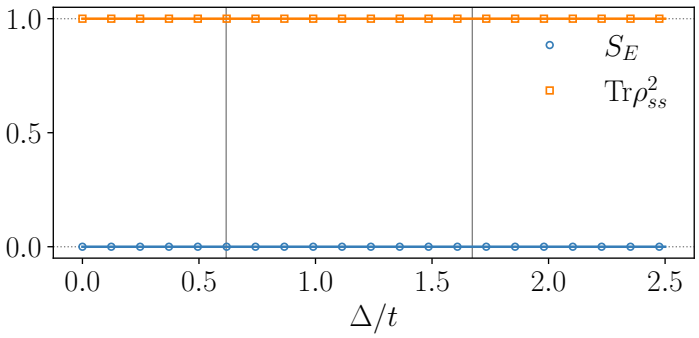

Figure 2.7: Entanglement entropy S_E and RDM purity $\mathrm{Tr}\rho_{ss}^2$ for two bipartitions of the chain along the vertical cut corresponding to $\alpha = 0.9t$, $\Delta \in [0, 2.5t]$, $\beta = 0$ and $\epsilon = 0.001t$. The entanglement entropy S_E is computed in between bosonic and spin-1/2 degrees of freedom (circles), while $\mathrm{Tr}\rho_{ss}^2$ is the purity of the reduced density matrix of a single spin-1/2 after tracing all other degrees of freedom.

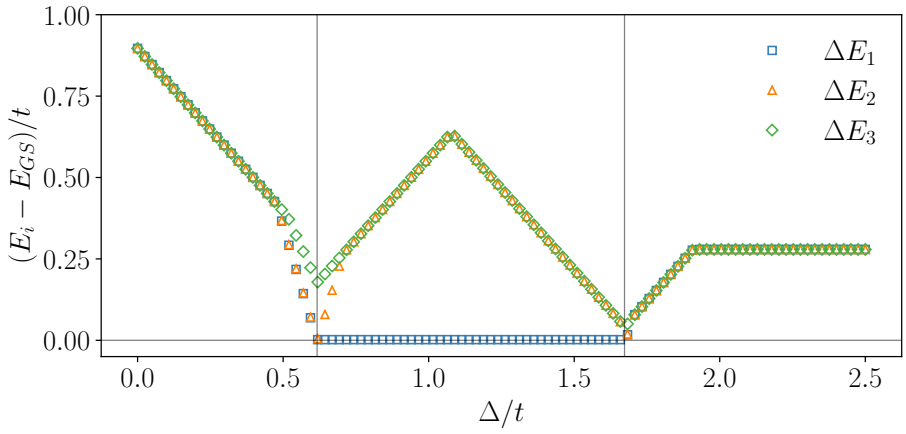

Figure 2.8: Energy difference in between the first three excited levels and the ground state for $\alpha = 0.9t$, $\Delta \in [0, 2.5t]$, $\beta = 0$ and $\epsilon = 0t$. Vertical lines mark the critical values $\Delta_\pm$ for $\alpha = 0.9t$ found with the variational ansatz. The central region features a twofold degenerate ground state as ΔE_1 is zero.

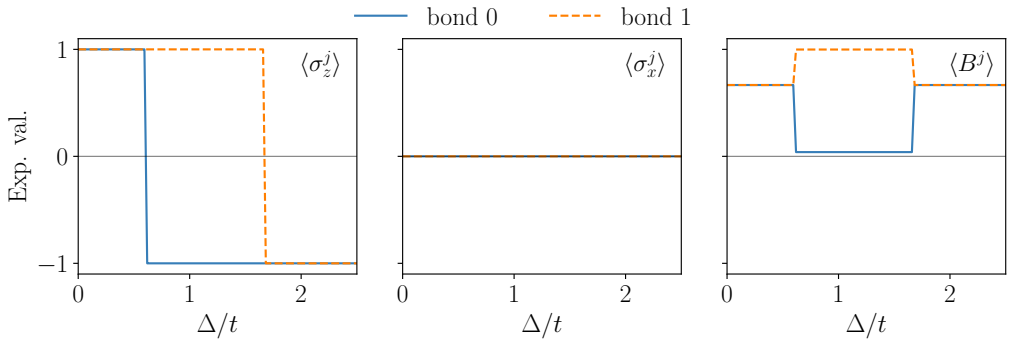

Figure 2.9: Expectation values of three local operators for $\alpha = 0.9$, $\Delta \in [0, 2.5t]$, $\beta = 0$ and $\epsilon = 0.001t$. From left to right we have $\hat{\sigma}_j^z$, $\hat{\sigma}_j^x$ and the bond hopping strength $\hat{B}_j$. The selected Néel configuration shows different expectation values on odd-even sites.

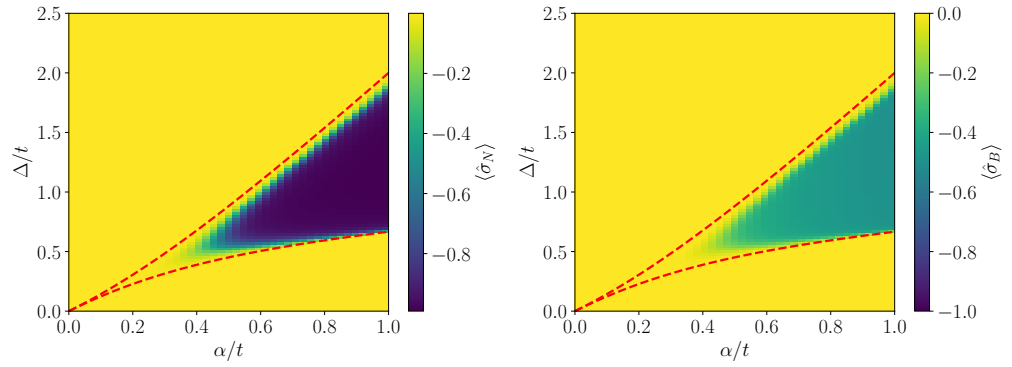

Figure 2.10: Phase space for the region $\alpha \in [0, t]$, $\Delta \in [0, 2.5t]$, $\beta = 0.05t$. Simulations were run with $\epsilon = 0.001t$ which selects the periodic, symmetry broken spin state $|\downarrow\uparrow\downarrow\uparrow\downarrow\uparrow\rangle$. Expected values on the ground state for the staggered spin magnetization $\hat{\sigma}_N$ (left) and staggered hopping amplitude $\hat{s}_B$ (right). The critical lines $\Delta_\pm$, valid for the $\beta = 0$ case, show that the Néel region shrinks as disorder increases.

behavior along the vertical cut in Figure 2.12, the mean field ansatz is still a good approximation for this value of β, but only far from the level crossing.

The lowest energy levels are plotted in Figure 2.13.

The graphs of Figure 2.10 show that the Néel order is preserved despite the absence of a protecting symmetry, but also show that the Néel region shrinks from the one in Figure 2.6 as the wavefunction smoothly passes from one configuration to the other. As a consequence, the dimerization of odd-even sites is still present in the Néel ordered region, but disappears smoothly as we cross its borders: Figure 2.14.

We now turn off the splitting perturbation $\hat{H}_\epsilon$. At difference with the adiabatic $\beta = 0$ limit, with no protecting symmetry and no artificial splitting the two

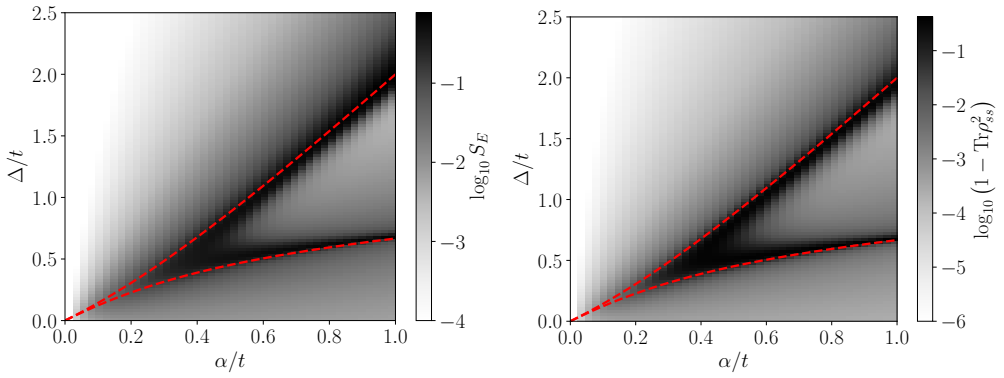

Figure 2.11: Entanglement entropy S_E between bosonic and spin-1/2 sites and RDM purity $\mathrm{Tr}\rho_{ss}^2$ of a single spin. For $\beta = 0.05t$ and $\epsilon = 0.001t$, quantum fluctuations increase in the proximity of the critical lines $\Delta_\pm$ (red), where Néel states are energetically close to the uniform regions.

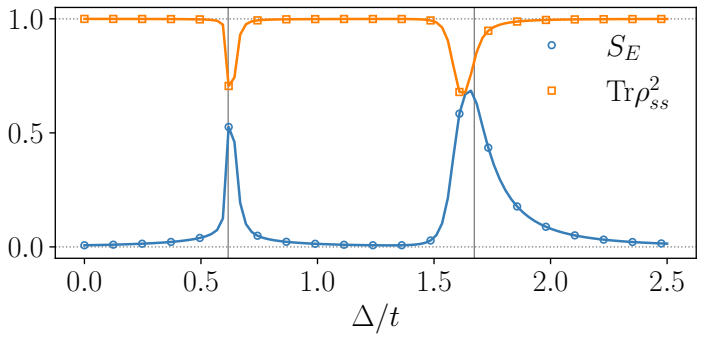

Figure 2.12: Entanglement entropy S_E and RDM purity $\mathrm{Tr}\rho_{ss}^2$ for two bipartitions of the chain. The plotted region of the phase space corresponds to $\alpha = 0.9t$, $\Delta \in [0, 2.5t]$, $\beta = 0.05$ and $\epsilon = 0.001t$.

degenerate symmetry broken ground states hybridize. Thus, for a finite size system at $\epsilon = 0$, the exact ground state is expected to be a superposition of the two symmetry-broken branches.

The separable mean-field ansatz does not capture this finite-size superposition and the associated long-range correlations dominating in the Néel region. However, this should not be interpreted as a complete breakdown of the mean-field picture. The ansatz remains an effective description of each individual symmetry broken state, selected by an infinitesimal staggered term or in the thermodynamic limit. The entanglement entropy S_E and the purity $\mathrm{Tr}\rho_{ss}^2$ are plotted in Figure 2.16 along the aforementioned vertical cut.

Furthermore, the hybrid Néel ground state shows nontrivial quantum correlations in the symmetry broken phases. The connected correlators $\langle \hat{\sigma}_0^z \hat{\sigma}_l^z \rangle_C =$

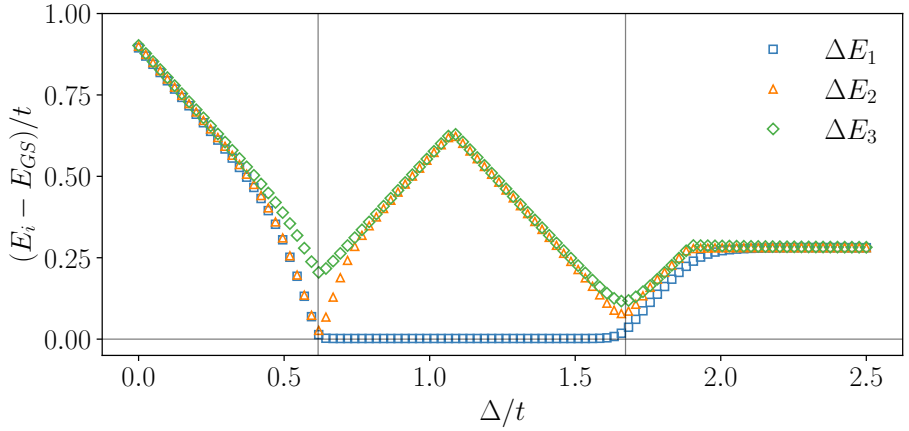

Figure 2.13: Energy difference in between the first three excited levels and the ground state for $\alpha = 0.9t$, $\Delta \in [0, 2.5t]$, $\beta = 0.05t$ and $\epsilon = 0t$. Vertical lines mark the critical values $\Delta_\pm$ for $\alpha = 0.9t$ found with the variational ansatz.

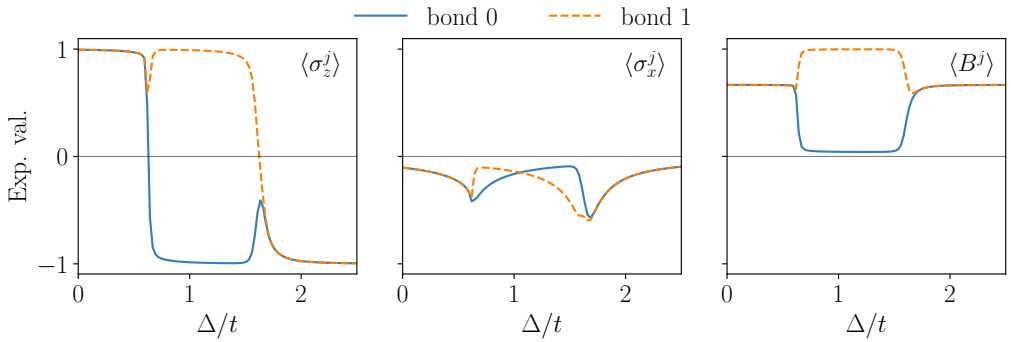

Figure 2.14: Expectation values of three local operators for $\alpha = 0.9t$, $\Delta \in [0, 2.5t]$, $\beta = 0.05t$ and $\epsilon = 0.001t$. From left to right: $\hat{\sigma}^z_{l(i)}$, $\hat{\sigma}^x_{l(i)}$ and the bond hopping strength $\hat{B}_{l(i)}$.

$\langle\hat{\sigma}^z_0\hat{\sigma}^z_l\rangle - \langle\hat{\sigma}^z_0\rangle\langle\hat{\sigma}^z_l\rangle$ depicted in Figure 2.17 highlight how the uniform regions are still characterized by separable states. Furthermore, despite the absence of a protecting symmetry we find that the hybridized ground state still shows clear anticorrelations between odd-even sites in the Néel region.

2.3.c Topology of the SSH model and edge states

In this last section we delve into how and why the Hamiltonian of Eq. (2.11) features topological phases of matter in its ground state. In particular, we highlight the connection between the physics and topology of the SSH model presented in section 1.1 and the model introduced in this chapter.

As follows from Eq. (2.19), in the hard-core boson limit the final form of the

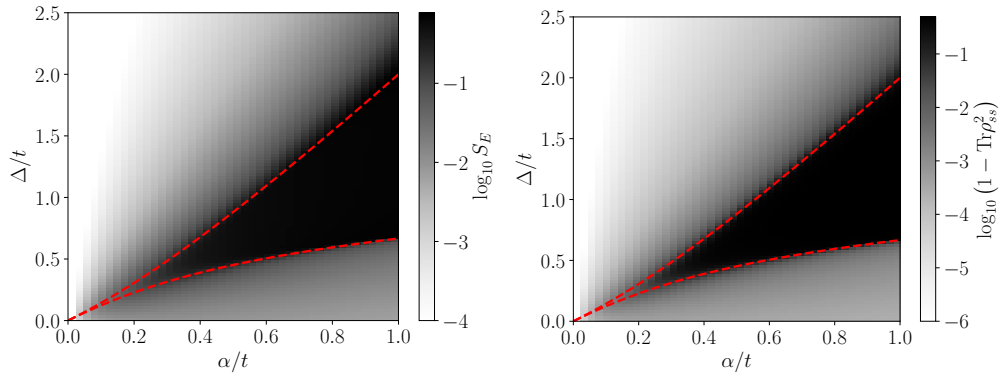

Figure 2.15: Entanglement entropy S_E between bosonic and spin-1/2 sites and purity of the reduced density matrix $\mathrm{Tr}\rho_{ss}^2$ of a single spin. With $\epsilon = 0t$ and $\beta = 0.05t$, Néel states hybridize and the mean-field ansatz is not an exact description of the ground state.

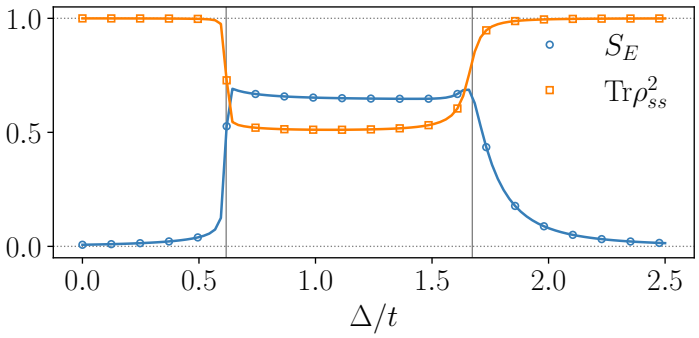

Figure 2.16: Entanglement entropy S_E between bosonic and spin-1/2 sites and purity of the reduced density matrix $\mathrm{Tr}\rho_{ss}^2$ of a single spin. The plotted region of the phase space corresponds to $\alpha = 0.9t$, $\Delta \in [0, 2.5t]$, $\beta = 0.05t$ and $\epsilon = 0t$.

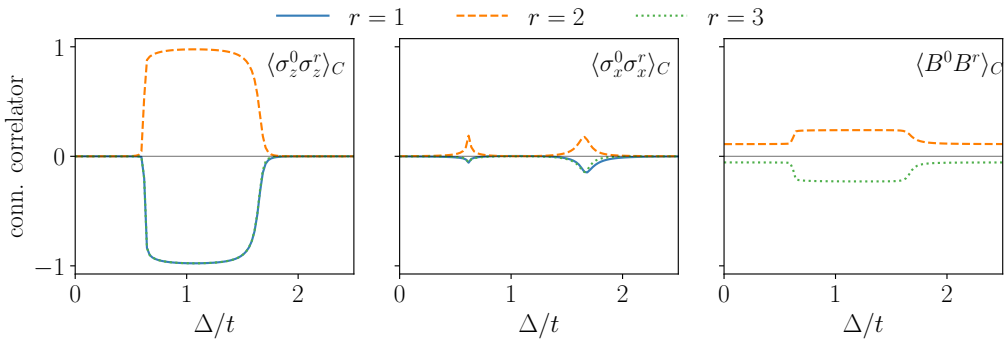

Figure 2.17: Connected correlators along the vertical cut for $\alpha = 0.9t$, $\Delta \in [0, 2.5t]$, $\beta = 0.05t$ and $\epsilon = 0t$.

variational ground state energy can be written as the sum of the occupied single particle energy levels proportional to the vector modulus $|\mathbf{v}(k)|$ over the first Brillouin zone, plus an additional contribution proportional to Δ and to the total magnetization. Comparing this to the results introduced in the previous chapter we highlight that, in that limit, the effective bosonic Hamiltonian maps to the many body SSH Hamiltonian, up to constant terms. The spin-boson interaction coupling α leads to an interaction-induced topological effective bosonic SSH Hamiltonian, of which the Hamiltonian of Eq. (2.11) inherits the topological properties.

A paradigmatic example of these topological properties is the ability of Eq. (2.11) to hold localized zero-energy modes in the symmetry broken Peierls phase. The following numerical study involves an open chain of 12 bosonic and 11 spin-1/2 sites, filled with 5 and 7 hardcore bosons, corresponding to one particle below and one particle above half filling. In the topological dimerized sector, this filling anomaly is accommodated by the emergence of edge-localized modes, as shown in Figure 2.18.

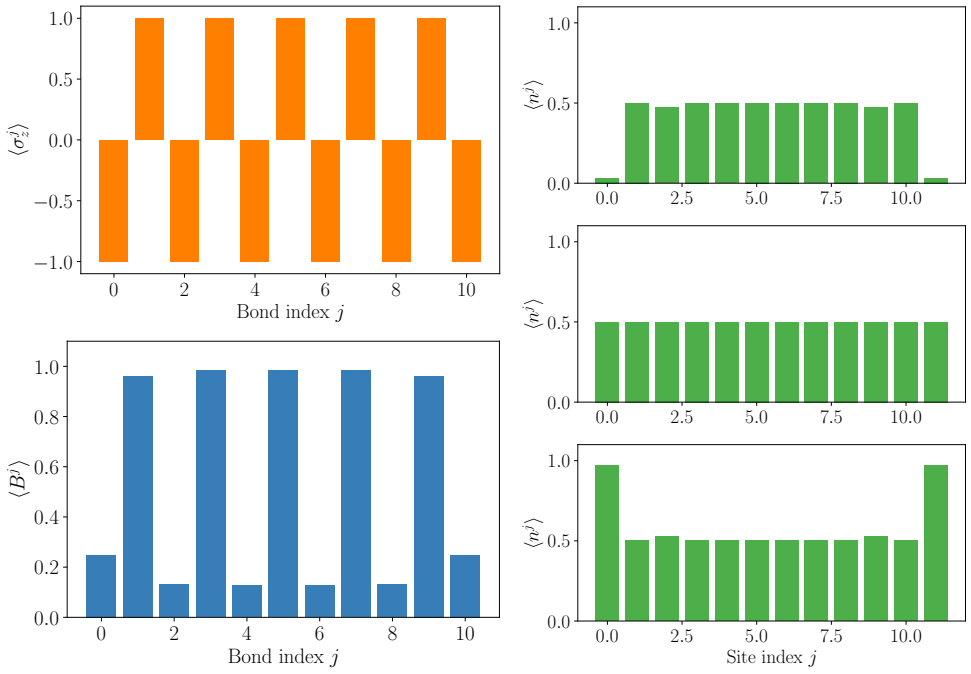

Figure 2.18: Local observables along the open chain for $\alpha = 0.6t$, $\Delta = 0.8t$, $\beta = 0t$ and $\epsilon = 0$ on the nontrivial excited state. Left: expectation values for the spin-1/2 $\hat{\sigma}^z_{l(i)}$ component (top) and for the hopping amplitude $\hat{B}_{l(i)}$ (bottom) show that the edges have weak hoppings. Right: local bosonic densities along the chain for 5 (top), 6 (middle) and 7 (bottom) bosons. Filling anomalies lead to the emergence of localized zero energy edge modes.

The bulk Hamiltonian of (2.19) is similar to the bulk Hamiltonian of the SSH model introduced in the previous chapter. The winding number and the Berry phase are computed in exactly the same way as for the original SSH model [20], thus confirming that the model of Eq. (2.11) presents two distinct and topologically disconnected symmetry broken phases. The existence of zero energy edge modes is a consequence of the bulk-boundary correspondence inherited from the SSH model, with some relevant differences which are to be addressed.

In the original SSH model of section 1.1, the hopping parameters J, J' determine whether the ground state of an open chain hosts zero energy edge modes or not. The two parameters J, J' are fixed and thus the ground state of the Hamiltonian of Chapter 1 either hosts edge modes or it doesn't if it's topologically trivial.

In the Hamiltonian of Eq. (2.11) the effective hopping parameters $t+\alpha, t-\alpha$ instead emerge from the interaction of the bosonic and spin degrees of freedom. For an open chain, one symmetry-broken dimerized state starts and ends with a strong $-t-\alpha$ hopping strength, we refer to its spin wavefunction as $|\uparrow\downarrow \dots \downarrow\uparrow\rangle$. Its spin configuration, starting and ending with $|\uparrow\rangle$ states, leads to a bosonic effective Hamiltonian equivalent to the trivial configuration of the SSH model. The chain in this state, reported in Figure 2.19, does not feature zero-energy edge modes and thus is trivial.

The eigenstate which instead starts with a weak bond $-t+\alpha$, $|\downarrow\uparrow \dots \uparrow\downarrow\rangle$, has a separable spin configuration which starts and ends with a $|\downarrow\rangle$ state. The effective bosonic Hamiltonian corresponds to the topological one of section 1.1 and this state features the zero-energy edge modes of Figure 2.18. For this reason, this state is nontrivial and topologically disconnected from the trivial one.

For an open chain the two symmetry broken configurations are not degenerate for the model in Eq. (2.12). Finite size effects increase the energy of the dimerized configuration which starts with a weak bond $t-\alpha$, the topological one. As we prove in the following, of the two symmetry broken configurations, the trivial one is the ground state which shows a strong hopping $-t-\alpha$ at its edges.

Due to our interest in the study of topological phenomena and the bulk-boundary correspondence, we report some considerations on the experimental feasibility of the study of said nontrivial state.

For the case $\beta = 0$, the fact that the nontrivial state is an excited state is not a problem. Suppose that an experimental setup prepares a quantum system in such state: since the local spin degrees of freedom are completely frozen in the adiabatic limit, the effective bosonic Hamiltonian is exactly the one of the topological SSH model and the system inherits its properties.

For $\beta \ll t$ instead the nontrivial topological state is not protected by the

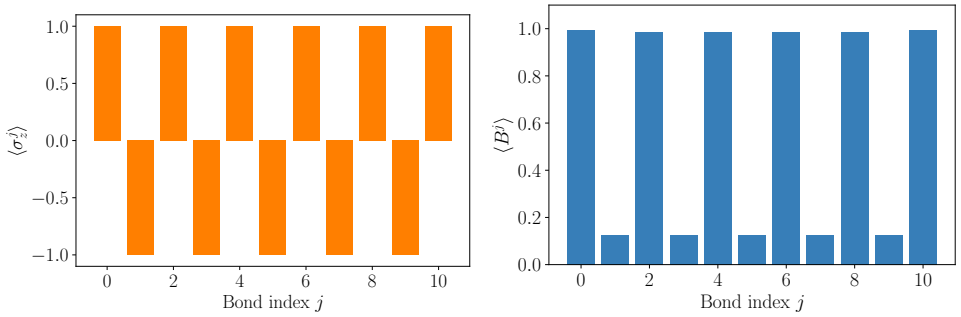

Figure 2.19: Ground state of the open chain for $\alpha = 0.6t$, $\Delta = 0.8t$, $\beta = 0t$ and $\epsilon = 0t$. The bond at the edges of the chain has value $-t - \alpha$.

local σ_j^z symmetry and is allowed to transition and evolve towards the real ground state, corresponding to the trivial SSH configuration introduced in the previous chapter. As shown by González-Cuadra et al. even in these conditions topological order survives [20]. Furthermore, these transitions or mixing of the nontrivial state are hindered by the length of the chain: the two non-trivial and trivial symmetry broken spin configurations are connected by an extensive number of spin-flips.

Another relevant criticality to be addressed is the necessity for the nontrivial state of a local protecting symmetry. For $\beta = 0$, fixing the global magnetization sector $\hat{M} = \sum_j \hat{\sigma}_j^z$ is not enough to find the nontrivial state $|{\downarrow}{\uparrow}\ldots{\uparrow}{\downarrow}\rangle$ in the ground state. Even in the global magnetization sector $\langle \hat{M} \rangle = -1$, which hosts $|{\downarrow}{\uparrow}\ldots{\uparrow}{\downarrow}\rangle$, this state is an excited state separated from the ground state by a dense and extensive number of intermediate states. These are spin configurations obtained from the trivial one of Figure 2.19 with an odd number of spins flipped, see for example Figure 2.21. The number of spin-flips must be odd since $|{\uparrow}\ldots{\uparrow}\rangle$ lives in a different symmetry sector, $\langle \hat{M} \rangle = +1$. Furthermore, due to the inversion symmetry of an open chain, the possible spin-flipped configurations are always at least twofold degenerate depending on the chain length.

For an open chain of 12 bosonic, 11 spin-1/2 sites we report in Figure 2.20 the lowest energy eigenstates for a system without symmetry restrictions and for a chain with total fixed magnetization $\langle \hat{M} \rangle = -1$ with $\beta = 0t$. We highlight the position of the excited nontrivial state $|{\downarrow}{\uparrow}\ldots{\uparrow}{\downarrow}\rangle$ and report in Figure 2.21 one of the lower-energy configurations obtained from the trivial state with the application of three spin-flips. Since the number of possible odd spin-flips grows linearly with the chain size, we conclude that the number of intermediate states in between the trivial configuration and the nontrivial one grows extensively.

All the aforementioned criticalities can be solved with the addition of a strong staggered ordering field, both for $\beta = 0$ and for $\beta \ll 1$. The addition of an order-

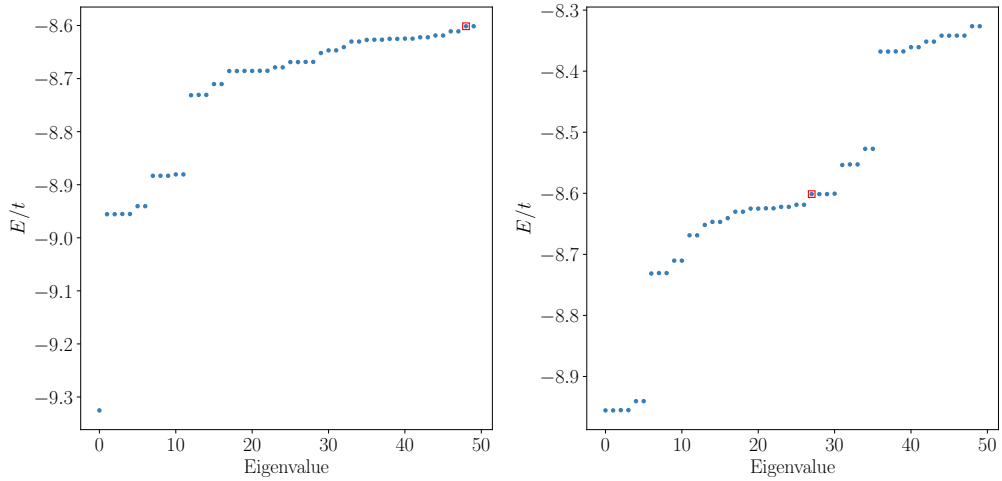

Figure 2.20: Lowest 50 energies for $\alpha = 0.6t$, $\Delta = 0.8t$, $\beta = 0t$ and $\epsilon = 0t$ on an open chain of 12 bosonic and 11 spin-1/2 sites. The nontrivial state $|{\downarrow\uparrow}\ldots{\uparrow\downarrow}\rangle$, marked with a red square, is an excited state for both the unrestricted Hamiltonian (left) and for the system projected on its global symmetry sector $\langle\hat{M}\rangle = -1$ (right).

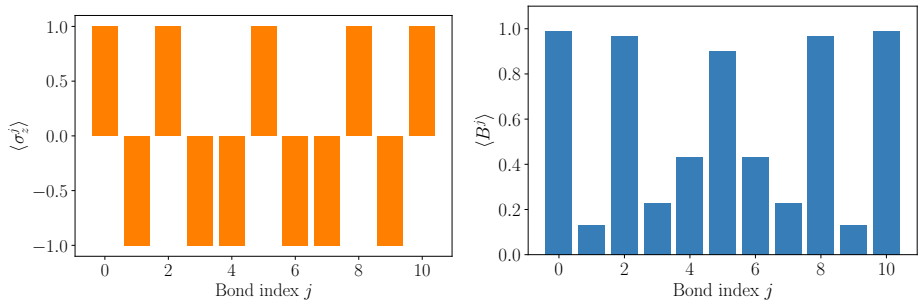

Figure 2.21: The sixth lowest eigenstate of the Hamiltonian restricted to the magnetization sector $\langle\hat{M}\rangle = -1$ for $\alpha = 0.6t$, $\Delta = 0.8t$, $\beta = 0t$ and $\epsilon = 0t$.

ing field as (2.30), with a high enough value of ϵ penalizes both the spin-flipped configurations and the trivial ground state. This solution requires experimental control over each individual local spin degree of freedom.

3 Spin-1 systems and quadrupoles

In the previous chapters we presented the capabilities of quantum simulation technologies and the physics of the Peierls transition in fermionic systems. Building from previous works [23, 20] we presented an interacting bosonic and spin-$1/2$ model able to mimic the physics of the Peierls transition in a quantum simulation framework. Recent progress in quantum simulation techniques made possible the realization of spin-1 Hamiltonians, leading the way to beyond-qbit studies. As an example, experimental setups using Rydberg arrays and ultracold atoms in optical lattices were able to emulate the physics of the spin-1 Haldane chains [12, 36].

In the following chapter we introduce spin-1 states and the set of quadratic spin operators $\hat{S}_\alpha \hat{S}_\beta$ for $\alpha, \beta \in \{x, y, z\}$. Furthermore, we highlight the connection of the latter to the second moment distribution of measurements of spin-1 wavefunctions.

From the decomposition in irreducible components of the axes of rotation we identify the traceless and symmetric rank-2 tensor $\hat{Q}_{\alpha\beta}$, referred to as the quadrupolar tensor. We study the behavior of $\hat{Q}_{\alpha\beta}$ for specific spin-$1/2$ and spin-1 pure states to highlight the richer phenomenology the spin-1 representation offers and its connection to time reversal symmetry. In the final part of the chapter, we present a parametrization of spin-1 wavefunctions using a two-vector representation $\mathbf{u}, \mathbf{v}$ and show that all pure spin-1 states form a continuous range of states with maximal spin vector length $\langle \hat{\mathbf{S}} \rangle^2 = 1$ and states with vanishing spin polarization $\langle \hat{\mathbf{S}} \rangle = 0$ but nonzero quadrupolar order $\langle \hat{Q}_{\alpha\beta} \rangle$. Following previous works [37], the former are referred to as coherent (or dipolar) states, while the latter are nematic (or quadrupolar) states.

3.1 Single spin fluctuations

For a generic single spin-N system, its Hilbert space has dimension $2N+1$ while all possible physically relevant operators acting on this space are represented as Hermitian matrices of size $(2N+1)\times(2N+1)$. These matrices generate a vector space with dimension $(2N+1)^2$, so we can choose a set of $(2N+1)^2$ linearly independent matrices which will act as its basis.

A convenient choice of basis is the following: the first four elements are given by the identity and three matrices representing the three spin operators: $\mathbb{I}$, $\hat{S}_x, \hat{S}_y, \hat{S}_z$. With these four operators, we already saturate the space generated by a single spin-$1/2$, which has dimension of $(2N+1)^2 = 4$.

For higher spins $S \geq 1$ we must include higher order combinations of the spin operators, the first of which are nine quadratic terms in the form $\hat{S}_\alpha \hat{S}_\beta$ for $\alpha, \beta \in \{x, y, z\}$. Due to the structure of the Lie algebra $\mathfrak{su}(2)$, only some quadratic terms are linearly independent of the four operators we already chose. In fact, the nine quadratic terms can be decomposed according to their transformation properties under rotations of the spin axes as follows:

- A single scalar contribution, given by $\hat{S}_x^2 + \hat{S}_y^2 + \hat{S}_z^2 = \hat{\mathbf{S}}^2$. For single spin states, this contribution is proportional to the identity since the operator $\hat{\mathbf{S}}^2$ is the quadratic Casimir of the $SU(2)$ group and fixes the representation in use.

- Three linearly independent antisymmetric combinations, which are the commutators $\left[\hat{S}_\alpha, \hat{S}_\beta\right]$. These terms do not introduce independent components from the ones already included in the basis. Indeed, given the $\mathfrak{su}(2)$ algebra, they correspond to the spin operators $\hat{S}_x, \hat{S}_y, \hat{S}_z$ and transform as vectors (rank-1 tensor) when rotating the axes.

- Five linearly independent contributions that form the elements of a rank-2 symmetric traceless tensor $Q_{\alpha\beta}$, also known as quadrupolar (or nematic) tensor.

For a generic spin-N representation with $N \geq 1$, the symmetric and traceless rank-2 components are nontrivial and must be included in the operator basis for the observables.

The entries of the rank-2 symmetric traceless tensor are chosen to be the

following, which define the quadrupolar tensor $\hat{Q}_{\alpha\beta}$:

$$\begin{aligned}\hat{Q}_{\alpha\beta} &= \frac{1}{2}\left\{\hat{S}_\alpha, \hat{S}_\beta\right\} - \frac{1}{3}\delta_{\alpha\beta}\hat{\mathbf{S}}^2 \\ &= \begin{pmatrix} \hat{S}_x^2 - \frac{1}{3}\hat{\mathbf{S}}^2 & \frac{1}{2}\left\{\hat{S}_x, \hat{S}_y\right\} & \frac{1}{2}\left\{\hat{S}_x, \hat{S}_z\right\} \\ \frac{1}{2}\left\{\hat{S}_y, \hat{S}_x\right\} & \hat{S}_y^2 - \frac{1}{3}\hat{\mathbf{S}}^2 & \frac{1}{2}\left\{\hat{S}_y, \hat{S}_z\right\} \\ \frac{1}{2}\left\{\hat{S}_z, \hat{S}_x\right\} & \frac{1}{2}\left\{\hat{S}_z, \hat{S}_y\right\} & \hat{S}_z^2 - \frac{1}{3}\hat{\mathbf{S}}^2 \end{pmatrix}\end{aligned} \tag{3.1}$$

The quadrupolar operators $\hat{Q}_{\alpha\beta}$ constitute the lowest order observables that carry information beyond the spin vector $\hat{\mathbf{S}}$. Note that, the operators $\hat{S}_i$ are hermitian and satisfy $\hat{\mathbf{S}}^2 = \hat{S}_x^2 + \hat{S}_y^2 + \hat{S}_z^2$, thus only five of the total nine entries of $\hat{Q}_{\alpha\beta}$ are linearly independent. Furthermore, the scalar contribution $\hat{\mathbf{S}}^2$ is proportional to the identity $\mathbb{I}$ and thus trivial once we fix the spin-1 representation.

With the identity, the three dipolar operators and the five linearly independent quadrupolar operators we build a basis of nine hermitian matrices. To understand the information encoded in the 8 nontrivial operators, suppose to repeatedly measure the spin in the arbitrary direction $\mathbf{n}$ on copies of the same spin-N wavefunction $|\psi\rangle$. The average of the spin measurements $\langle\psi|\,\mathbf{n}\cdot\hat{\mathbf{S}}\,|\psi\rangle$ depends, as expected, on the three dipolar operators:

$$\langle\psi|\,\mathbf{n}\cdot\hat{\mathbf{S}}\,|\psi\rangle = \mathbf{n}\cdot\langle\psi|\,\hat{\mathbf{S}}\,|\psi\rangle\,. \tag{3.2}$$

From the set of repeated measurements, we compute their variance:

$$\begin{aligned}\left\langle\left(\hat{\mathbf{n}}\cdot\hat{\mathbf{S}} - \langle\hat{\mathbf{n}}\cdot\hat{\mathbf{S}}\rangle\right)^2\right\rangle &= \left\langle n_i\left(\hat{S}_i - \langle\hat{S}_i\rangle\right) n_j\left(\hat{S}_j - \langle\hat{S}_j\rangle\right)\right\rangle \\ &= n_i\left\langle\left(\hat{S}_i - \langle\hat{S}_i\rangle\right)\left(\hat{S}_j - \langle\hat{S}_j\rangle\right)\right\rangle n_j \\ &= \hat{\mathbf{n}}^T C\hat{\mathbf{n}}\end{aligned} \tag{3.3}$$

where we introduced the covariance matrix, defined as:

$$\begin{aligned}C_{\alpha\beta} &= \left\langle\left(\hat{S}_\alpha - \langle\hat{S}_\alpha\rangle\right)\left(\hat{S}_\beta - \langle\hat{S}_\beta\rangle\right)\right\rangle \\ &= \langle\hat{Q}_{\alpha\beta}\rangle - \langle S_\alpha\rangle\langle S_\beta\rangle + \frac{1}{3}S(S+1)\delta_{\alpha\beta}\end{aligned} \tag{3.4}$$

and S is the spin length, fixed by the representation in use and equal to N for a single spin-N. Indeed, quadrupolar operators are relevant to the computation of second moments of the distribution of spin measurements. Equation (3.4) also clarifies the contribution of the quadrupolar tensor $\hat{Q}$ in spin measurements. The expectation value of the spin vector $\hat{\mathbf{S}} = (\hat{S}_x, \hat{S}_y, \hat{S}_z)^T$ determines the mean

outcome of measurements along the Cartesian axes, while the covariance matrix C encodes their fluctuations and depends both on $\hat{\mathbf{S}}$ and $\hat{Q}_{\alpha\beta}$. In addition, the 3×3 covariance matrix C is hermitian and thus admits an eigenvector decomposition with real eigenvalues. By looking at its eigenvalues λ_j and $\mathbb{R}^3$ eigenvectors $\hat{\lambda}_j$ we identify the directions in spin space along which the fluctuations are highest or lowest or intermediate.

Similarly, higher order spin operators can be associated with higher moments of the distribution of measurements.

Our basis is so far composed of 9 operators: the identity, the dipolar spin operators $\hat{S}_\alpha$ and the quadrupolar nematic tensor $\hat{Q}_{\alpha\beta}$. It's possible to expand the basis by selecting all spin operators that transform as rank-N operators under rotations with $N > 2$. As discussed at the beginning of this chapter, this procedure does not necessarily lead to linearly independent observables for all spin representations. For example, the vector space of hermitian operators acting on a single spin-$1/2$ state has dimension $(2N+1)^2 = 4$, which is also the dimension of the vector space of 2×2 matrices that represent said operators. Indeed, in the spin-$1/2$ representation the spin operators are mapped to the 2×2 Pauli matrices $\hat{\sigma}_i$ which satisfy $\hat{\sigma}_i^2 = \mathbb{I}$, $\{\hat{\sigma}_i, \hat{\sigma}_j\} = \delta_{ij}$. As a consequence, all higher-order spin operators $\hat{S}_i^m$ for $m \geq 2$ are either trivial, $\mathbb{I}$, or equal to their first power $\hat{S}_i$. Furthermore, all possible spin-$1/2$ operators are linear combinations of the three Pauli matrices and the identity as these four operators are enough to fill the vector space of 2×2 hermitian matrices.

Regarding the spin-1 Hilbert space, its vector space of hermitian matrices has dimension $(2N+1)^2 = 9$. Thus, all the information needed to describe a spin-1 pure state is contained in its length $\langle\hat{\mathbf{S}}^2\rangle$, in the three elements of its dipolar vector $\langle\hat{\mathbf{S}}\rangle$ and in the five elements of its quadrupolar tensor $\langle\hat{Q}\rangle$.

Having introduced the quadrupolar tensor of fluctuations $\hat{Q}$ of Eq. (3.1), we investigate its role in the description of spin-$1/2$ and spin-1 states.

3.1.a Spin-$1/2$ fluctuations

A single spin-$1/2$ system is described in the basis composed by the eigenstates $|\uparrow\rangle$ and $|\downarrow\rangle$ of $\hat{S}_z$ with eigenvalues $\pm 1/2$ respectively. In this basis, the operators $\hat{S}_x, \hat{S}_y, \hat{S}_z$ coincide with the 2×2 Pauli matrices:

$$\hat{S}_\alpha = \frac{1}{2}\hat{\sigma}_\alpha, \tag{3.5}$$

with properties:

$$[\hat{\sigma}_\alpha, \hat{\sigma}_\beta] = 2i\epsilon_{\alpha\beta\gamma}\hat{\sigma}_\gamma, \tag{3.6}$$

and:

$$\{\hat{\sigma}_\alpha, \hat{\sigma}_\beta\} = 2\delta_{\alpha\beta}. \tag{3.7}$$

While Eq. (3.6) is a direct consequence of the structure of the Lie algebra $\mathfrak{su}(2)$, Eq. (3.7) is a unique property of the Pauli matrices and thus of the fundamental representation spin-$1/2$ of $\mathfrak{su}(2)$.

Eq. (3.7) highlights once again that for a single spin-$1/2$, quadratic or higher order spin operators do not introduce independent degrees of freedom beyond linear spin terms, as introduced at the beginning of this chapter. Indeed, we decompose the quadratic product of two spin-$1/2$ operators into the sum of their commutators and anticommutators to get:

$$\begin{aligned}\hat{S}_\alpha \hat{S}_\beta &= \frac{1}{2}\left(\left[\hat{S}_\alpha, \hat{S}_\beta\right] + \left\{\hat{S}_\alpha, \hat{S}_\beta\right\}\right) \\ &= \frac{1}{2}\left(i\epsilon_{\alpha\beta\gamma}\hat{\sigma}_\gamma + \delta_{\alpha\beta}\right).\end{aligned} \tag{3.8}$$

Therefore, for a single spin-$1/2$ Hilbert space, any quadratic combination can be remapped to a single dipolar spin operator.

As a direct consequence of Eq. (3.7), the quadrupolar tensor $\hat{Q}$ is exactly equal to zero for spin-$1/2$ states. The matrix C then depends only on the expectation values of the dipolar operators $\langle \hat{S}_j \rangle$, as of Eq. (3.4). To study these expectation values, we take a generic point on the surface of the Bloch sphere, characterized by the polar angles (θ, ϕ). These angles characterize the pure state $|\psi\rangle = \cos(\theta/2)\,|\uparrow\rangle + e^{i\phi}\sin(\theta/2)\,|\uparrow\rangle$.

Without loss of generality, suppose we rotate our system such that $|\psi\rangle = |\uparrow\rangle$. The off-diagonal elements of C are zero as of Eq. (3.4) because $\langle \hat{S}_x \rangle = \langle \hat{S}_y \rangle = 0$. The only nonzero terms are on the diagonal, where $\langle \hat{\mathbf{S}}^2 \rangle = 3/4$ and $\langle \hat{S}_z \rangle^2 = 1/4$:

$$C = \begin{pmatrix} \frac{1}{4} & 0 & 0 \\ 0 & \frac{1}{4} & 0 \\ 0 & 0 & 0 \end{pmatrix} \tag{3.9}$$

Since we rotated our spin state the matrix C is diagonal, with two equal eigenvalues corresponding to the plane perpendicular to $\hat{z}$, and a third eigenvalue, 0, in the direction of $\hat{z}$. Since the elements on the diagonal correspond to the variance of the spin in the relative direction, we conclude that there are no fluctuations along the direction of the state $|\psi\rangle$, while the fluctuations are isotropic in the plane perpendicular to it. This is a well known result for spin-$1/2$ states.

The key information we may extract from this example is that a pure spin-$1/2$ state is characterized by its direction $\hat{\mathbf{n}}$ in spin space: it has a zero valued quadrupolar operator and an isotropic plane of fluctuations perpendicular to $\hat{\mathbf{n}}$.

3.1.b Breaking axial symmetry with spin-1 states

Quadratic operators applied on spin-1 states are nontrivial, differently from states of single spin-$1/2$. Higher order operators $\hat{S}_i^{n\geq 3}$, instead, will not introduce linearly independent degrees of freedom, as discussed at the beginning of this chapter. A single spin-1 pure state is completely characterized by the dipolar operators $\hat{S}_j$, the quadrupolar tensor $\hat{Q}$ and the spin length $\hat{\mathbf{S}}^2$.

To display the possibilities that single spin-1 states offer, we look at the following specific state:

$$|\psi\rangle = -\frac{1}{2\sqrt{3}}|1\rangle + \sqrt{\frac{2}{3}}|0\rangle - \frac{1}{2\sqrt{3}}|-1\rangle\,, \tag{3.10}$$

which gives the following matrices for the quadrupolar tensor:

$$\langle\hat{Q}\rangle = \begin{pmatrix} \frac{1}{3} & 0 & 0 \\ 0 & 0 & 0 \\ 0 & 0 & -\frac{1}{3} \end{pmatrix}, \tag{3.11}$$

and covariance matrix:

$$C = \begin{pmatrix} \frac{1}{9} & 0 & 0 \\ 0 & \frac{2}{3} & 0 \\ 0 & 0 & \frac{1}{3} \end{pmatrix}, \tag{3.12}$$

while the spin vector is given by:

$$\langle\hat{\mathbf{S}}\rangle = \left(\frac{2\sqrt{2}}{3}, 0, 0\right)^T. \tag{3.13}$$

From Eq. (3.12) we see that fluctuations are anisotropic, differently from the result of Eq. (3.9). Since the isotropy of the latter was independent of the chosen spin-$1/2$ state, anisotropic states are unique of higher spin-N representations $N \geq 1$.

3.1.c Time reversal symmetry and quadrupolar states

We have shown that spin-1 states offer a richer physics than spin-$1/2$ states. To further exemplify this statement, we now look at the behavior of spin states under the action of time reversal symmetry.

Time reversal is defined as an antiunitary transformation T which, in spin space, flips the components of the spin vector: $T\hat{\mathbf{S}}T^{-1} = -\hat{\mathbf{S}}$. Any spin state $|\psi\rangle$ which shows a nonzero spin vector $\langle\hat{\mathbf{S}}\rangle \neq 0$ is not an eigenvector of time reversal.

Suppose $|\psi'\rangle = T|\psi\rangle$, under the action of the operator T the direction of the spin arrow measured on such state is flipped:

$$\begin{aligned}\langle\psi|\,\hat{\mathbf{S}}\,|\psi\rangle &= \langle\psi'|\,T\hat{\mathbf{S}}T^{-1}\,|\psi'\rangle \\ &= \langle\psi'|\,-\hat{\mathbf{S}}\,|\psi'\rangle \\ &= -\langle\psi'|\,\hat{\mathbf{S}}\,|\psi'\rangle\,,\end{aligned} \tag{3.14}$$

and thus all quantum states with nonzero spin length are not preserved by time reversal. Since we know that all spin-$1/2$ states are characterized by the direction of their spin vector $\hat{\mathbf{n}}$, under the action of the operator T such states are flipped to $-\hat{\mathbf{n}}$.

For spin-1 wavefunctions, the spin length is not necessarily maximal, as for the $\hat{S}_z$ eigenstate $|\psi\rangle = |0\rangle$:

$$\langle\hat{S}_x\rangle = \langle\hat{S}_y\rangle = \langle\hat{S}_z\rangle = 0, \tag{3.15}$$

which displays a nonzero nematic tensor:

$$\langle Q\rangle = \begin{pmatrix} \frac{1}{3} & 0 & 0 \\ 0 & \frac{1}{3} & 0 \\ 0 & 0 & 0 \end{pmatrix}, \tag{3.16}$$

and an isotropic variance on the plane perpendicular to $\hat{z}$ with zero fluctuations along the z axis:

$$C = \begin{pmatrix} 1 & 0 & 0 \\ 0 & 1 & 0 \\ 0 & 0 & 0 \end{pmatrix}. \tag{3.17}$$

The distribution of its fluctuations is symmetric in the xy plane, perpendicular to z, but unlike the spin-$1/2$ state used to get Eq. (3.9), there is no spin vector. Since the state $|0\rangle$ is missing the "directionality" that the spin vector gives, it's left untouched by the time reversal operator T.

We studied states as the one in Eq. (3.10) or $|0\rangle$ which show different properties: from the length of the measured spin vector $\langle\hat{\mathbf{S}}\rangle$ to their transformation under time reversal. Given this different physical behaviors, we characterize all the possible pure spin-1 states:

- Purely coherent states, which have maximal spin length $\langle\hat{\mathbf{S}}\rangle^2 = 1$. Examples are the $\hat{S}_z$ eigenvectors $|\pm 1\rangle$. These states behave like spin-$1/2$ states and show isotropic fluctuations along the plane perpendicular to the vector $\langle\hat{\mathbf{S}}\rangle$.
- Purely quadrupolar states, with vanishing spin vector $\langle\hat{\mathbf{S}}\rangle = 0$. An example

is the $\hat{S}_z$ eigenvector $|0\rangle$. These states are time reversal invariant up to a global phase and show isotropic fluctuations on a plane in spin space.

- Mixtures of the two states, as the state introduced in Eq. (3.10). These states have a spin vector of intermediate length $0 < \langle\hat{\mathbf{S}}\rangle^2 < 1$ and show anisotropic fluctuations as shown in Eq. (3.12). These states break both time reversal symmetry and rotational symmetry with respect to the spin vector.

Having presented the different physical states that can be found in the spin-1 representation, in the following chapter we introduce a systematic study of such states.

3.2 Cartesian representation of spin-1 states

The most generic $S = 1$ wavefunction can be written as:

$$\begin{aligned} |\psi\rangle &= (u_x + iv_x)\,|x\rangle + (u_y + iv_y)\,|y\rangle + (u_z + iv_z)\,|z\rangle \\ &= (\mathbf{u} + i\mathbf{v}) \cdot (|x\rangle, |y\rangle, |z\rangle)\,, \end{aligned} \tag{3.18}$$

where $\mathbf{u}, \mathbf{v}$ are real vectors and $(|x\rangle, |y\rangle, |z\rangle)$ define a basis of time reversal invariant states built from $\hat{S}_z$ eigenstates:

$$\begin{aligned} |x\rangle &= \frac{i}{\sqrt{2}}\,(|1\rangle - |-1\rangle)\,, \\ |y\rangle &= \frac{1}{\sqrt{2}}\,(|1\rangle + |-1\rangle)\,, \\ |z\rangle &= -i\,|0\rangle\,, \end{aligned} \tag{3.19}$$

which also obey:

$$\hat{S}_i\,|j\rangle = i\epsilon_{ijk}\,|k\rangle\,, \tag{3.20}$$

such that $\hat{S}_i\,|i\rangle = 0$. With this choice, the state $|i\rangle$ is the eigenvector of zero eigenvalue of the spin $\hat{S}_i$ along the direction $i \in \{x, y, z\}$. These states are pure quadrupolar states with isotropic fluctuations along the plane perpendicular to the spin that they are named from.

We can write the normalization condition as:

$$u^2 + v^2 = 1, \tag{3.21}$$

while the global phase of the wavefunction is a redundancy which affects the choice of $\mathbf{u}, \mathbf{v}$ vectors, which are not gauge-invariant. To see this, we send

$|\psi\rangle \to e^{i\gamma}|\psi\rangle$ to get:

$$\begin{aligned} \mathbf{u}' &= \mathbf{u}\cos\gamma - \mathbf{v}\sin\gamma \\ \mathbf{v}' &= \mathbf{u}\sin\gamma + \mathbf{v}\cos\gamma. \end{aligned} \tag{3.22}$$

This redundancy leads to physically equivalent states described by different pairs of vectors. As expected, the transformation in Eq. (3.22) preserves the normalization of Eq. (3.21), since it's just a rotation of $|\psi\rangle$ of a complex phase.

By computing the scalar product of the pair $\mathbf{u}', \mathbf{v}'$ we find:

$$\mathbf{u}' \cdot \mathbf{v}' = \left(u^2 - v^2\right)\frac{1}{2}\sin 2\gamma + \mathbf{u}\cdot\mathbf{v}\cos 2\gamma, \tag{3.23}$$

so a gauge-fixing condition is given by the constraint [37]:

$$\mathbf{u}' \cdot \mathbf{v}' = 0. \tag{3.24}$$

From Eq. (3.23) we find that the needed angle γ satisfies:

$$\tan 2\gamma = \frac{2\mathbf{u}\cdot\mathbf{v}}{v^2 - u^2}, \tag{3.25}$$

where $\gamma \in]-\pi/4, \pi/4[$.

Notice that even if the initial pair is orthogonal $\mathbf{u}\cdot\mathbf{v} = 0$, we must fix γ in Eq. (3.23) to one of the values $\{\pm\pi/2, \pm\pi\}$, except for purely coherent states where $u^2 = v^2$. Indeed, the tangent in Eq. (3.25) has a marginal redundancy for $\tan 2\gamma = 0$ given by those four angles, which map the original vectors $\mathbf{u}, \mathbf{v}$ to, respectively, $(-\mathbf{v}, \mathbf{u})$, $(\mathbf{v}, -\mathbf{u})$ and $(-\mathbf{u}, -\mathbf{v})$.

The complete gauge-fixing procedure for a given pure spin-1 state is the following:

- find the two vectors $\mathbf{u}, \mathbf{v}$ from its decomposition in the time-reversal invariant basis of Eq. (3.19).
- Compute the angle γ from Eq. (3.25) and rotate the vectors $\mathbf{u}, \mathbf{v}$ to the pair $\mathbf{u}', \mathbf{v}'$ of Eq. (3.22).
- Switch $\mathbf{u}', \mathbf{v}'$ such that they are ordered $u' > v'$, and take their entries to be positive.

This gauge-fixing procedure might seem contrived, but allows for a simple computation of the expected values of the spin vector, the spin length and the action of the spin operator on the obtained state $|\psi\rangle$. After fixing the gauge, with

$|\psi\rangle$ of orthogonal vectors $\mathbf{u}, \mathbf{v}$ satisfying $u > v$, those expectation values read:

$$\langle\psi|\,\hat{\mathbf{S}}\,|\psi\rangle = 2\mathbf{u}\times\mathbf{v}, \tag{3.26}$$

$$\langle\psi|\,\hat{\mathbf{S}}\,|\psi\rangle^2 = 4u^2v^2, \tag{3.27}$$

$$\hat{\mathbf{S}}\,|\psi\rangle = i\,(\mathbf{u}+i\mathbf{v})\times(|x\rangle\,,|y\rangle\,,|z\rangle)^T\,. \tag{3.28}$$

From Eq. (3.27) it's clear that a generic state is purely quadrupolar, $\langle\hat{\mathbf{S}}\rangle^2 = 0$, if $\mathbf{u}=0\vee\mathbf{v}=0$ and purely coherent, $\langle\hat{\mathbf{S}}\rangle^2 = 1$, if $u=v=1/\sqrt{2}$.

In the following we assume that the conditions Eq. (3.24) and Eq. (3.21) are satisfied if not stated otherwise.

If the state is not purely coherent we call the longest vector $\mathbf{u}$ the director, which from Eq. (3.26) satisfies:

$$\begin{aligned}\mathbf{u}\cdot\hat{\mathbf{S}}\,|\psi\rangle &= i\mathbf{u}\cdot(\mathbf{u}+i\mathbf{v})\times(|x\rangle\,,|y\rangle\,,|z\rangle)^T\\ &= (\mathbf{v}\times\mathbf{u})\cdot(|x\rangle\,,|y\rangle\,,|z\rangle)^T\\ &= v_iu_j\epsilon_{ijk}\,|k\rangle\,,\end{aligned} \tag{3.29}$$

where ϵ_{ijk} is the Levi-Civita pseudotensor.

From Eq. (3.29) it's clear that a purely quadrupolar state ($v=0$) is an eigenstate of zero eigenvalue for the spin in the direction of $\mathbf{u}$ and its fluctuations along $\mathbf{u}$ are also zero. The director $\mathbf{u}$ is perpendicular to the plane of isotropic fluctuation like coherent states, but unlike them it has no orientation: it's an axial vector with no preferred direction given by $\langle\hat{\mathbf{S}}\rangle$.

We are now able to give a general description of spin-1 states:

- Fully quadrupolar states have a vanishing spin vector $\langle\hat{\mathbf{S}}\rangle = 0$ and are defined by their director up to an irrelevant phase: $|\psi\rangle = |\mathbf{u}\rangle$.
- Fully coherent states have a spin vector of maximal length oriented along $\hat{\mathbf{n}}$, $\left\langle\left(\hat{\mathbf{n}}\cdot\hat{\mathbf{S}}\right)\right\rangle^2 = 1$, and are characterized by $\hat{\mathbf{n}}$ up to an irrelevant phase: $|\psi\rangle = |\mathbf{n}\rangle$.
- States that are partially quadrupolar or coherent are defined by the pair of vectors $\mathbf{u}, \mathbf{v}$ up to an irrelevant phase.

As a final note, for a generic single spin-1 wavefunction its coherent or quadrupolar characters are competing quantities. From Eq. (3.21) and Eq. (3.27) we derive the following relation:

$$u^2 = \frac{1}{2}\left[1+\sqrt{1-\langle\hat{\mathbf{S}}\rangle^2}\right], \tag{3.30}$$

so a generic state is purely quadrupolar or purely coherent or a partial mixture of the two, but the first two are mutually exclusive.

Finally, for a generic state $|\mathbf{u}, \mathbf{v}\rangle$ of vectors $\mathbf{u} + i\mathbf{v}$ we report the expectation values of the quadrupolar operators $\hat{Q}_{\alpha\beta}$. The operators on the diagonal $\hat{Q}_{\alpha\alpha}$, after removing the constant term proportional to $S(S+1) = 2$, read:

$$\begin{aligned} \langle \hat{Q}_{\alpha\alpha} \rangle + 2/3 &= \sum_{\beta \neq \alpha} |u_\beta + i v_\beta|^2 \\ &= 1 - |u_\alpha + i v_\alpha|^2 , \end{aligned} \tag{3.31}$$

while the off-diagonal operators $\hat{Q}_{\alpha\beta}$ for $\beta \neq \alpha$ are:

$$\langle \hat{Q}_{\alpha\beta} \rangle = -2 \left(u_\alpha u_\beta + v_\alpha v_\beta \right) . \tag{3.32}$$

Having presented the opportunities that higher spin representations offer with respect to spin-$1/2$ states and after characterizing the possible spin-1 wavefunctions, in the next chapter we propose a model of interacting bosons and spin-1 degrees of freedom which features quadrupolar states in its ground state.

4 Topology from instability in spin-1 chains

In chapter 2 we introduced a one dimensional model of interacting bosons and spins. The model, as shown in Appendix A, always shows a dimerization of the bosonic hoppings in its ground state, for a specific choice of its parameters. This dimerization is induced by the boson-spin interaction and it ignores the nature of the spins. In chapter 3 we laid the fundamental theoretical ideas needed to describe a single spin-1 state. We found that, differently from spin-$1/2$, a single spin-1 state can be an eigenvector of time-reversal. Moreover, quadratic operators can act non-trivially within the local spin-1 Hilbert space.

For this reason, when extending the model of Eq. (2.11) from the spin-$1/2$ to the spin-1 degrees of freedom, several generalizations are possible. The aim of this thesis is to develop a Hamiltonian of interacting bosons and spin-1 qudits whose ground state features both a Peierls transition and quadrupolar spin states, a phenomenon unique of higher-length spin-N states, $N > 1/2$.

An advantage of quantum simulation techniques is the ability to realize ad-hoc, experimentally-viable couplings that go beyond the ones of Eq. (2.11). As a natural consequence of this possibility, we detach the spin-1 model from the couplings and from the Peierls mechanism behind Eq. (2.1).

The following chapter and the aim of this thesis is to bridge the ideas present in previous two chapters. We propose a modification of the Hamiltonian in Eq. (2.11) by implementing spin-1 quadrupolar operators. Spin-1 sites lead to a widely different morphology of the phase space, which features both Néel ordered regions and uniform regions of time reversal invariant spin-1 $|0\rangle$ states. Going into detail, the proposed model features a parameter space with four different regions corresponding to three different symmetry sectors in its ground state. Said sectors are characterized by the spin-1 wavefunction of the ground state, which is found in a state with ferroquadrupolar order, with alternating

Néel ordered nonquadrupolar states and lastly in an intertwined phase of alternating $|0\rangle$ and almost-coherent states with $u^2 \approx 1/2$.

In order to understand how and why such morphology emerges, we first give a brief overview on how dipolar and quadrupolar operators interact, then propose an analytical ansatz based on the Born-Oppenheimer approach introduced in chapter 2 and finally present a numerical study using exact diagonalization methods for a finite-size chain.

4.1 Quadrupolar states interacting with dipolar fields

In the following section we introduce an on-site spin-1 operator $\hat{O}$ which, suitably combined with the Hamiltonian of Eq. (2.12), is able to introduce $|0\rangle$ states in the ground state of the bosonic and spin-1 chain. Before dealing with the nature and behavior of the operator $\hat{O}$, we report some considerations on the shape of the Hamiltonian in Eq. (2.11) which led us to the introduction of this operator.

To move from the spin-$1/2$ Hamiltonian of Eq. (2.11) to the spin-1 formalism, many possible choices were considered.

One possibility is to map the spin-$1/2$ operators that emerged from the Holstein-Primakoff transformation of Eq. (2.10) and promote them to spin-1 operators: $\hat{\sigma}_z \to \hat{S}_z$, $\hat{\sigma}_x \to \hat{S}_x$. The Hamiltonian reads:

$$\hat{H} = -\sum_i \left[t + \alpha \hat{S}^z_{l(i)}\right] \left(\hat{c}^\dagger_i \hat{c}_{i+1} + \hat{c}^\dagger_{i+1} \hat{c}_i\right) + \frac{\Delta}{2} \sum_i \hat{S}^z_{l(i)} + \beta \sum_i \hat{S}^x_{l(i)} \tag{4.1}$$

As proven in Appendix A, for $\beta = 0$ the spin Hamiltonian of Eq. (2.11) is actually independent on the spin length, since the ground state is found in a product state of bosons and spin-1 $\hat{S}_z$ eigenstates. The adiabatic limit $\beta = 0$ thus recovers the same behavior and regions of the parameter space of the spin-$1/2$ case.

Different behaviors are expected for the two models for $\beta \neq 0$, since the action of the operator $\hat{\sigma}_x$ on the spin-$1/2$ eigenstates $|\uparrow\rangle, |\downarrow\rangle$ is fundamentally different from the one of the spin-1 operator $\hat{S}_x$ on the coherent states $|+1\rangle, |-1\rangle$. The former operator inverts the two spin-$1/2$ states, $\hat{\sigma}_x |\uparrow, \downarrow\rangle = |\downarrow, \uparrow\rangle$ while the latter sends both coherent states to the quadrupolar state $|0\rangle$: $\hat{S}_x |\pm 1\rangle = |0\rangle / \sqrt{2}$.

We expect that for large enough values of β the ground state's spin wavefunction features a superposition of quantum states, some of which are of quadrupolar nature $|0\rangle$. In fact, treating perturbatively the action of a singular on-site operator $\beta \hat{S}^x_{l(0)}$ over the symmetry-broken Néel state with alternating spin-1 wavefunctions, denoted $|+1, -1\rangle$, we find that the ground state acquires terms

hosting $|0\rangle$ spin-1 states:

$$|\Psi_{\text{GS}}\rangle_{\beta \ll t} = |+1,-1\rangle + \frac{\beta}{\Delta E}|0,-1\rangle \tag{4.2}$$

where $\Delta E = \langle 0,-1|\,\hat{H}\,|0,-1\rangle - \langle +1,-1|\,\hat{H}\,|+1,-1\rangle$.

The problem of the Hamiltonian of Eq. (4.1) is that the presence of $|0\rangle$ spin-1 states is strictly dependent on the value of β, which also increases quantum correlations and reduces the efficacy of a mean-field description, similarly to the behavior presented in Figure 2.10.

As we increase the value of β to increase the prevalence of $|0\rangle$ states, we also decrease the efficacy of the mean-field Born-Oppenheimer ansatz which ensures the presence of a Peierls transition.

Building from the result of Appendix A another possible approach is to substitute the $\hat{\sigma}_z$ operators of Eq. (2.11) with one or a combination of the spin-1 quadrupolar operators $\hat{Q}_1$ introduced in chapter 3 and the $\hat{s}_x$ operator with another operator $\hat{Q}_2$ which does not commute with $\hat{Q}_1$.

The Born-Oppenheimer ansatz for $\beta = 0$ is independent on the nature of the spin sites and for the appearance of Néel ordered regions requires only that the chosen local quadrupolar operator $\hat{Q}_1$ with eigenvalues $\{\, q_i \,\}$ has opposite-valued minimum and maximum eigenvalues $\min\{\, q_i \,\} = -\max\{\, q_i \,\}$. The Néel ordered region then features separable ground states identical to the ones presented in chapter 2 where the spin-1/2 states $|\uparrow\rangle, |\downarrow\rangle$ are substituted by the eigenvectors $|q_{\text{max}}\rangle, |q_{\text{min}}\rangle$ of $\hat{Q}_1$ with extremal eigenvalues.

Once again, different behaviors arise as we introduce quantum fluctuations for $\beta \neq 0$ and the physical properties of the ground state depend on the choice of operators $\hat{Q}_1, \hat{Q}_2$.

In order to feature an intertwined phase of alternating purely quadrupolar and purely coherent states in the ground state of the system we propose a model which goes beyond the Born-Oppenheimer paradigm introduced in chapter 2 and developed in Appendix A. In the following section we introduce the chosen spin-1 operator which will regulate the bosonic and spin-1 interaction, then in the next section we present the complete bosonic and spin-1 Hamiltonian.

Suppose we prepare a single spin-1 system as a quadrupolar state with director along $\hat{e}_z$. Consider, for example, the Hamiltonian $H = -\kappa\left(\hat{S}_x^2 - \hat{S}_z^2\right)$, which is diagonal in the $|x\rangle, |y\rangle, |z\rangle$ basis. Its eigenvalues are, in order, $+1, 0 - 1$ for $\kappa > 0$.

We introduce a dipolar perturbation along the generic direction $\mathbf{h}$:

$$H = -\kappa\left(\hat{S}_x^2 - \hat{S}_z^2\right) + \mathbf{h}\cdot\hat{\mathbf{S}} \tag{4.3}$$

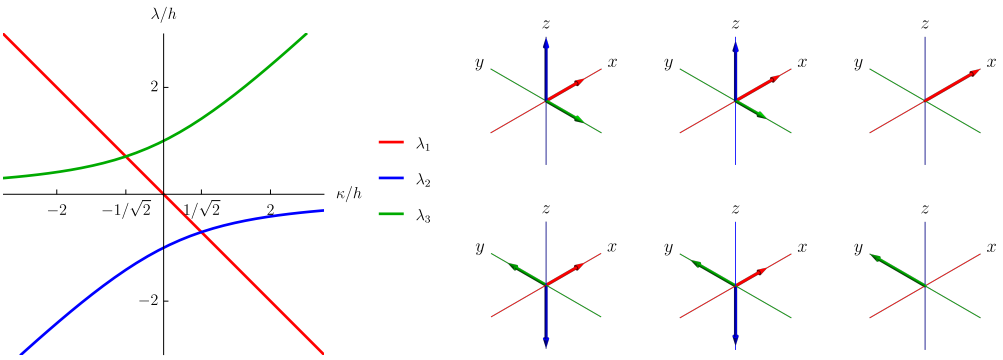

Figure 4.1: Left: Eigenvalues of the perturbed quadrupolar Hamiltonian as a function of the ratio κ/h. Right: $\mathbf{u}$ (green) $\mathbf{v}$ (red) and $\langle \mathbf{S} \rangle$ (blue) as κ/h changes for $|\psi_2\rangle$ (top) and for $|\psi_3\rangle$ (bottom). From left to right, the values of κ/h are 0, the critical value $1/\sqrt{2}$ and infinity.

The effect of a dipolar perturbation depends on the angle in between the dipolar vector $\mathbf{h}$ and the director of the unperturbed ground state [37]. To lay out the theory used in the following sections, we focus only on dipolar perturbations which are parallel to the director of the ground state $|z\rangle$: $h\hat{S}_z$.

We write the total Hamiltonian of Eq. (4.3) for $\mathbf{h} \cdot \hat{\mathbf{S}} = h\hat{S}_z$:

$$H = -\kappa \left(\hat{S}_x^2 - \hat{S}_z^2 \right) + h\hat{S}_z. \tag{4.4}$$

The eigenvalues of this Hamiltonian are:

$$\lambda_1 = -\kappa \tag{4.5}$$

$$\lambda_2 = \frac{1}{2}\left(\kappa - \sqrt{\kappa^2 + 4h^2} \right) \tag{4.6}$$

$$\lambda_3 = \frac{1}{2}\left(\kappa + \sqrt{\kappa^2 + 4h^2} \right) \tag{4.7}$$

with respective eigenvectors:

$$|\psi_1\rangle = |z\rangle \tag{4.8}$$

$$|\psi_2\rangle = \sin\theta_- |y\rangle + i\cos\theta_- |x\rangle \tag{4.9}$$

$$|\psi_3\rangle = \sin\theta_+ |y\rangle + i\cos\theta_+ |x\rangle \tag{4.10}$$

where $\tan(\theta_\pm - \pi/4) = -2h/\kappa \pm \sqrt{1 + (2h/\kappa)^2}$. Notice that there are two level crossings: one between the eigenstates $|\psi_1\rangle$ and $|\psi_2\rangle$ for $\kappa = h/\sqrt{2}$ and one for $|\psi_1\rangle$ and $|\psi_3\rangle$ for $k = -h/\sqrt{2}$.

While $|z\rangle$ is an eigenvector of both operators of (4.4), the eigenstates $|\psi_2\rangle$, $|\psi_3\rangle$

depend on the ratio κ/h. Using the $\mathbf{u}, \mathbf{v}$ formalism introduced in section 3.2, the eigenvectors $|\psi_2\rangle$ and $|\psi_3\rangle$ correspond to the pairs $\mathbf{u} = \sin\theta_{\mp}\mathbf{e}_y$ and $\mathbf{v} = \cos\theta_{\mp}\mathbf{e}_x$ respectively, which satisfy the constraints of Eq. (3.21) and (3.24). It is immediate to show that these two eigenstates continuously develop a nonzero dipolar moment for $h \neq 0$. Through Eq. (3.26) indeed we find:

$$\langle\psi_2|\,\mathbf{S}\,|\psi_2\rangle = -\sin(2\theta_-)\,\mathbf{e}_z \tag{4.11}$$

$$\langle\psi_3|\,\mathbf{S}\,|\psi_3\rangle = -\sin(2\theta_+)\,\mathbf{e}_z. \tag{4.12}$$

The wavefunction of the ground state is dependent on the ratio κ/h and evolves abruptly from the state $|\psi_2\rangle$ to the quadrupolar state $|z\rangle$ when $\kappa/h > 1/\sqrt{2}$. At such level crossing, $|\psi_2\rangle$ has a nonzero spin moment equal to $\langle\mathbf{S}\rangle = -2\sqrt{2}/3\mathbf{e}_z \approx -0.94\mathbf{e}_z$. The transition involves a purely quadrupolar, time reversal invariant state $|z\rangle$ and a state which is almost completely coherent $|\psi_2\rangle$.

The quadrupolar operator of (4.3) was chosen because of the peculiar properties of its eigenstates $|\psi_1\rangle, |\psi_2\rangle, |\psi_3\rangle$. Its lowest energy eigenstate for $\kappa/h > 1/\sqrt{2}$ is $|\psi_1\rangle = |z\rangle$, which is also an eigenstate of the dipolar perturbation $h\hat{S}_z$. Thus, the state $|z\rangle$ is an eigenstate of the full Hamiltonian of (4.3), although its energy may change with h. The two eigenstates $|\psi_2\rangle, |\psi_3\rangle$ are the quadrupoles $|x\rangle, |y\rangle$ for $\kappa/h \to +\infty$, but transform continuously under $\hat{S}_z$ as we lower the ratio κ/h and evolve towards the coherent states $|+1\rangle, |-1\rangle$. Their dipolar expectation value is zero when $h = 0$, but grows continuously to ± 1 as we decrease the ratio κ/h. We take advantage of these behaviors by connecting them to the bosonic-spin Hamiltonian discussed in chapter 2.

In the following section, we introduce a model where the bosonic chain interacts with the spin-1 chain inducing a Néel ordering on the spin side and an alternating bond order on the bosonic side. The ratio κ/h acts as a tunable degree of freedom, which changes the nature of the spin wavefunction because it changes the lowest energy eigenstates of Eq. (4.4). We find a transition from a dimerized bosonic phase interacting with states with partially developed spins to one interacting with purely quadrupolar states.

4.2 Intertwined quadrupolar-nonquadrupolar phases in a symmetry-breaking topological insulator

The model that we propose is a variation of the Hamiltonian in equation (2.12):

$$\hat{H} = -\sum_i \left[t + \alpha\hat{O}_{l(i)}\right]\hat{B}_{l(i)} + \frac{\Delta}{2}\sum_i \hat{S}^z_{l(i)} + \frac{U}{2}\sum_i \hat{n}_i\left(\hat{n}_i - 1\right) \tag{4.13}$$

where the operator $\hat{B}_{l(i)}$ is the bosonic hopping operator in between sites $i, i+1$ introduced in Eq. (2.6), while $\hat{O}_{l(i)}$ is the operator introduced in Eq. (4.4) for $h = 1$:

$$\hat{O}_{l(i)} = -\kappa \left[\left(\hat{S}^x_{l(i)} \right)^2 - \left(\hat{S}^z_{l(i)} \right)^2 \right] + \hat{S}^z_{l(i)}. \tag{4.14}$$

As discussed in the previous chapter, the operator $\hat{O}_{l(i)}$ acts as the operator $\hat{\sigma}_z$ of (2.11) when $\kappa \ll 1$.

From the Hamiltonian in Eq. (4.13) we understand that the local spin-1 space is symmetric under the transformation $\hat{S}^x_l \to -\hat{S}^x_l$: a rotation of π around the z axis. The corresponding spin-1 local operator is $\exp\left(-i\pi \hat{S}^z_l\right)$, which has a nondegenerate eigenvector $|0\rangle_l$ and two degenerate eigenvectors $|+1\rangle_l, |-1\rangle_l$. Since the local rotation operator commutes with the global Hamiltonian, $\left[\hat{H}, \exp\left(-i\pi \hat{S}^z_l\right)\right] = 0$, the ground state of the system is characterized by the number of local $|0\rangle_l$ states. A local spin-1 wavefunction is restricted by the local symmetry to be either the $\hat{S}^l_z$ eigenstate $|0\rangle_l$ or a superposition of $|+1\rangle_l, |-1\rangle_l$ states, parametrized like:

$$|\psi\rangle_l = \sin\theta \, |+1\rangle_l + e^{i\phi} \cos\theta \, |-1\rangle_l . \tag{4.15}$$

For this reason, if we limit ourselves to repeating spin configurations with periodicity 1 or 2, corresponding to translational invariant or symmetry-broken spin configurations, we only have three kinds of possible ground states:

- the spin wavefunction is a collection of quadrupolar states $|\psi_s\rangle = \otimes_i |0\rangle_{l(i)}$, which is the only state of the global symmetry sector $\exp\left(-i\pi \sum_i \hat{S}^z_{l(i)}\right)$ of maximal eigenvalue $+L$, where L is the number of spin-1 sites. The induced effective bosonic hopping has uniform strengths equal to $t - \alpha\kappa$. The spin wavefunction is characterized by ferroquadrupolar order, where all spin-1 states have directors aligned to the z axis.
- $|\psi_s\rangle$ lives in the eigenspace of $\exp\left(-i\pi \sum_i \hat{S}^z_{l(i)}\right)$ with zero eigenvalue. This eigenspace is spanned by states of alternating $|0\rangle$ quadrupoles on odd (even) sites and wavefunctions like Eq. (4.15) on even (odd) sites. Since repeating spin patterns of periodicity 2 are symmetry-broken configurations, the ground state of a periodic chain is two-fold degenerate. The two configurations have repeating dimers $|0\rangle_{l(i)} \otimes |\psi\rangle_{l(i+1)}$ and $|\psi\rangle_{l(i)} \otimes |0\rangle_{l(i+1)}$ respectively, which live in different local symmetry sectors. Each spin wavefunction of this sector features an intertwined quadrupolar-nonquadrupolar order.
- There are no local $|0\rangle_l$ states in the ground state, which lives in the symmetry sector of $\exp\left(-i\pi \sum_i \hat{S}^z_{l(i)}\right)$ with eigenvalue $-L$. Since local

states $|+1\rangle_l, |-1\rangle_l$ are degenerate eigenstates of the local symmetry, the eigenspace of the global symmetry is extensively degenerate. The ground state in this sector features both uniform configurations of local spin states like Eq. (4.15) and Néel-ordered local spin states with different $\theta, \phi, \theta', \phi'$, depending on the energy which minimizes the effective bosonic Hamiltonian.

The ferroquadrupolar states, where $|\psi_s\rangle = \otimes_i |0\rangle_{l(i)}$, are protected by the local symmetry. In the same way, the intertwined ferroquadrupolar - dipolar are protected by the same local symmetry, although the nature of the local dipolar states is allowed to change since both $|+1\rangle_l$ and $|-1\rangle_l$ are degenerate under $\exp\left(-i\pi\hat{S}_l^z\right)$.

4.2.a Ground state mean-field ansatz

Taking advantage of the local symmetries of Eq. (4.13), we propose a mean-field treatment of the ground state under the same assumptions reported in Appendix A. We suppose that the wavefunction of the ground state was separable between the bosonic part of the system and the degrees of freedom living on the bonds of the chain. This assumption leads to a Born-Oppenheimer ansatz: the dynamic of the spin degrees of freedom is assumed to be of orders of magnitude slower than the bosonic one. The bosonic particles adapt instantaneously to the effective Hamiltonian induced by the configuration of the spins. After a Jordan-Wigner transformation identical to the one reported in subsection 2.3.a, the wavefunction is assumed to be:

$$|\Psi_{\text{GS}}\rangle = |\psi_f\rangle \otimes_i |\psi\rangle_{l(i)}\,, \tag{4.16}$$

where $|\psi_f\rangle$ describes fermions (or hardcore bosons) and $|\psi_s\rangle = \otimes_i |\psi\rangle_{l(i)}$ the spin-1 sites.

Following the same reasoning which led to Eq. (2.25), we compute the effective fermionic bulk Hamiltonian by evaluating the local spin-1 operators of Eq. (4.13). The possible local spin-1 wavefunctions are the quadrupolar state $|0\rangle_l$ and the family of states in Eq. (4.15). For the fermionic and spin interaction we find:

$$\begin{aligned} s_l &= \langle\psi|\, \hat{S}_l^z - \kappa\hat{O}_l\, |\psi\rangle_l \\ &= -\cos 2\theta + \frac{\kappa}{2}\left(1 - \sin 2\theta \cos\phi\right), \end{aligned} \tag{4.17}$$

with local wavefunctions like Eq. (1.6), while for local $|0\rangle_l$ states the interaction

reads $s_l = -\kappa$. For the spin-1 on-site field instead we find:

$$\begin{aligned} d_l &= \langle\psi|\, \hat{S}_l^z \,|\psi\rangle_l \\ &= -\cos 2\theta \end{aligned} \tag{4.18}$$

for wavefunctions parametrized by θ, ϕ, while for local $|0\rangle_l$ states it vanishes $d_l = 0$.

In subsection 2.3.a, we restricted our variational spin parameters $\{s_{l(i)}\}$ to repeating blocks of pairs s_A, s_B. In the following study, the spin parameters $\{s_{l(i)}, d_{l(i)}\}$ are restricted once again to repeating blocks s_i, d_i with $i \in A, B$. Then the periodic chain is described by an enlarged unit cell of A, B pairs and the effective fermionic Hamiltonian is computed in exactly the same way of Eq. (2.19) and reads:

$$\hat{H}_f = -\sum_k (c_{kA}, c_{kB})^\dagger \left[\mathbf{v}(k) \cdot \boldsymbol{\sigma}\right] (c_{kA}, c_{kB}), \tag{4.19}$$

with bulk vector $\mathbf{v}(k)$ identical to the one in Eq. (2.20), but where its parameters s_A, s_B now take the values in Eq. (4.17), (4.18) or their counterparts for $|0\rangle_l$ local states.

The total energy ansatz, dependent on $s_i, d_i,\ i \in A, B$, reads:

$$\epsilon(s_A, s_B, d_A, d_B) = -\frac{2}{\pi} t_{AB}(s_A, s_B) E (1 - \delta_{AB}(s_A, s_B)^2) + \frac{\Delta}{4}(d_A + d_B) \tag{4.20}$$

With this result, we restrict our ansatz to one of the spin configurations introduced in the previous section, find the values for the variational angles θ, ϕ that minimize the energy of such spin configuration and finally compare its value across different symmetry sectors.

The uniform, ferroquadrupolar configuration is characterized by a locally separable spin wavefunction $|\psi_s\rangle = \otimes_i |0\rangle_{l(i)}$, thus $s_A = s_B = -\kappa$ and $d_A = d_B = 0$. We denote its energy from the ansatz in Eq. (4.20) as ϵ_{00}, which is:

$$\epsilon_{00} = -\frac{2}{\pi} (t - \alpha\kappa)\,. \tag{4.21}$$

The symmetry-broken phases displaying alternating $|0\rangle$ states and dipolar states have energies parametrized by θ, ϕ, which characterize the nonquadrupolar state in Eq. (4.15). The energy of this intertwined configuration, $\epsilon_{0\theta}$, reads:

$$\epsilon_{0\theta} = -\frac{2}{\pi} t_{0\theta}(\theta, \phi) E \left(1 - \delta_{0\theta}(\theta, \phi)^2\right) - \frac{\Delta}{4} \cos 2\theta, \tag{4.22}$$

where the dependence on θ, ϕ takes the following forms:

$$t_{0\theta}(\theta,\phi) = t - \frac{\alpha}{4}\left(\kappa\left(1+\sin 2\theta\cos\phi\right)+2\cos 2\theta\right), \tag{4.23}$$

and:

$$\delta_{0\theta}(\theta) = \frac{\alpha}{4t_{AB}(\theta)}\left(\left(\sin 2\theta\cos\phi-3\right)\kappa+2\cos 2\theta\right). \tag{4.24}$$

The values of θ, ϕ which minimize Eq. (4.22) also characterize which dipolar state $|\psi\rangle_l$ alternates with the state $|0\rangle_l$.

For the symmetry-broken phase without $|0\rangle$ states, the energy depends on four angles θ_A, ϕ_A and θ_B, ϕ_B. Its variational energy, denoted by ϵ_{AB}, reads:

$$\epsilon_{AB} = -\frac{2}{\pi}t_{AB}(s_A,s_B)E\left(1-\delta_{AB}(s_A,s_B)^2\right) - \frac{\Delta}{4}\left(\cos\theta_A+\cos\theta_B\right) \tag{4.25}$$

where:

$$t_{AB}(s_A,s_B) = t+\frac{\alpha}{2}\left(\frac{\kappa}{2}\left(2-\sin 2\theta_A\cos\phi_A-\sin 2\theta_B\cos\phi_B\right)-\cos 2\theta_A-\cos 2\theta_B\right) \tag{4.26}$$

for the effective bosonic hopping and:

$$\delta_{AB}(s_A,s_B) = \frac{\alpha}{4t_{AB}(s_A,s_B)}\left(2\cos 2\theta_B-2\cos 2\theta_A+\sin 2\theta_B\cos\phi_B-\sin 2\theta_A\cos\phi_A\right). \tag{4.27}$$

We can minimize the previous ansatz numerically to obtain the required values of θ, ϕ. An analytical treatment is impractical due to the presence of the elliptic integral of the second kind $E(x)$.

We implement a `Python` script using `SciPy` routines to minimize the energy for $\alpha = 0.6t$ and $\Delta \in [0t, 2.5t]$, $\kappa \in [-1.5, 1.5]$. Since Eq. (4.27) is symmetric under the exchange of θ_A, θ_B, we also add a staggering potential to the ansatz $\epsilon\left(|1\rangle\langle 1|_A - |-1\rangle\langle -1|_B\right)$ with $\epsilon = 0.001t$. By artificially breaking translational invariance we facilitate the convergence of the minimization procedure.

The convergence of the numerical minimization is hindered by the roughness of the energy landscape since the minimization variables $\cos\theta_i, \cos\phi_i$ are independent but influence the same terms of the energy ansatz in Eq. (4.22). Going into detail, the minimization of the equation (4.25) is strongly dependent on the initial guess for the angles θ_i, ϕ_i for $i \in A, B$.

The graphs of the minimization can be found in Figure 4.2 for the ansatz in Eq. (4.22), in Figure 4.3 for (4.25). It's clear for both cases that the θ_i angles are close to the values $\pi/2, 0$, corresponding to the coherent states $|1\rangle, |-1\rangle$ respectively. Deviations from these values are present, as to be expected, and are strongly dependent on Δ, κ.

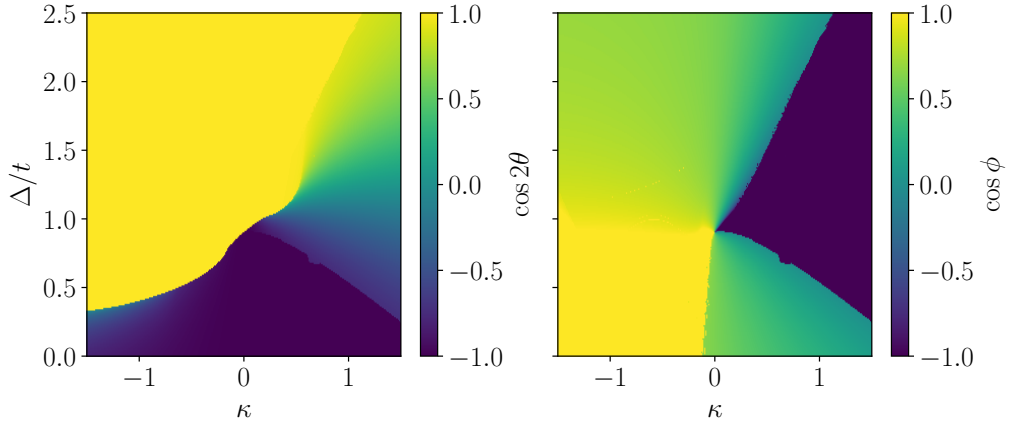

Figure 4.2: Numerical minimization of the energy of intertwined quadrupolar configurations $\epsilon_{0\theta}$. The left panel reports the values of $\cos 2\theta$ which minimize the energy, the right panel the values of $\cos\phi$. The minimization was done with $\alpha = 0.6t$, $\Delta \in [0, 2.5t]$ and $\kappa \in [-1.5, 1.5]$.

The mean-field ansatz of Eq. (4.16) predicts that the intertwined phases feature alternating pure quadrupolar-dipolar states, where the spin wavefunction is characterized by repeating $|0\rangle_{l(i)} \otimes |+1\rangle_{l(i+1)}$ dimers, for $\Delta/t \gg |\kappa|$, or by $|0\rangle_{l(i)} \otimes |-1\rangle_{l(i+1)}$ for $\Delta/t \ll |\kappa|$.

For the minimization of Figure 4.3, we find instead that the minimum of the energy features both two uniform regions for $\Delta \ll t$ and $\Delta \gg t$, where spins are all $|+1\rangle$ and $|-1\rangle$ coherent states respectively, and an intermediate central region where spins feature Néel ordered, mostly dipolar states with $\theta_A \simeq \pi/2$ and $\theta_B \simeq 0$.

The critical lines obtained from the numerical minimization of the ansatz are reported in Figure 4.4 and show that the parameter space is divided in regions of different global symmetry sectors: a ferroquadrupolar region, a region featuring intertwined ferroquadrupolar-dipolar order and a nonquadrupolar region for $\kappa > 0$. As mentioned previously, the minimization of the region without $|0\rangle$ states depends strongly on the initial guess for the angles θ_A, ϕ_A and θ_B, ϕ_B which minimize the energy of Eq. (4.25). The graphs in Figure 4.4 are to be considered as a qualitative analysis of the regions of parameter space.

4.2.b Numerical results

In this section we investigate numerically the properties of the ground state of Eq. (4.13). We perform the exact diagonalization of the aforementioned Hamiltonian using the Python package `QuSpin` [35]. The numerical study involves periodic boundaries and characterizes different regions of parameter space. Our focus

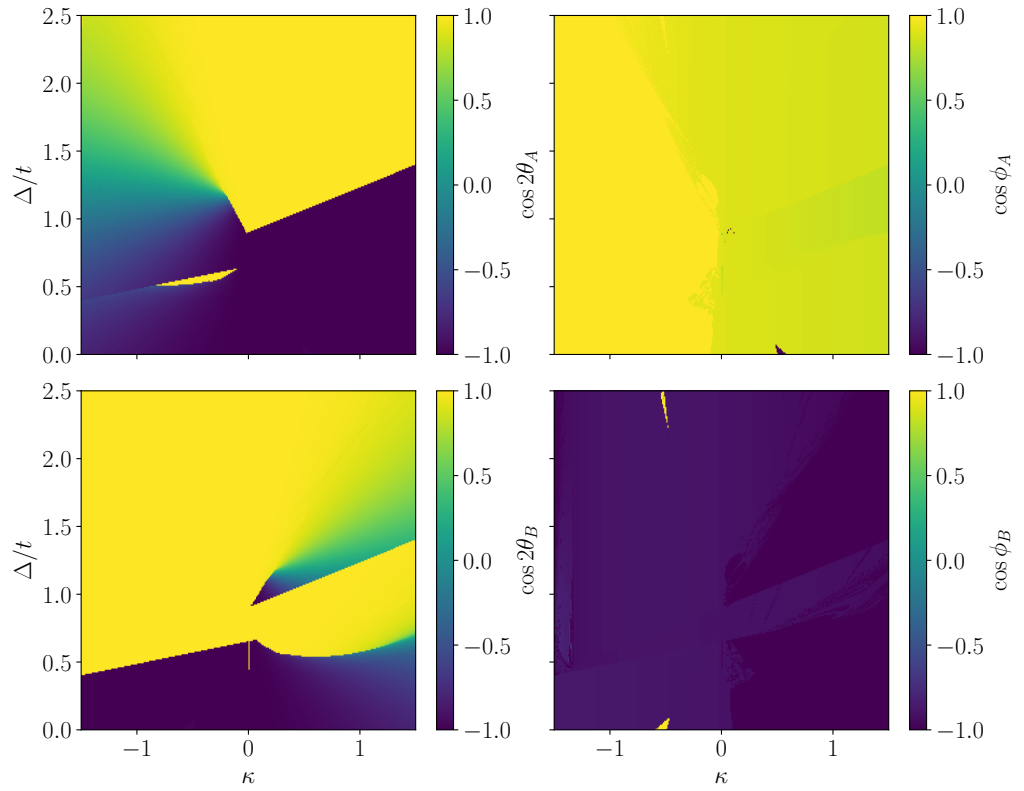

Figure 4.3: Numerical minimization of the energy of symmetry-broken, nonquadrupolar configurations ϵ_{AB}. Top panels refer to spin sites A of the enlarged unit cell, bottom panels to spin site B. Left panels report the values of $\cos 2\theta_i$ which minimize the energy, right panels the values of $\cos \phi_i$ for $i \in A, B$. The minimization was done with $\alpha = 0.6t$, $\Delta \in [0, 2.5t]$ and $\kappa \in [-1.5, 1.5]$ and a staggering field $\epsilon = 0.001t$.

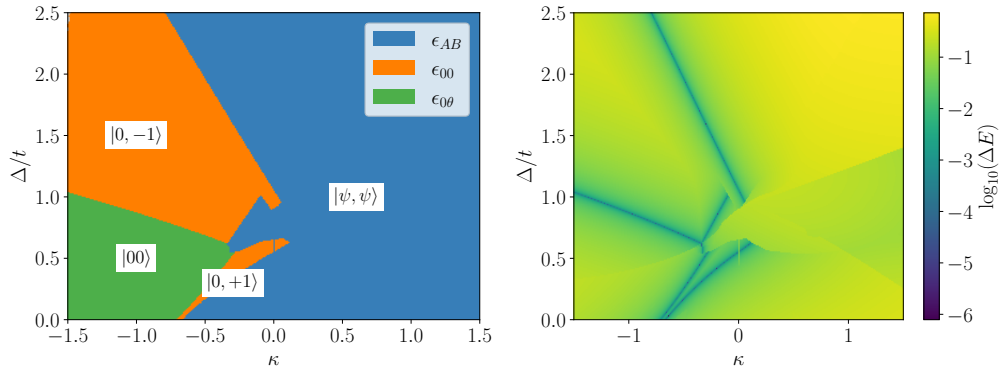

Figure 4.4: Symmetry sectors in the ground state for the numerical minimization. Left: lowest energies out of the three possible ground states introduced in subsection 4.2.a. Right: Energy difference between the two lowest energy symmetry sectors. The minimization was done with $\alpha = 0.6t$, $\Delta \in [0, 2.5t]$ and $\kappa \in [-1.5, 1.5]$ and a staggering field $\epsilon = 0.001t$.

is on the half filling properties of the system, since previous numerical studies of the Hamiltonian in Eq. (2.11) have found a strong dependence on the filling fraction [23].

We start with the results for a periodic chain of 6 bosonic sites, 6 spin-1 sites and 3 bosons. The local bosonic Hilbert space is truncated to a maximum of 1 boson per site, thus enforcing the limit for hardcore bosons $U \to +\infty$. With this restriction, the simulated Hilbert space is composed of 14580 states. We focus on the region of parameter space where $\alpha = 0.6t$, $\Delta \in [0t, 2.5t]$, $\kappa \in [-1.5, 1.5]$. Lastly, as discussed in [23], we also include a small artificial perturbation which splits the degeneracy of the ground state of the symmetry-broken phases:

$$H_\epsilon = \epsilon \sum_i (-1)^i \hat{S}_i^z, \tag{4.28}$$

where $\epsilon = 0.001t$. Except for when explicitly stated, all the following numerical results were obtained with the addition of this small perturbation.

From the exact diagonalization of the Hamiltonian in Eq. (4.13), we report in Figure 4.5 representative ground state configurations of the phase space of the ones anticipated in subsection 4.2.a. These are: the site-separable ferro-quadrupolar region with uniform spin wavefunction $\otimes_i |0\rangle_{l(i)}$; the two symmetry-broken configurations with alternating spin states $|0\rangle, |-1\rangle$ and $|0\rangle, |+1\rangle$ respectively; the two uniform regions where the local spin-1 wavefunction is a superposition of $|+1\rangle, |-1\rangle$ states.

We are interested in studying the regions of parameter space characterized by a breaking of the periodic chain's translational symmetry or by the presence of

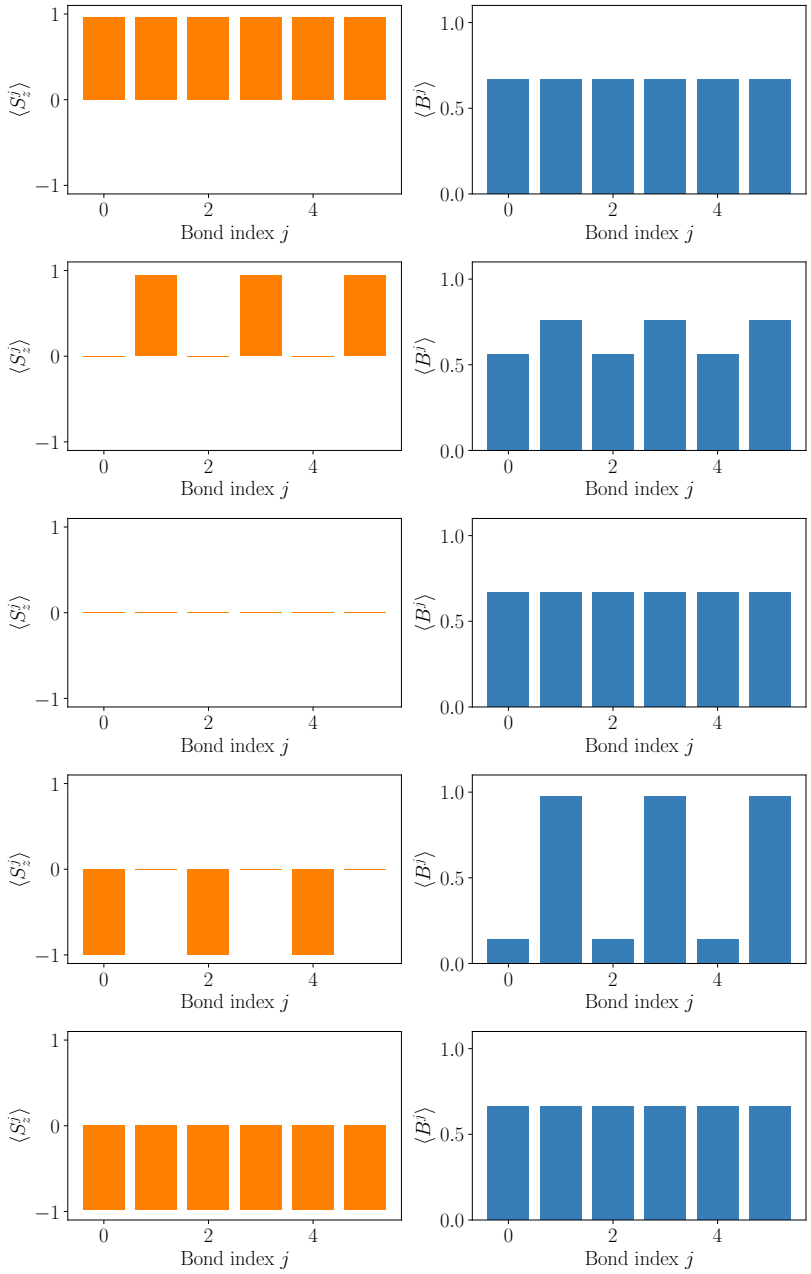

Figure 4.5: Expectation values for each spin $\hat{S}_j^z$ on the jth bond (right panels) and bosonic hopping amplitudes $\hat{B}_j$ of Eq. (2.31) along the chain (left panels) for five points of the configuration space. Here $\beta = 0t$, $\alpha = 0.6t$, $\kappa = -0.37$ and $\epsilon = 0.001t$. From top to bottom: for $\Delta = 0.2t$, the spins are all in a uniform configuration and bosons hop uniformly along the chain. For $\Delta = 0.4t$ we are in the Néel region where spins alternate between $|0\rangle$ states and mostly $|+1\rangle$ states. The bosonic hoppings dimerize accordingly. For $\Delta = 0.6t$ we are in the ferroquadrupolar region. All spins are in the state $|0\rangle$ and bosonic hoppings are uniform. For $\Delta = 1.2t$ we enter the Néel region opposite to the previous one, where spins alternate in between $|0\rangle$ and mostly $|-1\rangle$ states. For $\Delta = 1.9t$ spins align to a mixture of $|+1\rangle, |-1\rangle$ states.

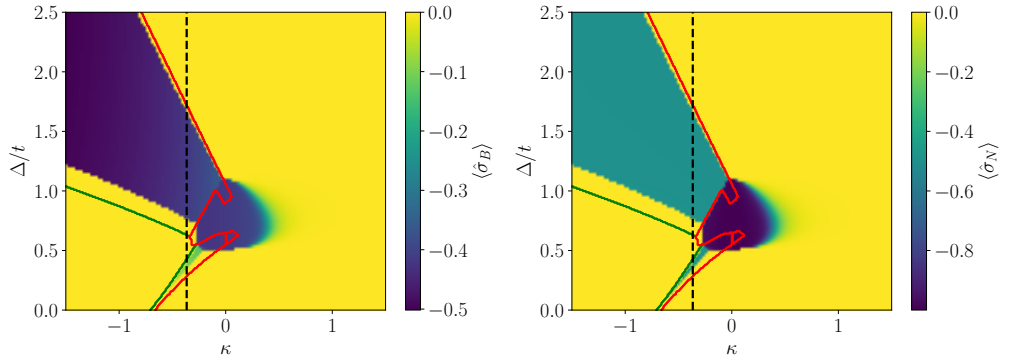

Figure 4.6: Phase space for the region $\alpha = 0.6t$, $\kappa \in [-1.5, 1.5]$, $\Delta \in [0, 2.5t]$. Simulations were run with $\epsilon = 0.001t$ which selects one of the symmetry-broken states in the dimerized region. Expected values on the ground state for the staggered spin magnetization $\hat{\sigma}_N$ (left) and staggered hopping amplitude $\hat{\sigma}_B$ of Eq. (2.31) (right). The yellow regions identify uniform configurations where translational invariance of the periodic chain is preserved. The colored regions instead are symmetry broken regions where spins are Néel ordered and bosons show bond-density waves. The red and green lines mark the boundaries of the symmetry sectors found with the mean-field ansatz. The red line is numerically unstable. The dashed vertical line corresponds to $\kappa = -0.37$.

quadrupolar order in the local spin-1 wavefunction. As a consequence, we measure the staggered hopping amplitude $\hat{\sigma}_B$ (2.31) and the staggered magnetization of the ground state:

$$\hat{\sigma}_N = \frac{1}{L} \sum_i (-1)^i \hat{S}^z_{l(i)}, \tag{4.29}$$

and the quadrupolar order parameter u^2 presented in Eq. (3.30).

The first two metrics can be found in Figure 4.6. The bosonic hopping amplitude staggers in well-defined regions for $\kappa < 0$ and $\kappa \ll 1$, marking a spontaneous breaking of the discrete translational invariance of the chain. Furthermore, the staggered magnetization characterizes three different regions for the symmetry-broken configurations: one where its value is maximal, $|\langle \hat{\sigma}_N \rangle| = 1$ and two disconnected regions where its value is intermediate, $|\langle \hat{\sigma}_N \rangle| \approx 0.5$. As stated in the previous chapter, these three regions are dominated by Néel ordered, separable spin states. The local spin-1 wavefunction is mainly composed of alternating $|+1\rangle$, $|-1\rangle$ states where $|\langle \hat{\sigma}_N \rangle| = 1$, while where $|\langle \hat{\sigma}_N \rangle| \approx 0.5$ the ground state mostly features alternating $|0\rangle$ and $|\pm 1\rangle$ states.

While $\hat{\sigma}_B$ (2.31) and $\hat{\sigma}_N$ (4.29) are global observables of the chain, u^2 is a local observable with values on each spin-1 site. Since we are interested in finding the regions that feature even a single local quadrupolar state, in Figure 4.7 we report the maximum value of u^2 measured along the chain.

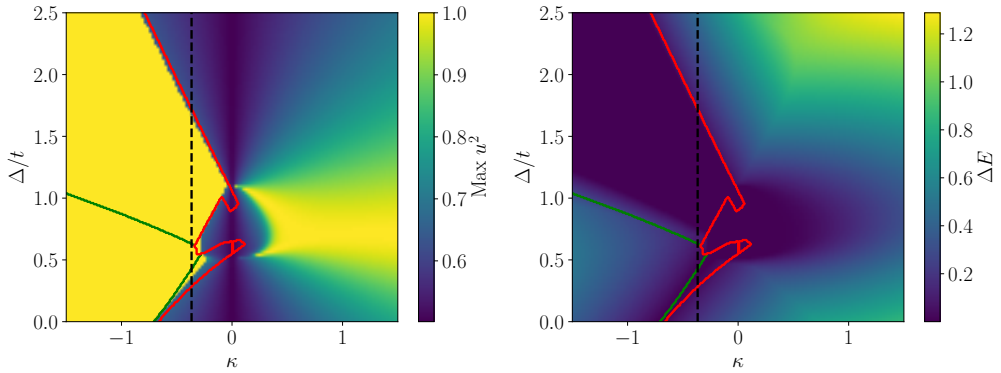

Figure 4.7: Phase space for the region $\alpha = 0.6t$, $\kappa \in [-1.5, 1.5]$, $\Delta \in [0, 2.5t]$. Simulations were run with $\epsilon = 0.001t$. Left: maximum value of the local quadrupolar order parameter u^2 along the chain. The yellow regions identify configurations where some spin-1 states are in a quadrupolar state or in a mixed state. Right: Energy difference between the ground state and the first excited state. Symmetry-broken regions feature a vanishing energy gap due to the presence of a two-fold degenerate ground state. The red and green lines mark the boundaries of the symmetry sectors found with the mean-field ansatz. The red line is numerically unstable. The dashed vertical line corresponds to $\kappa = -0.37$.

From the values of u^2 we find spin-1 local states that are purely quadrupolar both in a subregion of the broken symmetric phase and in a region where the chain is instead uniform. The region marked by the presence of local quadrupolar spin-1 states and symmetry breaking features alternating purely quadrupolar and almost purely coherent spin-1 states. It's a region protected by the local symmetry introduced in the previous chapter, where odd spin-1 sites (or even, depending on the sign of ϵ) are locked to the state $|0\rangle$ while even (or odd) spin-1 sites are superpositions of $|+1\rangle, |-1\rangle$.

Furthermore, the region where symmetry breaking does not occur but spin-1 states show $u^2 = 1$ is the uniform, site-separable ferroquadrupolar spin-1 wavefunction. This region is protected by the same local spin-1 symmetry so its boundaries are exact level crossings in between different symmetry sectors.

Regions that feature spontaneous symmetry breaking of translational invariance must have a two-fold degenerate ground state, since the two dimerized ground states can be connected by translation of one site. We verify this property by plotting in Figure 4.7 the energy difference between the lowest two energy levels. Indeed, all regions with nonzero dimerization feature a two-fold degenerate ground state.

Our analytical understanding of the Peierls transition for the model (2.11) is based on the hypothesis that the ground state is a factorized wavefunction

of bosons and separable spins. This hypothesis is at the core of the Born-Oppenheimer ansatz used in [23] and repeated in Appendix A. Through our numerical study, we find that this hypothesis holds only for $\kappa < 0$, as the right side of the graphs presented in Figure 4.7 is characterized by non-separable spins and significantly entangled spins and bosons. We do so by studying the Von Neumann entropy S_E of the chain between its bosonic $|\psi\rangle_b$ and spin $|\psi\rangle_s$ contributions. We also compute the purity of the reduced density matrix $\mathrm{Tr}\left[\rho_s^2\right]$ of a single spin-1 after tracing out all the remaining bosonic and spin sites. Due to the periodicity of the chain, the choice of the single site wavefunction is not relevant.

Data for the entanglement entropy S_E and the purity $\mathrm{Tr}\rho_s^2$ of the bipartitions along the parameter space are in Figure 4.8. The ground state always features entangled bosonic and spin states, except for the uniform ferroquadrupolar region which is protected by the local symmetry. Since $|0\rangle_l$ is nondegenerate for $\exp\left(-i\pi\hat{S}_l^z\right)$ with eigenvalue $+1$, the global ferroquadrupolar spin wavefunction is the only state of the global symmetry $\exp\left(-i\pi\sum_i \hat{S}_{l(i)}^z\right)$ of maximal eigenvalue $+L$. The other regions instead show nonzero quantum fluctuations so the ansatz of Eq. (4.16) is not exact. Even in this case, the amount of entanglement generated is negligible for the symmetry-broken regions where $S_E \approx 0.01$ and exactly zero for the ferroquadrupolar one.

For $\kappa > 0$ instead quantum fluctuations become extremely relevant: we cannot study this region using the Born-Oppenheimer approach.

Since the ground state ansatz holds only in the leftmost regions of Figure 4.11, we focus our numerical studies to the region $\kappa < 0$. We note that, because of the local symmetry of Eq. (4.13), for $\kappa > 0$ we find a uniform region devoid of local $|0\rangle$ states. The presence of regions where $u^2 \approx 1$ is explained by the superposition of nonseparable bosonic and spin sites with local opposite $|+1\rangle$, $|-1\rangle$ spin-1 states and relevant entanglement in between bosons and spin-1.

We proceed by selecting a vertical cut of the parameter space, for $\kappa = -0.37$. By imposing $\epsilon = 0.001t$ we select one of the two symmetry-broken states in order to compare its behavior to the proposed ansatz. The chosen vertical cut crosses all four regions introduced in the previous section: from the one devoid of $|0\rangle$ states for $\Delta \approx 0$ to the symmetry-broken one with alternating $|0\rangle$ and $|+1\rangle$ states, then the ferroquadrupolar region, the alternating $|0\rangle, |-1\rangle$ region and again the uniform region devoid of $|0\rangle$ for $\Delta > 2$.

The energy gap in between the ground state and the lowest energy states is reported in Figure 4.9 and indeed the regions featuring spontaneous symmetry-breaking of translational invariance are also degenerate at finite size with periodic boundaries.

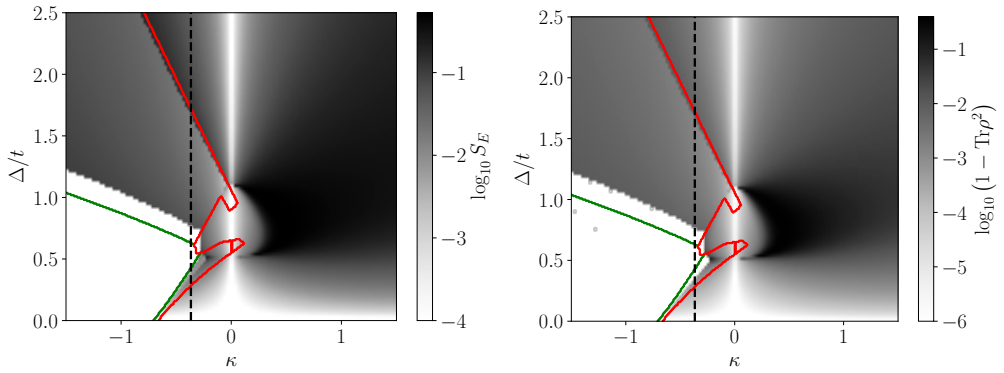

Figure 4.8: Phase space for the region $\alpha = 0.6t, \kappa \in [-1.5, 1.5]$, $\Delta \in [0, 2.5t]$. Simulations were run with $\epsilon = 0.001t$. Left: entanglement entropy S_E between bosonic and spin states. Right: purity of the reduced density matrix $\mathrm{Tr}\left[\rho_{ss}^2\right]$ of a single spin, after tracing out the remaining Hilbert space. For $\kappa < 0$ and far from the crossings between different local symmetry sectors, both values are nonzero but small. The red and green lines mark the boundaries of the symmetry sectors found with the mean-field ansatz. The red line is numerically unstable. The dashed vertical line corresponds to $\kappa = -0.37$.

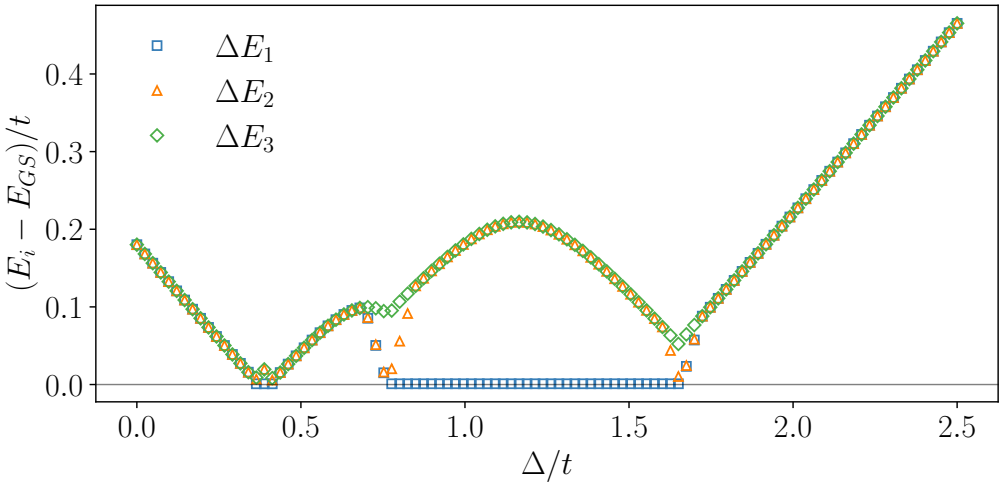

Figure 4.9: Energy difference in between the first three excited levels and the ground state for $\alpha = 0.6t$, $\Delta \in [0, 2.5t]$, $\kappa = -0.37$ and $\epsilon = 0t$. The central region and the smaller region for $\Delta \sim 0.4t$ features a twofold degenerate ground state as ΔE_1 is zero.

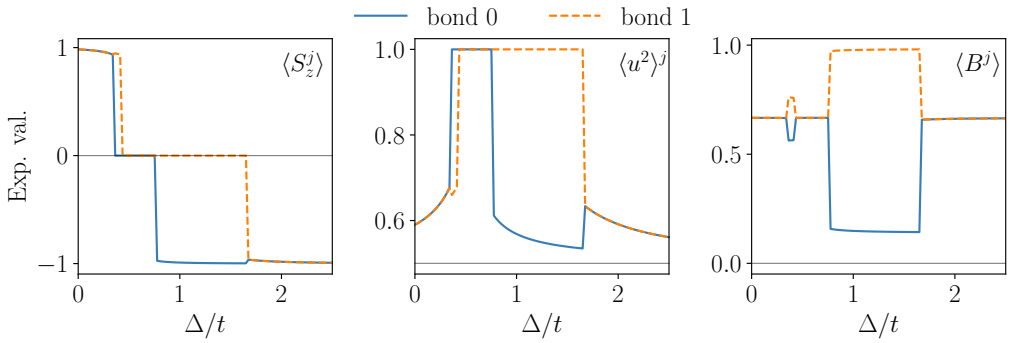

Figure 4.10: Expectation values of three local operators on the jth bonds with $j \in 0, 1$ for $\alpha = 0.6t$, $\Delta \in [0, 2.5t]$, $\kappa = -0.37$ and $\epsilon = 0.001t$. From left to right: $\hat{S}^z_j$, u^2_j and the bond hopping strength $\hat{B}_j$.

Having selected one of the two symmetry-broken ground states we compute the expectation values of the local observables $\hat{S}_{l(i)}$, $u^2_{l(i)}$ and $\hat{B}_{l(i)}$ and report them in Figure 4.10. The two dimerized regions feature intermediate spin lengths, as $\langle S^z_{l(i)} \rangle$ is not exactly equal to ± 1 and the quadrupolar order parameter u^2 assumes values different from $1/2$. These effects are both related to the finite size of the system and to the fact that the ground state is not a site-separable wavefunction. The numerical minimization of the ansatz states that the ground state is indeed composed of alternating $|0\rangle, |-1\rangle$ or $|0\rangle, |+1\rangle$ spin states, but these effects induce both the entanglement of spins and bosons and the superposition of opposite spin states $|+1\rangle, |-1\rangle$. The spin sites characterized by $|0\rangle$ states are instead once more protected by the local symmetry.

In Figure 4.11 we plot the aforementioned entanglement entropy S_E and reduced density matrix purity along the cut. Both observables maintain small values, except for the regions close to the transitions across different symmetry sectors.

The quadrupolar character of spin-1 states leads also to a nontrivial expectation value of the quadrupolar operators of Eq. (3.1). As shown in Figure 4.12, the separable $|0\rangle$ state present both in the ferroquadrupolar region and in the intertwined region is protected by the local symmetry. The $\hat{S}_z$ eigenstate $|0\rangle$ is also a zero-valued eigenstate of $\hat{S}^2_z$ and an eigenvalue of the quadrupolar operators $\hat{S}^2_x, \hat{S}^2_y$ of eigenvalue 1. Indeed, the expectation value of $\hat{Q}_{z^2} = (S^z)^2$ is exactly zero when evaluated on a local $|0\rangle$ state, while $\hat{Q}_{x^2}, \hat{Q}_{y^2}$ are exactly one. Furthermore, we see from the expectation values of the operators $\hat{Q}_{x^2}, \hat{Q}_{y^2}$ that the partially coherent states present in the regions without ferroquadrupolar ordering are uneven superpositions of $|+1\rangle, |-1\rangle$ states, as both $(|+1\rangle + |-1\rangle)/\sqrt{2}$ and $(|+1\rangle - |-1\rangle)/\sqrt{2}$ are eigenstates of eigenvalue 1 or 0 of said operators. This

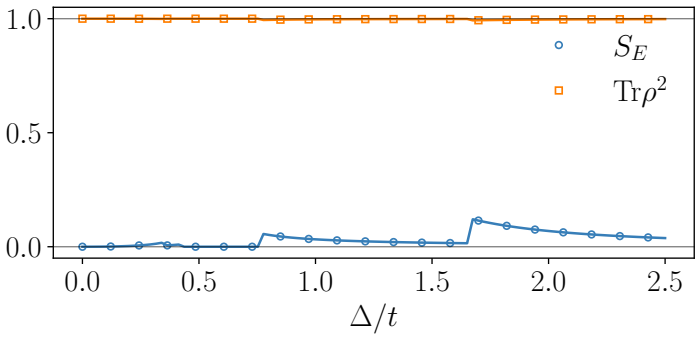

Figure 4.11: Entanglement entropy S_E between bosons and spins and reduced density matrix purity $\mathrm{Tr}\rho_{ss}^2$ of a single spin site along the vertical cut corresponding to $\alpha = 0.6t$, $\Delta \in [0, 2.5t]$, $\kappa = -0.37$ and $\epsilon = 0.001t$. The entanglement entropy S_E is computed in between bosonic and spin-1 degrees of freedom (circles), while $\mathrm{Tr}\rho_{ss}^2$ is the purity of the reduced density matrix of a single spin-1 after tracing all other degrees of freedom.

result contradicts the mean-field results of the previous section, which instead predicted a separable spin wavefunction with alternating $|0\rangle$ and $|\pm 1\rangle$ states in those regions of parameter space. As shown in Figure 4.11, the ground state is not an exactly separable wavefunction and thus the ansatz is not valid. Furthermore, the relatively small size of the chain studied increases the relevance of finite-size effects.

Having studied the specific symmetry-broken configurations, we remove the infinitesimal perturbation setting $\epsilon = 0$. All symmetry-broken configurations are exactly degenerate, since they live in different symmetry sectors of the local symmetry. In order to prove the presence of correlations in the unperturbed ground state, we compute the expected value of the correlator $\hat{U}^0\hat{U}^r$ where $\hat{U}^r = \exp\left(-i\pi\hat{S}_r^z\right)$. The operator $\hat{U}^r$ has eigenvalue $+1$ if the local spin state of the rth bond is $|0\rangle$, while has two degenerate eigenvalues -1 for all superpositions of the states $|+1\rangle, |-1\rangle$. If Néel order is present, where states alternate in between $|0\rangle$ and local superpositions of $|+1\rangle, |-1\rangle$, the correlator $\hat{U}^0\hat{U}^1$ assumes value -1. If instead the ground state is found in a separable, uniform configuration the correlator assumes value $+1$. In Figure 4.13 we report its values along the vertical cut and for various distances $r \in \{1, 2, 3\}$. The spin wavefunction features long range order both in its uniform regions and in its Néel ordered regions.

In conclusion, we report in Figure 4.14 the regions found using exact diagonalization techniques. We use the notation $|\Uparrow\rangle_l, |\Downarrow\rangle_l$ to represent local spin-1 states like Eq. (4.15), which are quantum superpositions of coherent states $|+1\rangle_l, |-1\rangle_l$. As can be seen in Figure 4.10, these superpositions feature partially developed dipolar moments such that $\langle\hat{S}_l^z\rangle \neq 0$ but $\left|\langle\hat{S}_l^z\rangle\right| \leq 1$. The direction of the ar-

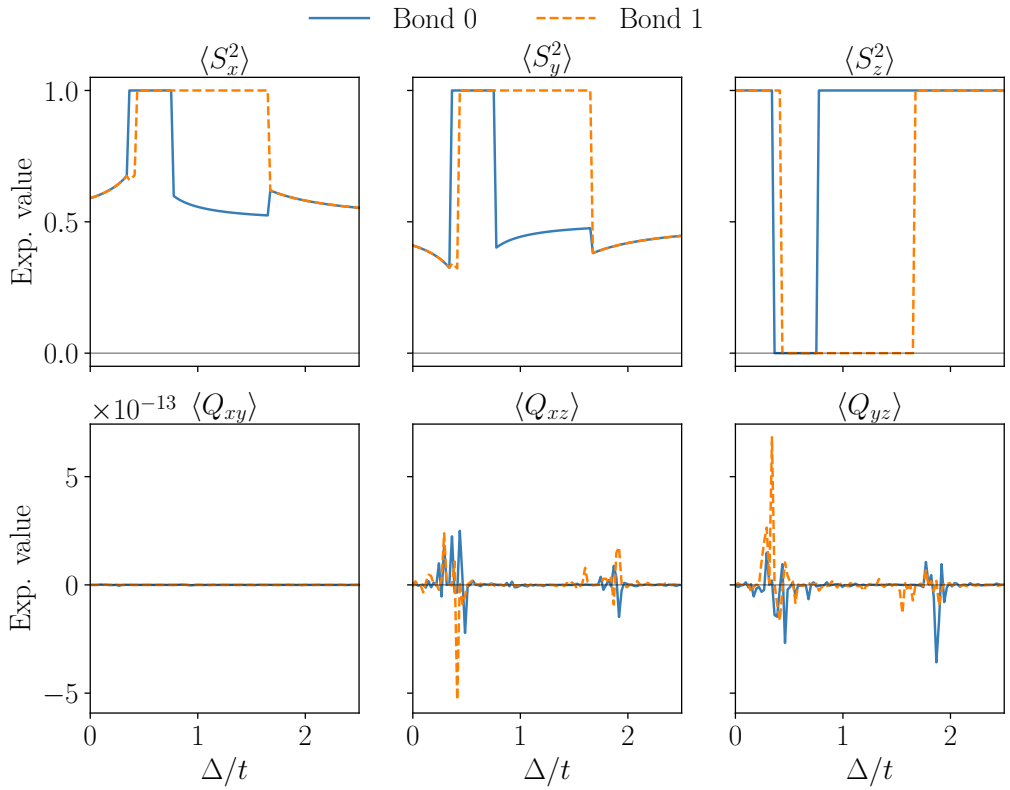

Figure 4.12: Expectation values of the local quadrupolar operators of Eq. (3.1) for $\alpha = 0.6t$, $\Delta \in [0, 2.5t]$, $\kappa = -0.37$ and $\epsilon = 0.001t$. The top three panels report the quadratic operators $(\hat{S}_j^x)^2, (\hat{S}_j^y)^2, (\hat{S}_j^z)^2$ while the bottom panels report the anticommutators of the spin-1 operators $\hat{S}_j^x, \hat{S}_j^y, \hat{S}_j^z$.

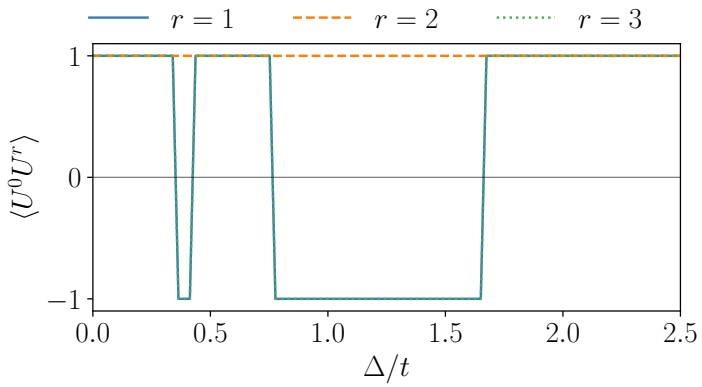

Figure 4.13: Expectation values of the correlator $\hat{U}^0 \hat{U}^r$ for $\alpha = 0.6t$, $\Delta \in [0, 2.5t]$, $\kappa = -0.37$ and $\epsilon = 0$.

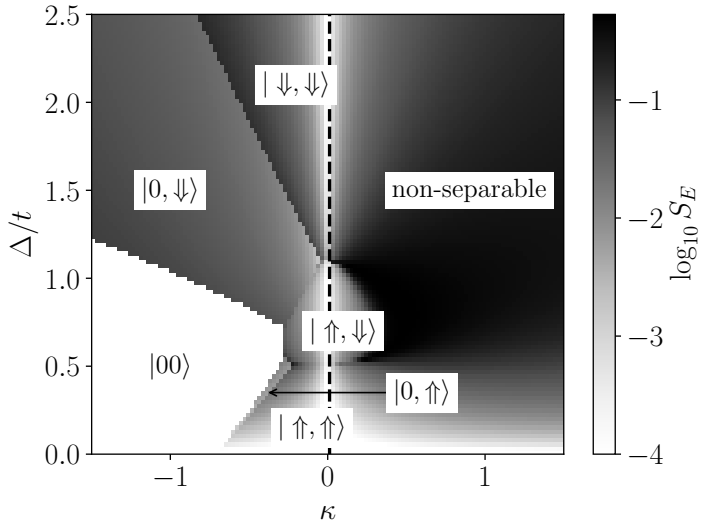

Figure 4.14: Entanglement entropy S_E between bosonic and spin-1 sites on the ground state and its characterization in the identified regions. Simulations were run with $\epsilon = 0.001t$ in the region $\alpha = 0.6t$, $\kappa \in [-1.5, 1.5]$, $\Delta \in [0, 2.5t]$. The $|\Uparrow\rangle, |\Downarrow\rangle$ states represent local spin-1 wavefunction with spin vector of intermediate length $\left|\langle \hat{S}_l^z \rangle\right| \leq 1$ and positive/negative direction of the spin identified by the direction of the respective arrow.

row coincides with the direction of the partially developed spin vector, thus $|\Uparrow\rangle_l$ represents a state with $\langle \hat{S}_l^z \rangle > 0$, while $|\Downarrow\rangle_l$ represents $\langle \hat{S}_l^z \rangle < 0$.

4.2.c Topology of the symmetry-broken phases and edge-modes

As we did for the Hamiltonian of Eq. (2.11), in this last section we study the topological properties of the ground state of Eq. (4.13). In particular, we prove the existence of an eigenstate hosting localized edge-states.

As shown for Eq. (2.19) in subsection 2.3.c, in the hard-core boson regime the effective fermionic energy of Eq. (4.19) can be written as the sum of the occupied single particle energy levels proportional to the vector modulus $|\mathbf{v}(k)|$ over the first Brillouin zone. Even for the spin-1 case, this effective Hamiltonian maps to the many body SSH Hamiltonian, up to constant terms. The spin-boson interaction coupling α leads to an interaction-induced topological effective bosonic SSH Hamiltonian. The ground state of Eq. (4.13) inherits the topological properties of the SSH Hamiltonian.

Furthermore, the winding number is computed in exactly the same way as for the original SSH model [20], thus confirming that the model of Eq. (4.13) presents two distinct and topologically disconnected symmetry broken phases

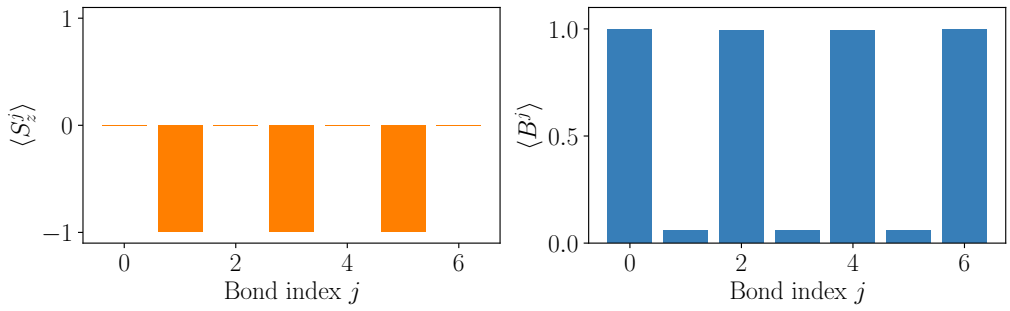

Figure 4.15: Ground state of the open chain for $\alpha = 0.6t$, $\Delta = 1.5t$, $\kappa = -0.8$ and $\epsilon = 0t$. The bond at the edges of the chain has strength $-t - \alpha\kappa$.

in two of its eigenstates.

The following numerical study involves an open chain of 8 bosonic and 7 spin-1 sites, filled with 3 and 5 hardcore bosons, corresponding to one particle below and one particle above half filling. At half filling, the Hilbert space hosts 153090 states. Furthermore, we focus on a specific choice of parameters $\alpha = 0.6t$, $\Delta = 1.5t$, $\kappa = -0.8$ and $\epsilon = 0$ which select one point in the symmetry-broken region featuring intertwined ferroquadrupolar-dipolar order.

For an open chain, one dimerized state starts and ends with a strong $-t - \alpha\kappa$ hopping strength, we refer to its spin wavefunction as $|0 \Downarrow \ldots \Downarrow 0\rangle$. Its spin configuration, starting and ending with $|0\rangle$ states, leads to a bosonic effective Hamiltonian equivalent to the trivial configuration of the SSH model. The chain in this state, reported in Figure 4.15, does not feature zero-energy edge modes and thus is trivial.

The eigenstate which instead starts with a weak bond, $|\Downarrow 0 \ldots 0 \Downarrow\rangle$, has a separable spin configuration which starts and ends with a $|\Downarrow\rangle$ state like Eq. (4.15) and features an intermediate dipolar moment. The effective bosonic Hamiltonian corresponds to the topological one of section 1.1 and this state features the zero-energy edge modes of Figure 4.16. For this reason, this state is nontrivial and topologically disconnected from the trivial one.

Exactly as discussed in subsection 2.3.c, for an open finite chain the topological and trivial eigenstates of Eq. (4.13) have different energies and the ground state is found in the configuration without edge states. Indeed, finite size effects increase the energy of the dimerized configuration which starts with a weak bond and the ground state is the trivial one $|0 \Downarrow \ldots \Downarrow 0\rangle$.

In the topological eigenstate of spin wavefunction $|\Downarrow 0 \ldots 0 \Downarrow\rangle$, the filling anomaly is accommodated by the emergence of edge-localized modes, as shown in Figure 4.16.

Similarly to the spin-$1/2$ case, the topological state is an excited state separated

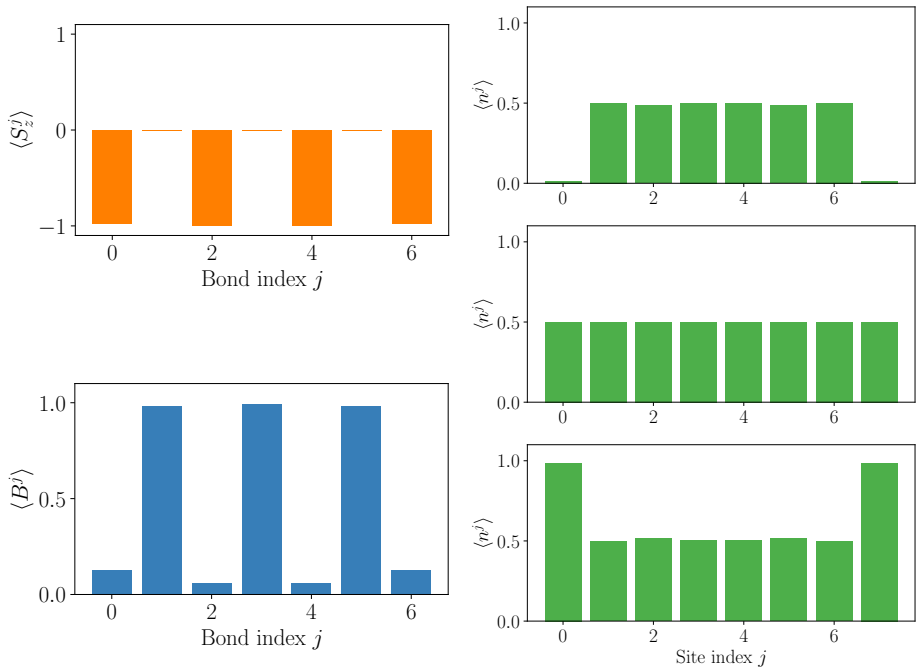

Figure 4.16: Local observables along the open chain for $\alpha = 0.6t$, $\Delta = 1.5t$, $\kappa = -0.8$ and $\epsilon = 0$ on the nontrivial excited state. Left: expectation values for the spin-1 $\hat{S}^z_{l(i)}$ component (top) and for the hopping amplitude $\hat{B}_{l(i)}$ (bottom) show that the edges have weak hoppings. Right: local bosonic densities along the chain for 3 (top), 4 (middle) and 5 (bottom) bosons. Filling anomalies lead to the emergence of localized zero energy edge modes.

from the ground state by a dense and extensive number of intermediate states. For our open chain of 8 bosonic, 7 spin-1 sites we report in Figure 4.17 the lowest energy eigenstates, we also highlight the position of the excited nontrivial state $|\Downarrow 0 \dots 0 \Downarrow\rangle$.

Differently from the Hamiltonian of Eq. (2.11), the topological state is protected by the local symmetry highlighted in the previous section, $\exp\left(-i\pi \hat{S}^z_l\right)$. Indeed, for an open chain of $2L$ spin sites, the trivial configuration has $L+1$ local $|0\rangle$ states on the odd bonds of the lattice, while the topological one features L local $|0\rangle$ states on the even bonds. The two are both topologically disconnected and live in different symmetry sectors.

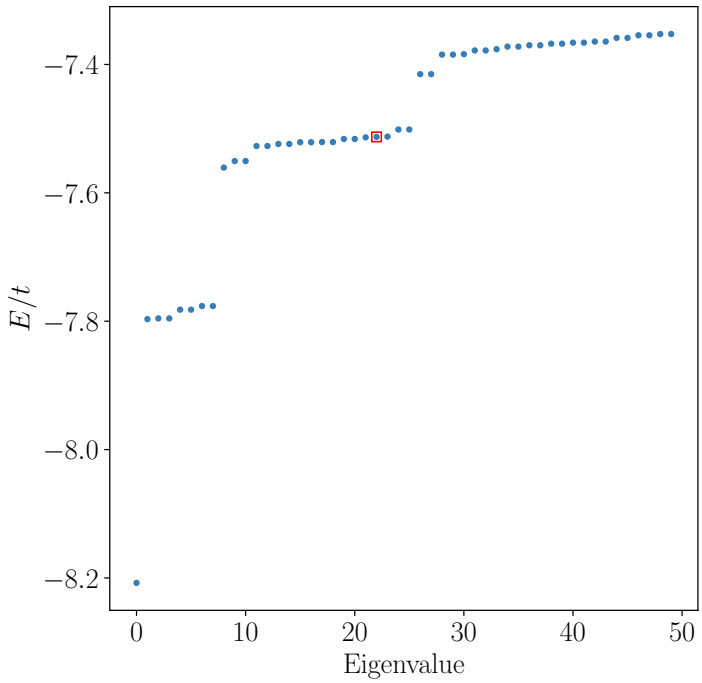

Figure 4.17: Lowest 50 energies for $\alpha = 0.6t$, $\Delta = 1.5t$, $\kappa = -0.8$ and $\epsilon = 0t$ on an open chain of 8 bosonic and 7 spin-1 sites. The nontrivial state $|\Downarrow 0 \ldots 0 \Downarrow\rangle$, marked with a red square, is an excited state for the Hamiltonian of Eq. (4.13).

5 Conclusions

The study presented in this thesis aims to provide a theoretical and numerical investigation of a one-dimensional lattice featuring bosons interacting with spin-1 degrees of freedom living on its bonds, which induce an effective Su-Schrieffer-Heeger bosonic many-body model. By combining a Born-Oppenheimer mean-field approach and exact diagonalization techniques, this work shows how the interplay of interactions, symmetry-breaking and topology may be used to engineer complex quantum states with the desired order. The extension from the spin-$1/2$ to the spin-1 degrees of freedom of the $\mathbb{Z}_2$ Bose-Hubbard model introduced by González-Cuadra et al. [20] allows for the emergence of quadrupolar, time-reversal invariant states showing long-range ferroquadrupolar or intertwined quadrupolar-dipolar order. Based on the spin-1 model introduced in this work, possible steps forward in future investigations would be the characterization of the phases present in the non-separable region, which goes beyond the Born-Oppenheimer ansatz, or study the adiabatic evolution of an open chain as it crosses the topological transition found numerically from the mean-field ansatz. As the main finding of this work, the interplay of interactions and symmetry-breaking leads to the formation of long-range order and topologically disconnected phases, which are leveraged to select the required spin-1 quadrupolar states. This result further generalizes what observed in the spin-$1/2$ case: while the spin-$1/2$ Hamiltonian features tunable fluctuations from its mean-field result, it also features the same ground state even under modifications of the nature of the degrees of freedom living on the bonds, as long as the Born-Oppenheimer ansatz is valid. By partially breaking the Born-Oppenheimer ansatz the ground state is allowed to explore different quantum phases, at the price of losing the tunability of the correlations.

Connecting theory with ongoing experimental realizations of qudit systems,

our model opens a novel direction for many-body physics in one-dimensional lattices and possibly introduces novel states featuring quadrupolar order which may be relevant for quantum simulation platforms.

A Minimization of the Born-Oppenheimer ansatz

In this appendix we give a general overlook on the ideas behind the ansatz of Eq. (2.25). The behavior of a system obeying the Hamiltonian (2.11) is connected to the Born-Oppenheimer ansatz deployed in chapter 2 and thus can be extended to different Hamiltonians. In this appendix we prove the existence of Néel ordered regions for a broad class of Hamiltonians similar to (2.11) under the Born-Oppenheimer ansatz.

We start with the hypothesis that the ground state wavefunction is separable between the bosonic (or fermionic) part of the system and the degrees of freedom living on the bonds of the chain. This assumption allows us to define the Born-Oppenheimer ansatz: the dynamic of the degrees of freedom living on the bonds is assumed to be significantly slower than the bosonic (fermionic) one. Equivalently, we suppose that the bosonic (or fermionic) particles adapt instantaneously to the effective Hamiltonian induced by the configuration of the bonds.

In order to expand from this idea, notice that in such regime the bosonic effective Hamiltonian is completely oblivious on the nature of the degrees of freedom which generated it: as long as the effective Hamiltonian is the same, the bosonic behavior is the same. This is meaningfully described by the fact that the wavefunctions of Eqs. (2.14) and (4.16) are assumed to be separable: the bosonic (fermionic) and the spin degrees of freedom do not interfere with each other.

We now introduce the two main assumptions of this chapter:

- The Hamiltonian has the general form:

$$\hat{H} = -\sum_i \left[t + \alpha \hat{A}_{l(i)}\right] \left(\hat{c}_i^\dagger \hat{c}_{i+1} + \hat{c}_{i+1}^\dagger \hat{c}_i\right) + \frac{\Delta}{2} \sum_i \hat{A}_{l(i)} \tag{A.1}$$

where we introduced a general hermitian operator $\hat{A}_i$ acting on a general degree of freedom living on the bonds of the chain. We also ignore the disordering contributions of Eq. (2.11) proportional to β.

- The ground state is separable in between its fermionic degrees of freedom and its general degrees of freedom living on the bonds:

$$|\Psi_{\text{GS}}\rangle = |\psi_f\rangle \otimes_i |\psi_{l(i)}\rangle \tag{A.2}$$

Then, by following the process of subsection 2.3.a, we find the same ground state ansatz for the energy as the one in equation (2.25). Differently from the spin-1/2 result, here $s_l = \langle\psi_l| \hat{A}_l |\psi_l\rangle$ and the variational parameters $\{s_l\}$ are no longer constrained to the values $\{1, -1\}$:

$$\epsilon(s_A, s_B) = -\frac{2}{\pi} t_{AB} E(1 - \delta_{AB}^2) + \frac{\Delta}{4}(s_A + s_B), \tag{A.3}$$

with t_{AB} and δ_{AB} defined as in subsection 2.3.a.

Note that the operator $\hat{A}_l$ is implicitly assumed to be bounded, so that its expectation value s_l is contained in a bounded range $[A_{\text{min}}, A_{\text{max}}]$. Under this constraint, we introduce the normalized operator:

$$\hat{\mathcal{A}}_l = (\hat{A}_l - a_m)/\delta_A, \tag{A.4}$$

where a_m is the middle point of the spectrum of $\hat{A}_l$:

$$a_m = \frac{A_{\text{min}} + A_{\text{max}}}{2}, \tag{A.5}$$

and δ_A is half of the extension of the spectrum of $\hat{A}_l$:

$$\delta_A = \frac{A_{\text{max}} - A_{\text{min}}}{2}. \tag{A.6}$$

The expectation value of $\hat{\mathcal{A}}_l$ is contained in $[-1, 1]$ and by substituting into Eq. (A.1) we find:

$$\hat{H} = -(t + \alpha a_m) \sum_i \left[\left(1 + \alpha' \hat{\mathcal{A}}_{l(i)}\right) \left(\hat{c}_i^\dagger \hat{c}_{i+1} + \hat{c}_{i+1}^\dagger \hat{c}_i\right) + \frac{\Delta'}{2} \hat{A}_{l(i)} \right], \tag{A.7}$$

where the bare couplings are:

$$\alpha' = \frac{\delta_A}{t + \alpha a_m} \alpha \tag{A.8}$$

for the interaction and:

$$\Delta' = (t + \alpha a_m)\,\Delta \tag{A.9}$$

for the effective potential on the bonds. As long as the renormalized hopping $t + \alpha a_m$ is different from zero, the Hamiltonian of Eq. (A.7) will present the same ground state of Eq. (A.1), but with spectrum now dependent on the renormalized energy scale $t + \alpha a_m$.

Having established the functional form of our energy ansatz in Eq. (A.1), we proceed by proving that the values that minimize Eq. (A.3) for $s_A, s_B \in [-1, 1]$ are exactly $\{1, -1\}$, the ones already found for the spin-1/2 case. As mentioned in chapter 2, the parameter space for $\beta = 0$ can be studied in the region $\alpha \geq 0$, as the ground state for a pair (α, Δ) is identical to $(-\alpha, -\Delta)$, once we send $\hat{A}_l \to -\hat{A}_l$. We then suppose that $0 < \alpha < t$, since the case $\alpha = 0$ is trivial. We also suppose that $\alpha < t$, since for $\alpha = \pm t$ the chain features hopping strengths equal to $2t$ or 0 and the Hamiltonian of Eq. (A.1) splits into noninteracting dimers.

If we introduce the change of variables $x = s_A + s_B$ and $y = s_A - s_B$, the energy ansatz reads:

$$\epsilon(x, y) = -\frac{2}{\pi}\left(t + \alpha\frac{x}{2}\right) E\left(1 - \left(\frac{\alpha y}{2t + \alpha x}\right)^2\right) + \frac{\Delta}{4}x, \tag{A.10}$$

which is symmetric for $y \to -y$ and we restrict our study to $y \in [0, 2]$, $x \in [-2, 2]$.

For $y = 0$ we have uniform hoppings and the energy is extremized by the highest values of $|x|$, so $s_A = s_B = \pm 1$.

For $y > 0$, the ansatz of equation (A.10) is a monotonic decreasing function of y:

$$\frac{\partial \epsilon}{\partial y} = \frac{2}{\pi}\alpha^2 y \frac{\partial}{\partial y} E\left(1 - \left(\frac{\alpha y}{2t + \alpha x}\right)^2\right). \tag{A.11}$$

The first derivative of the complete elliptic integral of the second kind, E', is strictly negative for $0 < \alpha < t$. Thus, the minima of the energy are at the boundaries of the s_A, s_B interval $[-1, 1]$, constraining s_A, s_B to the segments $s_B = -1$, $s_A \in [-1, 1]$ or $s_A = 1$, $s_B \in [-1, 1]$.

Focusing only on the first segment, the energy depends only on s_A and its second derivative is always negative or zero:

$$\frac{\partial^2 \epsilon}{\partial s_A^2}(s_A, s_B)\Big|_{s_B=-1} = \frac{\alpha^2}{2\pi}\left(\rho_1 E\left(1 - \delta_{AB}^2\right) - \rho_2 K\left(1 - \delta_{AB}^2\right)\right) \tag{A.12}$$

with:

$$\rho_1 = 2\frac{t_{AB}}{(t+\alpha s_A)^2} \tag{A.13}$$

$$\rho_2 = \frac{2t^2 + 2\alpha t(s_A - 1) + \alpha^2(s_A^2 + 1)}{(t+\alpha s_A)^2 2t_{AB}} \tag{A.14}$$

The same calculations can be repeated for the segment with $s_A = 1$, $s_B \in [-1, 1]$. Being a concave function over a closed interval, the minima of the energies are found at the boundaries of the segments. Thus the extrema of the energy may be found only at the values ± 1 for s_A, s_B.

Bibliography

[1] J. Ignacio Cirac and Peter Zoller. Goals and opportunities in quantum simulation. Nature Physics, 8, 4, pp. 264–266, 2012.

[2] Immanuel Bloch, Jean Dalibard, and Wilhelm Zwerger. Many-body physics with ultracold gases. Reviews of Modern Physics, 80, 3, pp. 885–964, 2008.

[3] D. Jaksch et al. Cold Bosonic Atoms in Optical Lattices. Phys. Rev. Lett., 81, pp. 3108–3111, 1998.

[4] Hendrik Weimer et al. A Rydberg quantum simulator. Nature Physics, 6, 5, pp. 382–388, 2010.

[5] J. Q. You and Franco Nori. Quantum information processing with superconducting qubits in a microwave field. Physical Review B, 68, 6, p. 064509, 2003.

[6] W. P. Su, J. R. Schrieffer, and A. J. Heeger. Solitons in Polyacetylene. Physical Review Letters, 42, 25, pp. 1698–1701, 1979.

[7] J.K. Asbóth, L. Oroszlány, and A.P. Pályi. A Short Course on Topological Insulators: Band Structure and Edge States in One and Two Dimensions. Springer International Publishing, 2016.

[8] Di Xiao, Ming-Che Chang, and Qian Niu. Berry phase effects on electronic properties. Reviews of Modern Physics, 82, 3, pp. 1959–2007, 2010.

[9] Antoine Browaeys and Thierry Lahaye. Many-body physics with individually controlled Rydberg atoms. Nature Physics, 16, 2, pp. 132–142, 2020.

[10] Immanuel Bloch, Jean Dalibard, and Sylvain Nascimbène. Quantum simulations with ultracold quantum gases. Nature Physics, 8, 4, pp. 267–276, 2012.

[11] J. Mögerle et al. Spin-1 Haldane phase in a chain of Rydberg atoms. PRX Quantum, 6, 2, p. 020332, 2025.

[12] Pimonpan Sompet et al. Realizing the symmetry-protected Haldane phase in Fermi–Hubbard ladders. Nature, 606, 7914, pp. 484–488, 2022.

[13] Marcos Atala et al. Direct measurement of the Zak phase in topological Bloch bands. Nature Physics, 9, 12, pp. 795–800, 2013.

[14] Sylvain de Léséleuc et al. Observation of a symmetry-protected topological phase of interacting bosons with Rydberg atoms. Science, 365, 6455, pp. 775–780, 2019.

[15] Xiao-Liang Qi and Shou-Cheng Zhang. Topological insulators and superconductors. Reviews of Modern Physics, 83, 4, pp. 1057–1110, 2011.

[16] Lukasz Fidkowski and Alexei Kitaev. Topological phases of fermions in one dimension. Physical Review B, 83, 7, p. 075103, 2011.

[17] Xie Chen, Zheng-Cheng Gu, and Xiao-Gang Wen. Classification of gapped symmetric phases in one-dimensional spin systems. Physical Review B, 83, 3, p. 035107, 2011.

[18] Xie Chen et al. Symmetry-Protected Topological Orders in Interacting Bosonic Systems. Science, 338, 6114, pp. 1604–1606, 2012.

[19] R. E. Peierls. Quantum Theory of Solids. Oxford University Press, 2001.

[20] Daniel González-Cuadra et al. Symmetry-breaking topological insulators in the ${\mathbb{Z}}_{2}$ Bose-Hubbard model. Physical Review B, 99, 4, p. 045139, 2019.

[21] Seiichi Kagoshima. Peierls Phase Transition. Japanese Journal of Applied Physics, 20, 9, p. 1617, 1981.

[22] Eduardo Fradkin and Jorge E. Hirsch. Phase diagram of one-dimensional electron-phonon systems. I. The Su-Schrieffer-Heeger model. Physical Review B, 27, 3, pp. 1680–1697, 1983.

[23] Daniel González-Cuadra et al. Strongly Correlated Bosons on a Dynamical Lattice. Physical Review Letters, 121, 9, p. 090402, 2018.

[24] T. Senthil. Symmetry-Protected Topological Phases of Quantum Matter. Annual Review of Condensed Matter Physics, 6, pp. 299–324, 2015.

[25] A. J. Heeger et al. Solitons in conducting polymers. Reviews of Modern Physics, 60, 3, pp. 781–850, 1988.

[26] Daniel González Cuadra. A cold-atom approach to topological quantum matter across the energy scale. PhD thesis, 2020.

[27] Pinaki Sengupta, Anders W. Sandvik, and David K. Campbell. Peierls transition in the presence of finite-frequency phonons in the one-dimensional extended Peierls-Hubbard model at half-filling. Physical Review B, 67, 24, p. 245103, 2003.

[28] Manuel Weber, Fakher F. Assaad, and Martin Hohenadler. Excitation spectra and correlation functions of quantum Su-Schrieffer-Heeger models. Physical Review B, vol. 91, 24, p. 245147, 2015.

[29] Christian Gross and Immanuel Bloch. Quantum simulations with ultracold atoms in optical lattices. Science, 357, 6355, pp. 995–1001, 2017.

[30] Matthew P. A. Fisher et al. Boson localization and the superfluid-insulator transition. Physical Review B, 40, 1, pp. 546–570, 1989.

[31] Markus Greiner et al. Quantum phase transition from a superfluid to a Mott insulator in a gas of ultracold atoms. Nature, 415, 6867, pp. 39–44, 2002.

[32] P. Jordan and E. Wigner. Über das Paulische Äquivalenzverbot. Zeitschrift für Physik, 47, 9, pp. 631–651, 1928.

[33] T. Holstein and H. Primakoff. Field Dependence of the Intrinsic Domain Magnetization of a Ferromagnet. Physical Review, 58, 12, pp. 1098–1113, 1940.

[34] Jürgen König and Fred Hucht. Newton series expansion of bosonic operator functions. SciPost Physics, 10, 1, p. 007, 2021.

[35] Phillip Weinberg and Marin Bukov. QuSpin: a Python package for dynamics and exact diagonalisation of quantum many body systems part I: spin chains. SciPost Physics, 2, 1, p. 003, 2017.

[36] J. Mögerle et al. Spin-1 Haldane phase in a chain of Rydberg atoms. arXiv:2410.21424, 2024.

[37] Tamás András Tóth. Quadrupolar Ordering in Two-Dimensional Spin-One Systems. PhD thesis, 2011.